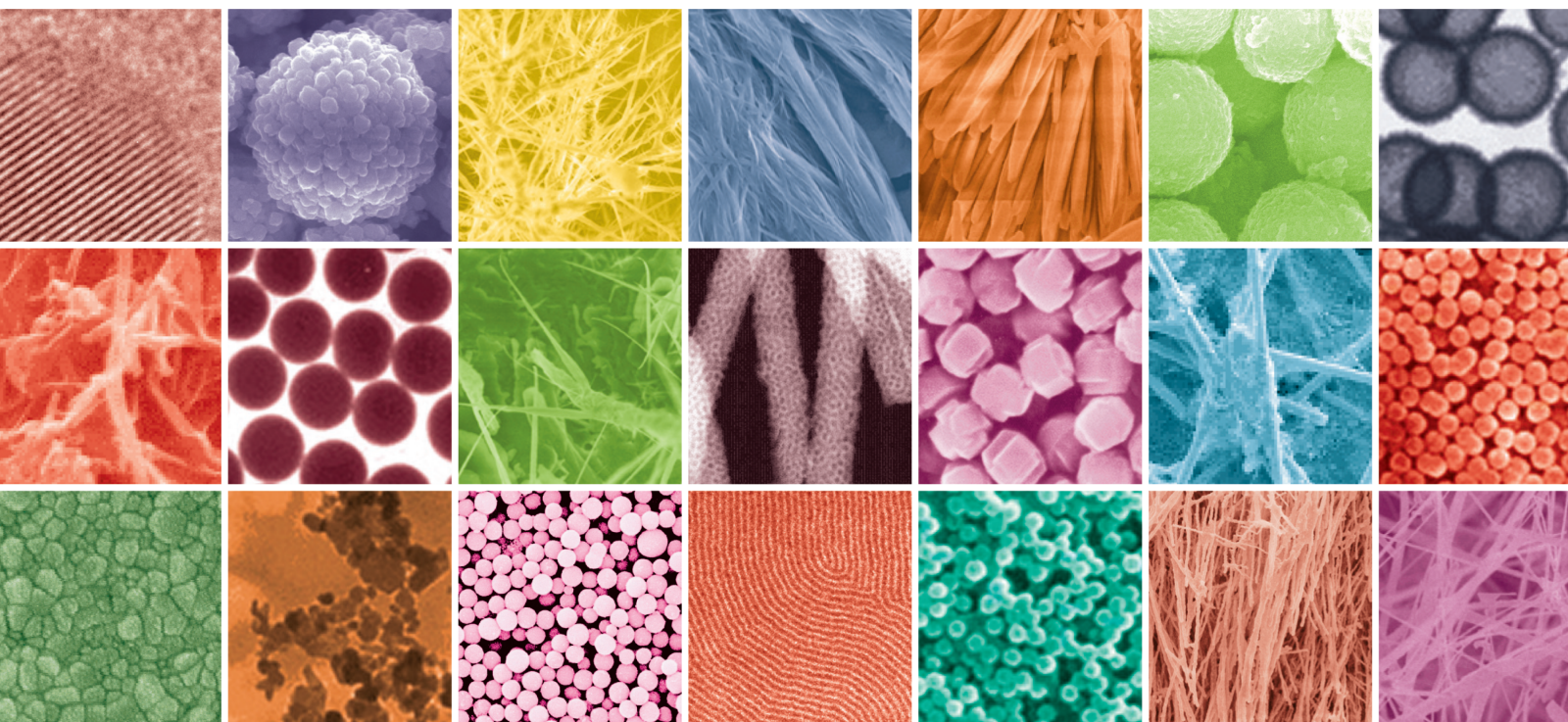# Synthesis, Properties and Advanced Applications of Fluorescent Nanomaterials

Lead Guest Editor: Xiao Jin
Guest Editors: Yuxiao Wang, Dongyu Li, and Jialong Duan

Synthesis, Properties and Advanced Applications of Fluorescent Nanomaterials

Synthesis, Properties and Advanced Applications of Fluorescent Nanomaterials

Lead Guest Editor: Xiao Jin
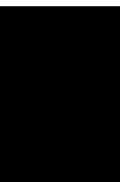Guest Editors: Yuxiao Wang, Dongyu Li, and Jialong Duan

Contents

Research Article

Study on the Chemotherapeutic Effect and Mechanism of Doxorubicin Hydrochloride on Drug-Resistant Gastric Cancer Cell Lines Using Metal-Organic Framework Fluorescent Nanoparticles as Carriers

Xianmei Lv,[1] Qiusheng Guo [ID],[2] and Liming Xu[1]

[1]*Department of Oncology, Quzhou Kecheng Hospital, Zhejiang Province, Quzhou 324000, China*
[2]*The 2ND Clinical Medical College of Zhejiang Chinese Medical University, Hangzhou 310053, China*

Correspondence should be addressed to Qiusheng Guo; zhanluzhihun@126.com

Objective. To prepare a polyethylene glycol- (PEG-) modified rare earth metal-organic framework material drug delivery system, obtain DOX@Eu (BTC) fluorescent nanoparticles after loading doxorubicin (DOX), and explore the effect of DOX@Eu (BTC) fluorescent nanoparticles on the chemotherapy sensitivity of gastric cancer multidrug-resistant cells SGC7901/ADR. *Methods.* The rare earth metal-organic framework fluorescent nanoparticles EU (BTC) were prepared by the solvent method and modified with PEG, and DOX@Eu (BTC) fluorescent nanoparticles were obtained after loading DOX. The particle size distribution of the prepared nanoparticles was analyzed by TEM, the adsorption performance of the prepared nanoparticles was evaluated by BET, the effective drug loading of DOX in the nanoparticles was determined by TGA analysis, and the pH response release performance was evaluated by *in vitro* release experiments. The MTT method was used to test the toxicity of EU (BTC) to GES-1 and SGC7901/ADR cells and detect the proliferation of SGC7901/ADR cells in each group. A fluorescence confocal microscope was used to observe the positioning of DOX@Eu (BTC) in SGC7901/ADR cells. The expression level of miR-185 in each group of cells was detected by RT-qPCR. The Annexin V-FITC/PI method was used to determine the apoptosis rate of cells in each group. The expression of MRS2 and related drug resistance proteins in each group of cells was detected by Western blotting (WB). The dual-luciferase reporter gene experiment was used to verify the targeting relationship between miR-185 and MRS2. *Results.* Most of the prepared EU (BTC) fluorescent nanoparticles have a particle size between 50 and 200 nm and have good adsorption capacity. The effective drug loading of DOX is 29%, and it has pH-responsive release performance and can be used in acidic environments. DOX was immobilized in EU (BTC) fluorescent nanoparticles, and DOX@Eu (BTC) fluorescent nanoparticles were present in the cytoplasm or cell membrane of SGC7901/ADR cells. Compared with DOX, DOX@Eu (BTC) fluorescent nanoparticles have stronger cytotoxicity to SGC7901/ADR cells, which also effectively inhibited the expression of multidrug resistance proteins in cells. The expression level of miR-185 in SGC7901/ADR cells decreased, but the expression level of MRS2 protein in SGC7901/ADR cells increased. miR-185 and MRS2 proteins are closely related to the multidrug resistance of SGC7901/ADR cells, and MRS2 is the downstream target gene of miR-185. After the treating of SGC7901/ADR cells with DOX@Eu (BTC) fluorescent nanoparticles, the expression of miR-185 in the cells increased significantly, while the expression of MRS2 protein decreased significantly, and the magnitude of the change was more obvious than that of DOX treatment. Overexpression of miR-185 (miR-mimics) or inhibition of MRS2 (si-MRS2) enhanced the inhibitory effect of DOX@Eu (BTC) fluorescent nanoparticles on the proliferation of SGC7901/ADR cells, which significantly increased the induction of apoptosis by DOX@Eu (BTC) fluorescent nanoparticles, and simultaneous enhanced the inhibitory effect on the expression level of multidrug resistance protein. However, overexpression of miR-185 and MRS2 (pc-MRS2+miR-mimics) at the same time did not affect the chemotherapy sensitivity of SGC7901/ADR cells to DOX@Eu (BTC) fluorescent nanoparticles. However, simultaneous transfection of miR-185 mimics and pc-MRS2 did not affect the chemotherapy sensitivity of SGC7901/ADR cells to DOX@Eu (BTC) fluorescent nanoparticles. *Conclusion.* DOX@Eu (BTC) fluorescent nanoparticles can effectively enhance the chemotherapy sensitivity of SGC7901/ADR cells to DOX, which may be achieved by upregulating the expression of miR-185 in SGC7901/ADR cells and then inhibiting the expression of MRS2 protein.

1. Introduction

Gastric cancer is a malignant tumor of the digestive tract with high morbidity and mortality worldwide [1]. Although there have been great advances in early screening and treatment of gastric cancer, the incidence of gastric cancer in my country is still high [2]. At this stage, the main treatment for gastric cancer is surgical resection, but most patients are already at an advanced stage when gastric cancer is diagnosed, and the effect of surgical treatment is still limited [3]. Studies have shown that chemotherapy has a good effect on killing tumor cells [4], but the 5-year survival period of gastric cancer patients after chemotherapy is much lower than expected [5], mainly because of the multidrug resistance of gastric cancer cells and complex tumor microenvironment [6, 7]. The tumor microenvironment is an extremely complex system, which is the main reason for inducing drug resistance of cancer cells and affecting the efficacy of chemotherapy drugs [8]. Nanoparticles are a kind of drug delivery system proposed in recent years that can encapsulate and target chemotherapeutic drugs to tumor tissues [9], which can effectively overcome the shortcomings of free chemotherapeutic drugs in the human body such as low effective dose, poor pharmacokinetic properties, and large side effects on patients, and improve the chemotherapy effect of cancer patients. The metal-organic framework compound is a new type of hybrid material, which is famous for its porosity and has the characteristics of ultrahigh surface area and large pore size suitable for adsorbing drugs. It also has the characteristics of being degradable, and after modification, it can improve the targeting of tumor cells and is a potential chemotherapeutic drug carrier [10]. MicroRNA (miRNA) is a class of noncoding single-stranded RNA molecules whose role has always been a hot spot in cancer research. Xia et al. reported that miR-185 is closely related to the proliferation, invasion, and metastasis of pancreatic cancer cells [11]. The report of Xiang et al. showed that miR-185 affects the sensitivity of ovarian cancer cells to cisplatin [12]. Also, the study by Tan et al. showed that miR-185 is related to the resistance of gastric cancer cells [13]. Doxorubicin hydrochloride (Doxorubicin, DOX) is a broad-spectrum antitumor antibiotic and a commonly used chemotherapeutic drug in the treatment of gastric cancer. However, related studies have shown that gastric cancer cells will develop resistance after exposure to DOX for a period, which affects the chemotherapy effect of DOX. [14].

This study intends to load DOX on polyethylene glycol- (PEG-) modified rare earth metal-organic framework material nanoparticles to obtain fluorescent DOX@Eu (BTC) nanoparticles and compare DOX with fluorescent DOX@Eu (BTC) nanoparticles, compare the effects of DOX and fluorescent DOX@Eu (BTC) nanoparticles on the chemotherapy sensitivity of gastric cancer multidrug-resistant cell line SGC7901/ADR, and explore the mechanism of their effects on the chemotherapy sensitivity of SGC7901/ADR.

2. Experimental Materials and Methods

2.1. Materials and Main Instruments

2.1.1. Materials.
Drug-resistant gastric cancer cell line SGC7901/ADR, gastric cancer cell line SGC7901, and human gastric epithelial cell line GES-1 were purchased from Shanghai Yiyan Biotechnology Co., Ltd. The primer sequences, miR-185 mimics, and si/pc-MRS2 were designed and synthesized by Biotech. Fetal bovine serum, penicillin, streptomycin, PBS buffer, pancreatin, and RPMI 1640 medium were purchased from Shanghai Yingxin Laboratory Equipment Co., Ltd. Adriamycin hydrochloride (CAS: 25316-40-9, content 99%) was purchased from Wuhan Yuanqi Pharmaceutical Chemical Co., Ltd. Dimethylformamide (DMF), absolute ethanol, 1-(3-dimethylaminopropyl)-3-ethylcarbodiimide hydrochloride (EDC), N-hydroxysuccinimide (NHS), 1,3,5-benzenetricarboxylic acid (H3BTC), europium nitrate (Eu (NO)3·6H2O), polyvinylpyrrolidone (PVP), sodium acetate (CH3COONa·3H2O), and dimethyl sulfoxide (DMSO) were purchased from Shanghai Anpu Experimental Technology Co., Ltd. 4$'$,6-diamidino-2-phenylindole (DAPI), MTT cell proliferation and toxicity detection kit, Trizol kit, RT-qPCR quantitative detection kit, Annexin V-FITC/PI apoptosis detection reagent kit, WB detection kit, and dual luciferase reporter gene detection kit were purchased from Shenzhen Zike Biotechnology Co., Ltd. Human mitochondrial MRS protein (MRS2) primary antibody, multidrug resistance protein (MDR1/P-gp, MDR-1 and CST-π) primary antibody, GAPDH primary antibody, and corresponding secondary antibody were purchased from Santa Cruz, USA.

2.1.2. Main Instruments.
Main instruments include laser confocal microscope (Zeiss LSM780), dialysis bag (Solarbio 18 mm, molecular cutoff flow 1000), thermogravimetric analyzer (TA TGAQ50), multifunctional microplate reader (Thermo MUL TIDKAN MK3), and incubator (Thermo IGO150).

2.2. Cell Culture and Transfection.
RPMI 1640 medium containing 10% fetal bovine serum, 1% penicillin, and streptomycin was used to culture drug-resistant gastric cancer cell line SGC7901/ADR, gastric cancer cell line SGC7901, and human gastric epithelial cell line GES-1, in an incubator at 37°C, with 5% CO_2 for routine culturing. SGC7901/ADR cells were cultured with DOX at a concentration of 0.1 μg/mL to maintain cell resistance. SGC7901/ADR cells at the logarithmic growth phase were inoculated into a 6-well plate after 0.25% trypsin digestion, and the cell concentration was adjusted to 10^4 cells/well. After overnight incubation, 50 pmol of miR-NC, miR-185 mimics, si-NC, si-MRS2, pc-NC, or pc-MRS2 were transfected into SGC7901/ADR cells, respectively. After incubating the cells at 37°C for 4-6 hours, the culture medium was replaced. After 24 hours, the RNA of each group was extracted, and the expression of miR-185 or MRS2 mRNA in the cells was detected by RT-qPCR.

2.3. Preparation of Nano-Eu (BTC) Loaded with Doxorubicin Hydrochloride.
A certain amount of H_3BTC, Eu $(NO)_3$·6H_2O, PVP, and CH_3COONa·3H_2O according to the

ratio of $1:2:47:20$ was weighted. H_3BTC and Eu $(NO)_3\cdot 6H_2O$ were dissolved in DMF to obtain the reaction precursor; PVP and $CH_3COONa\cdot 3H_2O$ were dissolved in the mixed solvent in advance (MDF : C_2H_6O : H_2O = 3 : 2 : 2). After that, the reaction precursor and the mixed solvent were transferred to a round-bottomed flask and mixed well to obtain the reaction solution. Heat the oil bath to 80°C and stir; after 24 h, absolute ethanol was used to wash 3 times to obtain Eu (BTC) crystals. 5 mg of dried Eu (BTC) crystals were dispersed in 7 mL of H_2O and stirred at room temperature. 10 mg EDC, 10 mg NHS, and 20 mg PEG were dissolved in 1 mL H_2O, and the EDC solution was added to the stirred Eu (BTC) dispersion and continued to stir for 10 minutes before adding the NHS solution. The reaction was continued at room temperature for 24 h and centrifuged ($500\times$g) for 5 min. The precipitated PEG-modified fluorescent Eu (BTC) nanoparticles were collected and washed. 5 mg of dried fluorescent Eu (BTC) nanoparticle powder was used and immersed in 1 mL DOX aqueous solution (8 mg/mL) and stirred for 24 h at room temperature to obtain DOX-loaded fluorescent Eu (BTC) nanoparticle (DOX@Eu (BTC)).

2.4. Identification of Fluorescent DOX@Eu (BTC) Nanoparticles.

An appropriate amount of PEG-modified fluorescent Eu (BTC) nanoparticles was dissolved in H_2O. After stirring, a transmission electron microscope was used to take pictures of different positions, the particle diameters of 500 nanoparticles in different positions were counted, and a particle size distribution map was made. Take an appropriate amount of PEG-modified fluorescent Eu (BTC) nanoparticles for washing and dry at 170°C to obtain a white powder. After setting the specific surface tester parameters, its nitrogen adsorption-desorption isotherm was tested under the condition of the ice-water mixture. The thermal stability of fluorescent Eu (BTC) nanoparticles and fluorescent DOX@Eu (BTC) nanoparticles and the effective DOX load of fluorescent DOX@Eu (BTC) nanoparticles were analyzed with a thermogravimetric analyzer. 5 mg of the sample to be tested was placed on the tray, and the speed was measured under an N_2 atmosphere; the heating rate is 20°C/min, and the maximum temperature is 900°C. The dialysis method was used to compare the DOX release of fluorescent DOX@Eu (BTC) nanoparticles in vitro at different pHs. An appropriate amount of fluorescent DOX@Eu (BTC) nanoparticles was dissolved in H_2O, centrifuged ($500\times$g) for 5 min, and then removed clear. After washing 3 times with ultrapure water, the precipitate was resuspended in 3 mL of the corresponding pH buffer solution, and after mixing, transferred to a dialysis bag and placed in the same pH buffer solution. Finally, stir at a speed of 300 rpm, and the amount of DOX released at each time point was recorded.

2.5. Fluorescent Eu (BTC) Nanoparticle Toxicity Test (MTT).

An appropriate amount of fluorescent Eu (BTC) nanoparticles was dissolved in PBS buffer; the density was adjusted to 2 mg/mL. SGC7901/ADR cells were inoculated at a density of 10^4 cells/well in a 96-well plate and incubated overnight. The prepared fluorescent Eu (BTC) nanoparticle solution was diluted; the final concentration was adjusted to 20 μg/mL, 10 μg/mL, 4 μg/mL, 1 μg/mL, and 0.1 μg/mL; and

a blank control was also set. The medium in the 96-well plate was aspirated, and 200 μL of each gradient concentration solution was added, incubated for 24 h after adding the drug. Then, 20 μL of MTT (5 μg/mL) solution was added to each well and incubated for 4 h. After aspirating the test solution in each well, 150 μL DMSO was added to dissolve the crystals. Finally, a multifunctional microplate reader was used to detect the absorbance of each group of cells at 490 nm, and the absorbance was recorded.

2.6. Sensitivity of SGC7901/ADR Cells to DOX and Fluorescent DOX@Eu (BTC) (MTT).

An appropriate amount of DOX or fluorescent DOX@Eu (BTC) nanoparticles was dissolved in PBS buffer to ensure that the net DOX concentration is 10 μg/mL, and a blank control was also set. The MTT method was used to detect the effects of DOX and fluorescent DOX@Eu (BTC) nanoparticles on the cell viability of each group of SGC7901/ADR. The method was the same as the above, and the absorbance of each group of cells at 1 h, 6 h, 12 h, 24 h, 36 h, 48 h, 60 h, and 72 h was recorded.

2.7. Observation of the Fluorescent DOX@Eu (BTC) Localization in Cell by a Confocal Laser Microscope.

An appropriate amount of fluorescent DOX@Eu (BTC) nanoparticles was dissolved in PBS buffer to ensure that the net DOX concentration is 10 μg/mL. The prepared PBS solution was cocultured with SGC7901/ADR cells for 12 h. After incubation, the nuclei were stained with DAPI, and the localization of fluorescent DOX@Eu (BTC) nanoparticles in the cells was observed by a laser confocal microscope.

2.8. Detection of the Expression of miR-185 and MRS2 mRNA in Cells.

Trizol one-step method was used to extract total RNA from each group of cells, and 2 μg total RNA was used to synthesize cDNA. Take 2 μL of reverse transcription product, 10 μL of SYBR Green Mix, 0.5 μL of the upstream, and downstream primers of miR-185 or MRS2 mRNA and establish a PCR reaction system with a total volume of 20 μL according to the kit instructions. The PCR thermal cycle parameters were 95°C for 5 min, 94°C for 30 s, and 60°C for 30 s, with a total of 45 cycles. The primer sequence is as follows: MRS2(R): $5'$-CCAGAACCATGGAATGCCTGC-$3'$, MRS2(F): $5'$-GTATCCACGGGGCTGTTCCTAAC-$3'$; miR-185(R): $5'$-CAATGGAGAGAAAGGCAGTTCC-$3'$, miR-185(F): $5'$-AATCCATGAGAGATCCCTACCG-$3'$; GAPDH(R): $5'$-CGCTCCTGGAAGATGGTGAT-$3'$, GAPDH(F): $5'$-GACCCCTTTCATTGACCTCAAC-$3'$. The $2^{(-\triangle\triangle Ct)}$ method was used to calculate the relative expression level of each gene.

2.9. Detection of Apoptosis Level.

The cells in each group were cultured for 24 hours, and DOX or fluorescent DOX@Eu (BTC) nanoparticle solution with a net concentration of 10 μg/mL was added. After continuing the routine culture for 48 hours, the cells were digested with 0.25% trypsin and collected. After washing 3 times with PBS, the apoptosis ratio of each group was determined by Annexin V-FITC/PI double staining according to the kit instructions.

2.10. Detection of the Protein Expression of Multidrug Resistance Gene and MRS2.

Cells at the logarithmic growth

phase were collected to extract the total protein in each group of cells, and the protein concentration was determined by the BCA method. After adding SDS-PAGE loading buffer, heat denaturation treatment was performed. $15\,\mu g$ total protein was added to each lane, and electrophoresis with 20 mA current for 60 min. The sample was transferred to the PVDF membrane by the wet transfer method and sealed with 5% skim milk at room temperature for 3 hours. After that, the diluted multidrug resistance protein primary antibody, MRS2 primary antibody, or GAPDH primary antibody (1 : 1000) was added and incubated overnight at 4°C. Then, the corresponding secondary antibody (1 : 10000) was added and incubated at room temperature for 1 h. Finally, after ECL luminescence development, pictures were taken, and Image-j was used to analyze the gray value of each band, and the relative expression level was calculated.

2.11. The Verification of the Targeting Relationship between miR-185 and MRS2 by Dual-Luciferase Reporter Gene Experiment. Cells at the logarithmic growth phase were collected, digested with 0.25% trypsin, and inoculated in a 96-well plate at a density of 10^4 cells/well. After overnight incubation, miR-NC, WT-MRS2 or MUT-MRS2, miR-185 mimics, and WT-MRS2 or MUT-MRS2 were transfected into SGC7901/ADR cells and then incubated for 48 h after transfection. The cell suspension in each well was centrifuged (1000×g) for 5 minutes, and the supernatant was collected and transferred to a 96-well plate. The fluorescence of each well was measured when the firefly luciferase substrate and the Renilla luciferase substrate were added. The relative luciferase activity was calculated of each well.

2.12. Statistical Analysis. All experiments are repeated three times, and the data were expressed as mean ± standard deviation ($\bar{x} \pm s$). GraphPad Prism 8.2.1 software was used for data analysis and picture drawing. The comparison between the two groups was performed by t test, and the comparison between multiple groups was performed by one-way analysis of variance. $P < 0.05$ or $P < 0.01$ indicated that the difference was statistically significant.

3. Results

3.1. Characterization of Fluorescent DOX@Eu (BTC) Nanoparticles. The particle size of PEG-modified fluorescent Eu (BTC) nanoparticles was analyzed, and the results showed that the average particle size was 130 nm, the maximum was 270 nm, and the minimum was 60 nm. More than 74% of the nanoparticles have a size distribution between 100 and 200 nm (see Figure 1(a)). The micropore structure of the prepared fluorescent Eu (BTC) nanoparticles was characterized, and the results showed that the specific surface area of the PEG-modified fluorescent Eu (BTC) nanoparticles was 2461.11 m^2/g, and the pore volume was 0.76×10^{-6} m^3/g. The average pore radius is 38.29×10^{-10} m, and the N$_2$ adsorption-desorption isotherm has obvious hysteresis loops, which is a characteristic curve of typical mesoporous materials and has good adsorption capacity (as shown in Figure 1(b)). After loading DOX, fluorescent DOX@Eu

(BTC) nanoparticles were obtained, and the heating curves of fluorescent Eu (BTC) nanoparticles and fluorescent DOX@Eu (BTC) nanoparticles were compared. The quality of fluorescent Eu (BTC) nanoparticles decreased steadily at 20~350°C, and the rate of mass decrease appears a short plateau at 350°C. The mass loss caused by bound water and DMF was about 20%, which was consistent with the theoretical calculation. For fluorescent DOX@Eu (BTC) nanoparticles, the temperature rise curve was similar to fluorescent Eu (BTC) nanoparticles below 200°C. When the temperature was above 200°C, DOX gradually decomposed, increasing the rate of mass decline. At 350°C, the remaining mass percentage of fluorescent DOX@Eu (BTC) nanoparticles was about 71%, that is, the effective drug loading of fluorescent DOX@Eu (BTC) nanoparticles was about 29%. The remaining mass percentages of fluorescent Eu (BTC) nanoparticles and fluorescent DOX@Eu (BTC) nanoparticles at 900°C were 29.53% and 40.12%, which were consistent with the theoretical calculation values (as shown in Figure 1(c)). The *in vitro* release of fluorescent DOX@Eu (BTC) nanoparticles at different pHs was compared, and the results showed that when the pH was 7.4, the release of DOX was relatively slow, and the release rate gradually increased as the pH decreased (as shown in Figure 1(d)).

3.2. The Effect of Fluorescent DOX@Eu (BTC) on SGC7901/ADR Cells. MTT was used to detect the toxicity of fluorescent Eu (BTC) to GES-1 and SGC7901/ADR cells. The results showed that the concentration of fluorescent Eu (BTC) at $0.1~20\,\mu g/mL$ had no significant effect on cell survival, indicating that fluorescent Eu (BTC) was nontoxic to GES-1 and SGC7901/ADR cells (as shown in Figure 2(a)). The laser confocal microscope was used to observe the positioning of fluorescent DOX@Eu (BTC) in the cell, and the results showed that the red fluorescence did not overlap with the blue fluorescence, and the red fluorescence was ringed around the blue fluorescence, indicating that DOX was fixed on the fluorescent Eu (BTC) nanoparticles and cannot enter the nucleus. DOX and Eu (BTC) existed together in the cell membrane or cytoplasm (as shown in Figure 2(b)). MTT method was also used to detect the inhibitory effect of DOX and fluorescent DOX@Eu (BTC) on SGC7901/ADR cells. With the increase of the action time under the same net DOX concentration, both DOX and fluorescent DOX@Eu (BTC) can significantly reduce the SGC7901/ADR cell survival rate ($P < 0.05$). In the first 30 h, DOX inhibited cells better than fluorescent DOX@Eu (BTC) nanoparticles, but after 30 h, fluorescent DOX@Eu (BTC) inhibited cells better than DOX. This was caused by the gradual release of DOX loaded in fluorescent Eu (BTC) and the gradual increase in the effective drug concentration in the cells (as shown in Figure 2(c)). Annexin V-FITC/PI was performed to detect the effects of DOX and fluorescent DOX@Eu (BTC) on SGC7901/ADR cell apoptosis. The results showed that both DOX and fluorescent DOX@Eu (BTC) significantly increased the early apoptosis and late apoptosis of SGC7901/ADR cells ($P < 0.05$), and fluorescent DOX@Eu (BTC) had a more obvious effect on the early apoptosis of SGC7901/ADR cell ($P < 0.05$) (see Figure 2(d)). Western blotting was used to

(a)

(b)

(c)

(d)
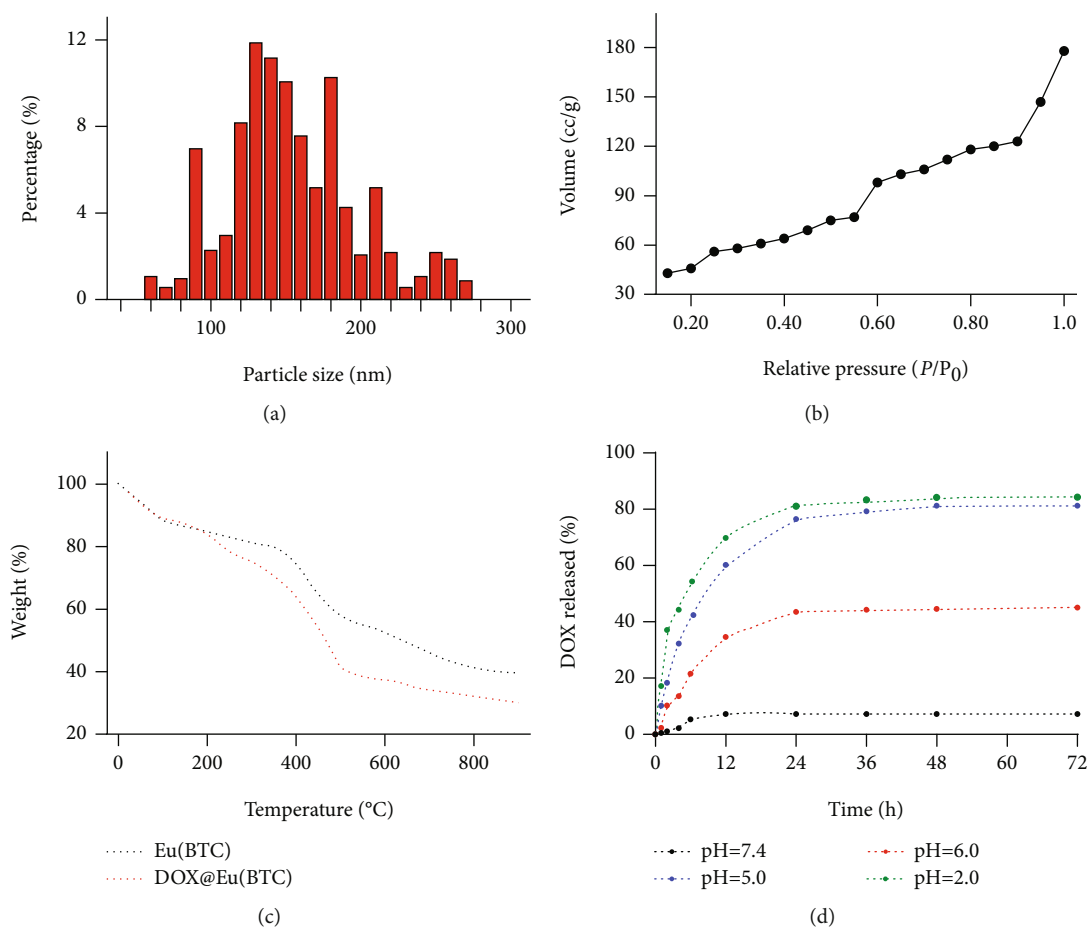
FIGURE 1: Characterization of prepared fluorescent nanoparticles. (a) Size distribution of nano-Eu (BTC). (b) Nitrogen adsorption-desorption isotherm curve of nano-Eu (BTC); (c) TGA analysis of Eu (BTC) and DOX@Eu (BTC). (c) TGA analysis of DOX@Eu (BTC) and Eu (BTC). (d) Releasing the curve of the DOX in vitro under different pH.

detect the expression of resistance-related proteins, and the results showed that both DOX and fluorescent DOX@Eu (BTC) significantly inhibited the expression of MDR1/P-gp, MDR-1, and CST-π proteins in cells ($P < 0.05$), and fluorescent DOX@Eu (BTC) has a more obvious inhibitory effect on the expression of multidrug resistance protein ($P < 0.05$) (see Figure 2(e)).

3.3. The Effect of miR-185 on the Drug Resistance of SGC7901/ADR Cells. RT-qPCR was used to detect the expression of miR-185 in different cell lines. The results showed that the expression of miR-185 in SGC7901 and SGC7901/ADR cell lines was significantly lower than that in GES-1 cell line ($P < 0.05$), and the expression level in SGC7901/ADR cell line was the lowest ($P < 0.05$) (see Figure 3(a)). When miR-185 mimics were transfected into the SGC7901/ADR cell line, the expression level of miR-185 in the cells increased significantly ($P < 0.05$) (as shown in Figure 3(b)). MTT was used to detect the toxicity of fluorescent DOX@Eu (BTC) to SGC7901/ADR cells transfected with miR-185 mimics. The results showed that the transfection of miR-185 mimics can significantly enhance the toxicity of fluorescent DOX@Eu (BTC) to SGC7901/ADR cells and inhibit the proliferation of SGC7901/ADR cells ($P < 0.05$)

(as shown in Figure 3(c)). Annexin V-FITC/PI was used to detecting the effect of fluorescent DOX@Eu (BTC) on the apoptosis of SGC7901/ADR cells transfected with miR-185 mimics. The results showed that the transfection of miR-185 mimics significantly increased the apoptosis of SGC7901/ADR cells induced by fluorescent DOX@Eu (BTC) ($P < 0.05$), which had a more obvious effect on the early apoptosis of SGC7901/ADR cells ($P < 0.05$) (as shown in Figure 3(d)). Western blotting was used to detect the effect of fluorescent DOX@Eu (BTC) on the expression of related drug resistance proteins in SGC7901/ADR cells transfected with miR-185 mimics. The results showed that transfection of miR-185 mimics significantly enhanced the inhibitory effect of fluorescent DOX@Eu (BTC) on the expression of related drug-resistant proteins ($P < 0.05$) (as shown in Figure 3(e)).

3.4. Targeting Relationship between miR-185 and MRS2. The bioinformatics website ENCORI predicted potential downstream target genes of miR-185. The results showed that MRS2 was a downstream target gene of miR-185, and the target binding sequence was shown in Figure 4(a). The dual-luciferase reporter gene experiment verified the targeting relationship between miR-185 and MRS2. The results

(a)

(b)

(c)

(d)
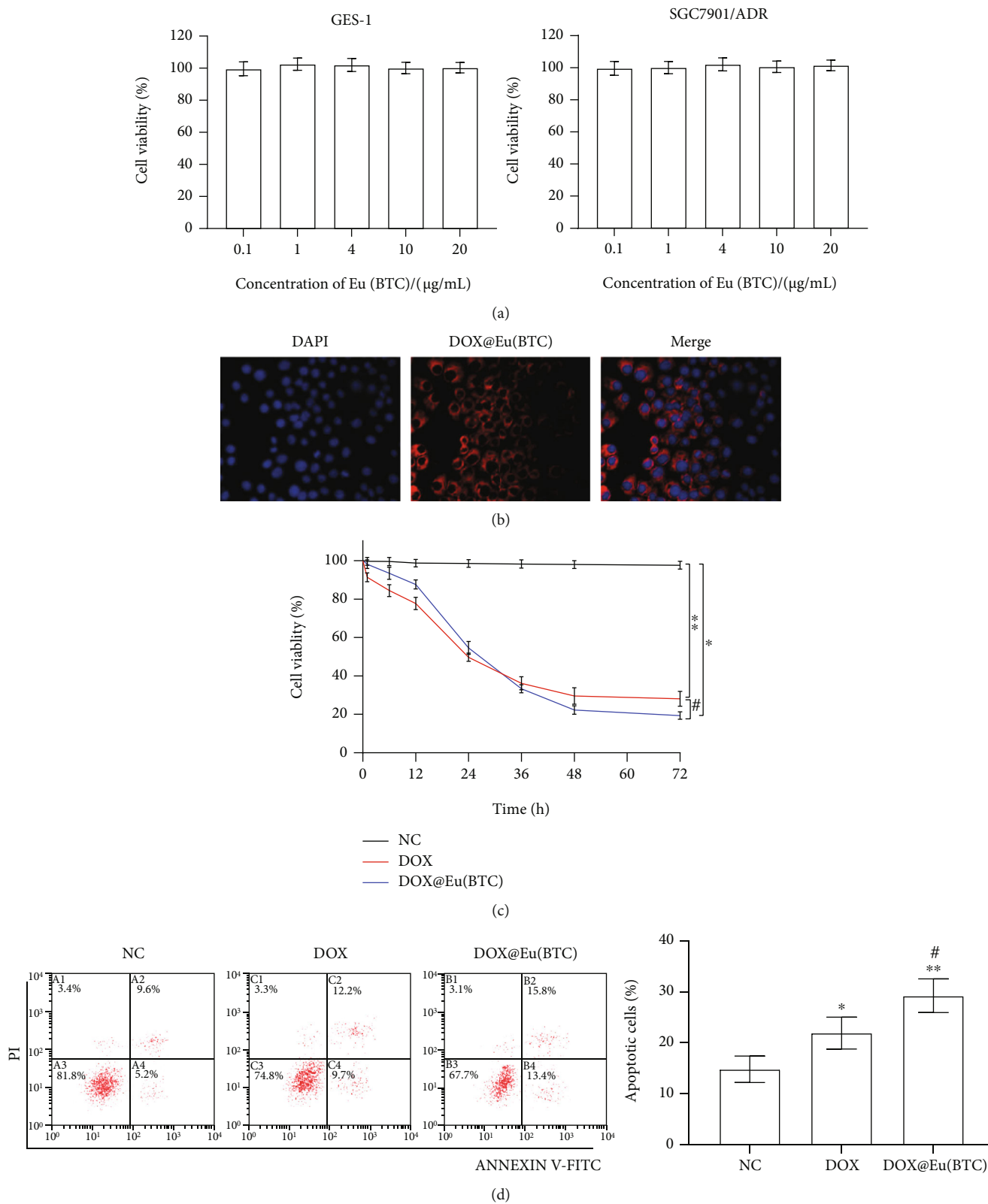
FIGURE 2: Continued.
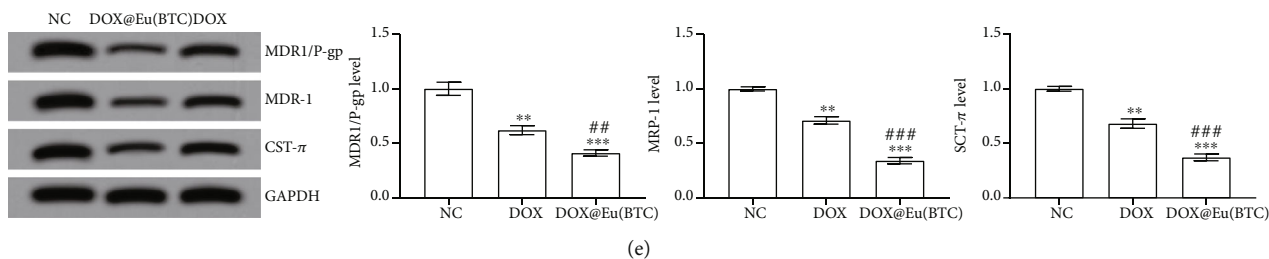
FIGURE 2: Effect of DOx@EU (BTC) fluorescent nanoparticles on SGC7901/ADR cells. (a) Result of the cytotoxic test of Eu (BTC). (b) CLSM image of SGC7901/ADR cells after incubation with DOX@Eu (BTC). (c) Result of the cytotoxic test of DOX and DOX@Eu (BTC) after different incubation times. (d) Result of DOX and DOX@EU (BTC) on the apoptosis rate of SGC7901/ADR cells. (e) Result of DOX and DOX@EU (BTC) on multidrug resistance protein relative expression level of SGC7901/ADR cells.
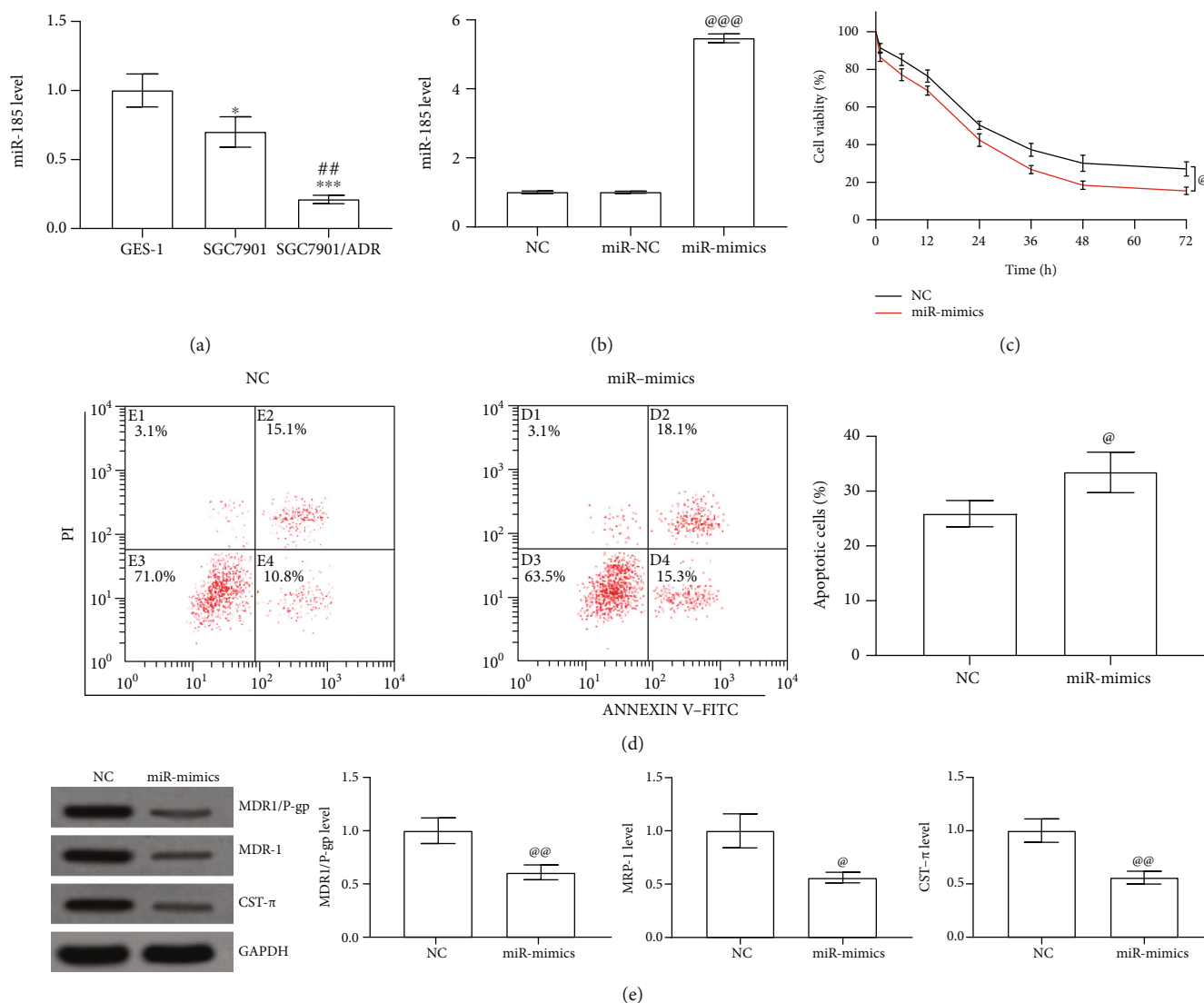
FIGURE 3: Effect of miR-185 on the drug resistance of SGC7901/ADR cells. $^*P < 0.05$ and $^{***}P < 0.001$ vs. GES-1 group; $^{##}P < 0.01$ vs. SGC7901 group; $^@P < 0.05$, $^{@@}P < 0.01$, and $^{@@@}P < 0.001$ vs. NC group. (a, b) The expression level of miR-185 in SGC7901/ADR cells. (c) Comparison of DOX@Eu (BTC) on cell viability SGC7901/ADR cell by different transfection. (d) Comparison of DOX@Eu (BTC) on cell apoptosis rate SGC7901/ADR cell by different transfection. (e) Comparison of DOX@Eu (BTC) on multidrug resistance protein relative expression SGC7901/ADR cell by different transfection.

MSR2: 5′-cgauuGGCUGACGAUCUCUCCa-3′
          : : | | | | | | | | | |
miRNA: 5′-aguccUUGACGGAAAGAGAGGu-3′

(a)

(b)

(c)
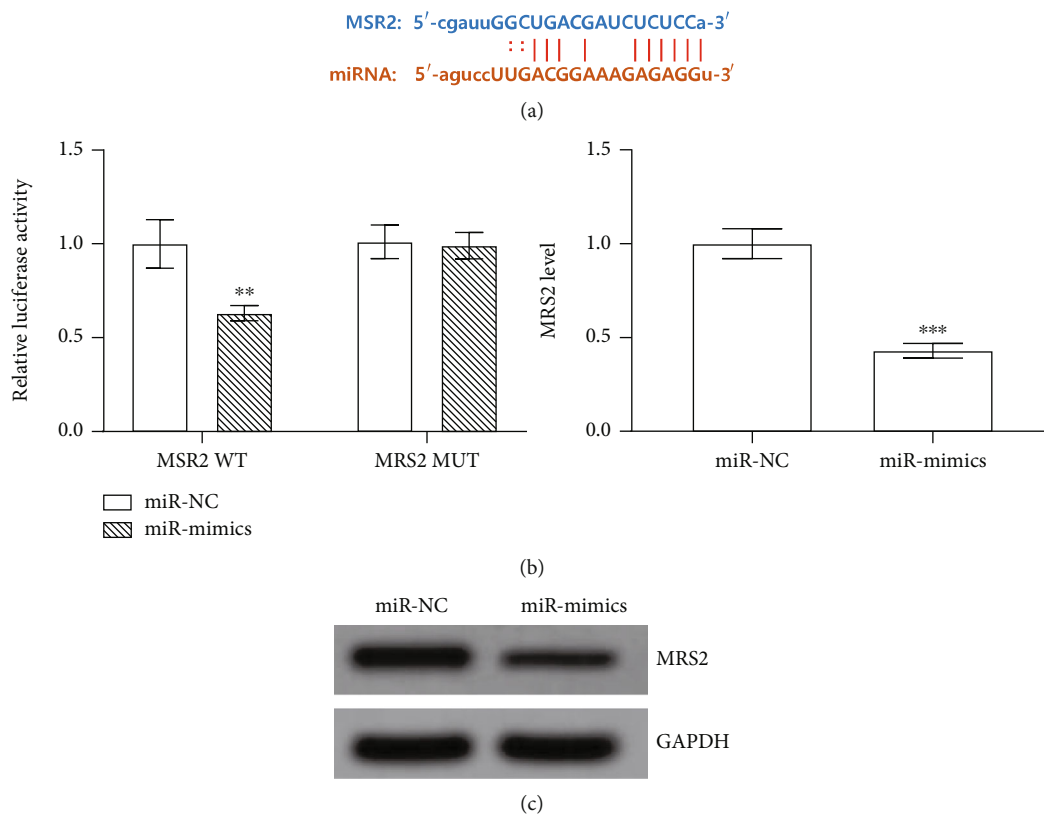
FIGURE 4: Verification of the targeting relationship between miR-185 and MRS2. $^{**}P < 0.01$ and $^{***}P < 0.001$ vs. miR-NC group. (a) Targeting area of miR-185 and MRS2. (b) Dual-luciferase reporter gene verified the targeting relationship between miR-185 and MRS2. (c) Expression levels of MRS2 in SGC7901/ADR cell.

showed that miR-185 significantly inhibited the luciferase activity of the wild-type MRS2 vector ($P < 0.05$) (as shown in Figure 4(b)). Western blotting was used to detect the effect of miR-185 on the expression level of MRS2 protein, and the results demonstrated that miR-185 significantly inhibited the expression level of MRS2 protein (as shown in Figure 4(c)).

3.5. The Effect of MRS2 on the Drug Resistance of SGC7901/ADR Cells. Western blotting was used to detect the expression of MRS2 in different cell lines and SGC7901/ADR cells after transfection with si-MRS2. The results showed that the expression of MRS2 protein in SGC7901 and SGC7901/ADR cell lines was significantly higher than that in GES-1 cells ($P < 0.05$), and the expression level in SGC7901/ADR cell line was the highest ($P < 0.05$) (see Figure 5(a)). SGC7901/ADR cell line was transfected with si-MRS2, and the expression level of MRS2 protein in the cells was significantly reduced ($P < 0.05$) (as shown in Figure 5(b)). MTT was used to detect the toxicity of fluorescent DOX@Eu (BTC) to SGC7901/ADR cells transfected with si-MRS2, and the results discovered that the transfection of si-MRS2 can significantly inhibit the proliferation of SGC7901/ADR cells ($P < 0.05$) (as shown in Figure 5(c)). Annexin V-FITC/PI was used to detecting the effect of fluorescent DOX@Eu (BTC) on the apoptosis of SGC7901/ADR cells transfected with si-MRS2. The results showed that the transfection of si-MRS2 significantly increased the apoptosis of

SGC7901/ADR cells induced by fluorescent DOX@Eu (BTC) ($P < 0.05$), which had similar effects on early and late apoptosis of SGC7901/ADR cells (as shown in Figure 5(d)). Western blotting was used to detect the effect of fluorescent DOX@Eu (BTC) on the expression of related drug resistance proteins in SGC7901/ADR cells transfected with si-MRS2. The results showed that the transfection of si-MRS2 significantly inhibited the expression of related drug resistance proteins in the SGC7901/ADR cell line ($P < 0.05$) (as shown in Figure 5(e)).

3.6. Fluorescent DOX@Eu (BTC) Affects the Chemotherapy Sensitivity of SGC7901/ADR Cells through the miR-185/MRS2 Molecular Axis. RT-qPCR was used to detect the expression of miR-185 in SGC7901/ADR cells after treatment with DOX and fluorescent DOX@Eu (BTC). The results showed that the expression of miR-185 in SGC7901/ADR cells was significantly increased after drug treatment ($P < 0.05$), and the expression of miR-185 after fluorescent DOX@Eu (BTC) treatment was significantly higher than that after DOX treatment ($P < 0.05$) (see Figure 6(a)). Western blotting was used to detect the expression level of MRS2 in SGC7901/ADR cells after treatment. The results showed that the expression level of MRS2 protein in SGC7901/ADR cells was significantly reduced after drug treatment, and the expression level of MRS2 protein after fluorescent DOX@Eu (BTC) treatment was significantly lower than that after DOX treatment ($P < 0.05$) (see
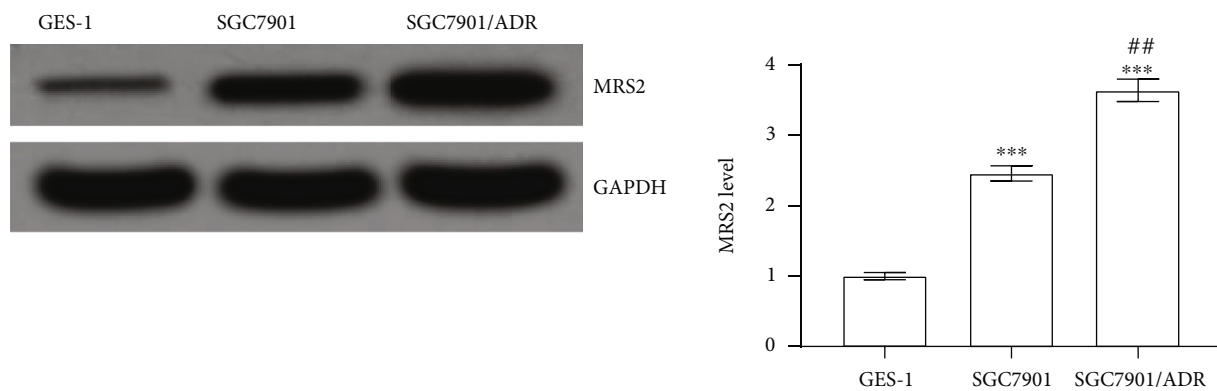
(a)
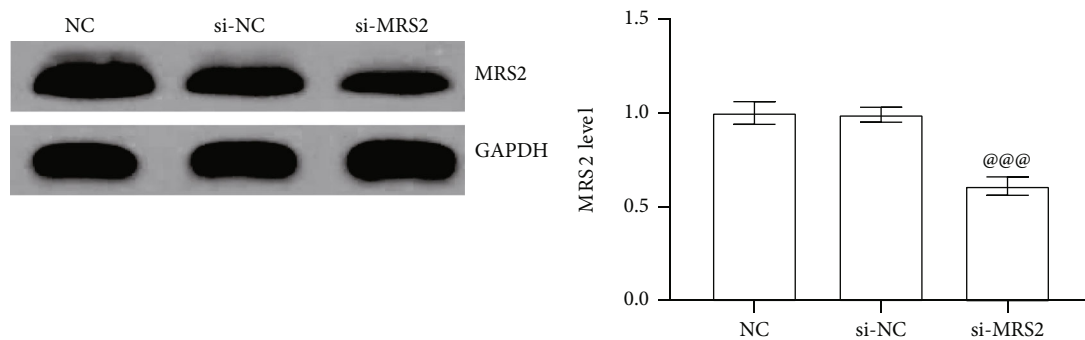
(b)
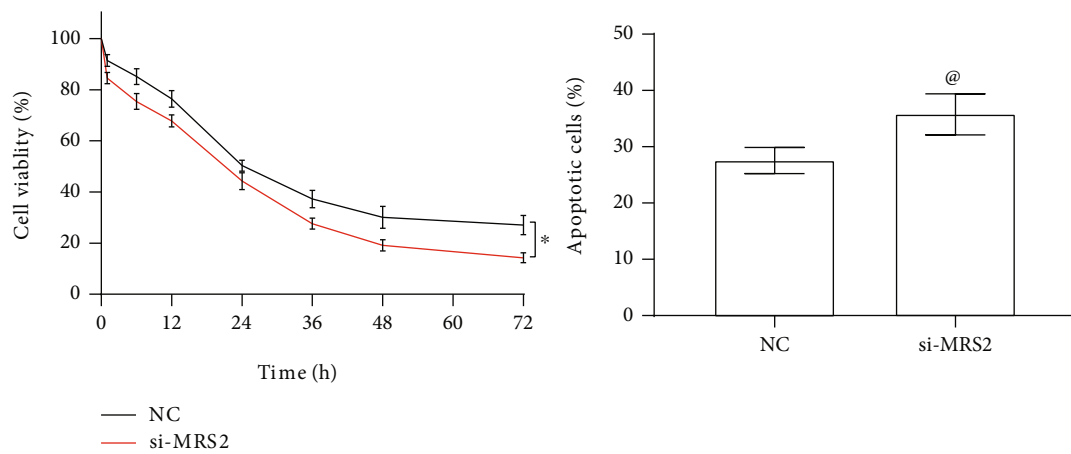
(c)

FIGURE 5: Continued.

(d)

(e)
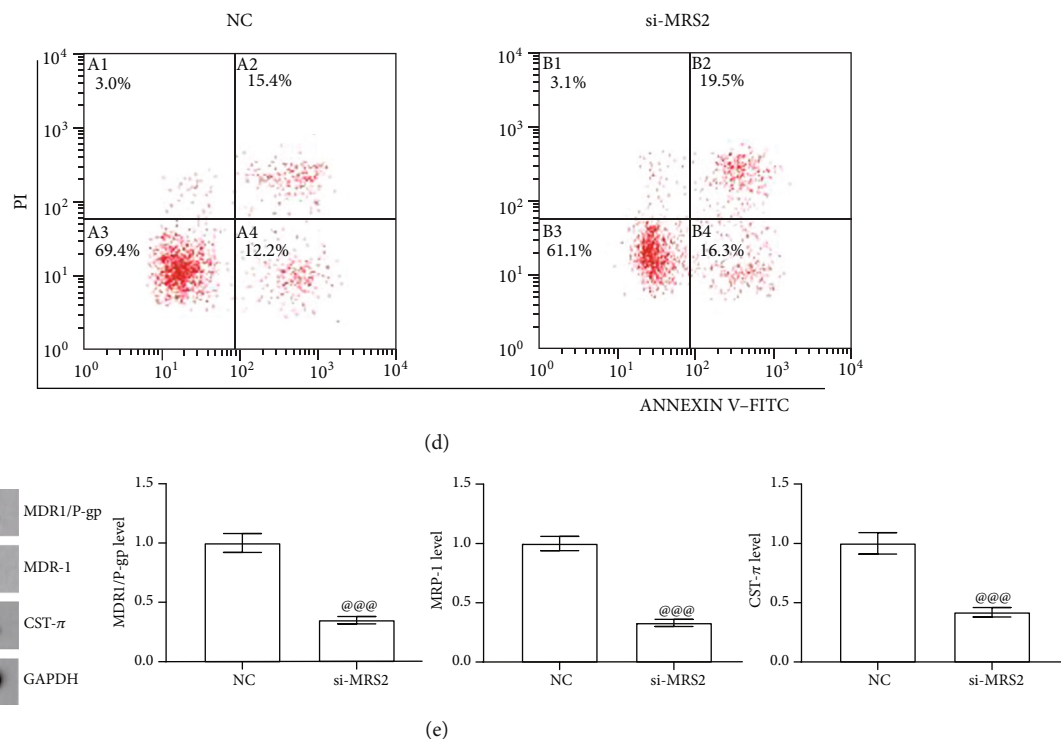
FIGURE 5: Effect of MRS2 on the drug resistance of SGC7901/ADR cells. $^{***}P < 0.001$ vs. GES-1 group; $^{\#\#}P < 0.01$ vs. SGC7901 group; $^{@}P < 0.05$ and $^{@@@}P < 0.001$ vs. NC group. (a, b) The expression level of MRS2 in SGC7901/ADR cells. (c) Comparison of DOX@Eu (BTC) on cell viability SGC7901/ADR cell by different transfection. (d) Comparison of DOX@Eu (BTC) on cell apoptosis rate SGC7901/ADR cell by different transfection. (e) Comparison of DOX@Eu (BTC) on multidrug resistance protein relative expression SGC7901/ADR cell by different transfection.

Figure 6(b)). After the transfection of pc-MRS2, the expression level of MRS2 protein in SGC7901/ADR cells increased significantly ($P < 0.05$); however, transfection of miR-185 mimics and pc-MRS2 at the same time had no significant effect on the expression level of MRS2 protein in SGC7901/ADR cells (as shown in Figure 6(c)). MTT, Annexin V-FITC/PI, and Western blotting were used to detect the effects of fluorescent DOX@Eu (BTC) on the proliferation, apoptosis, and related drug resistance protein expression of SGC7901/ADR cells transfected with miR-185 mimics and pc-MRS2. The results showed that the expression levels of proliferation, apoptosis, and related drug resistance proteins in fluorescent DOX@Eu (BTC) treatment of SGC7901/ADR cells transfected with miR-185 mimics and pc-MRS2 at the same time were not significantly different from those of untransfected SGC7901/ADR cells (see Figures 6(d)–6(f)).

4. Discussion

Gastric cancer ranks first among the malignant tumors of the digestive tract in my country, with a poor prognosis [1]. Chemotherapy is the main method for the treatment of advanced gastric cancer. However, the emergence of multidrug resistance in gastric cancer cells often leads to chemotherapy failure. Studies have shown that drug delivery systems using nanoparticles as carriers can target drugs to tumor tissues and improve the sensitivity of tumor tissues to chemotherapy

[15]. Nanodrug carrier refers to a drug delivery system obtained by combining nanoparticles with a particle size of 10~1000 nm and drugs, which can transport drugs to tumor tissues, change the distribution of drugs in patients, and reduce the loss of drugs in the normal group, which can also reduce side effects and improve the bioavailability of drugs. Compared with general materials, metal-organic framework materials have the characteristics of larger specific surface area and porosity. It is currently known as the largest and lightest crystalline material with the largest specific surface area. In recent years, it has achieved rapid development in the field of drug release [16]. Because rare-earth metal-organic framework materials integrate the advantages of metal-organic framework materials as nano-drug carriers and the excellent optical properties of rare-earth metals, they have attracted more attention in the field of drug delivery systems [17].

The drug delivery system believes that the carrier with a particle size of 50~200 nm can be targeted and retained in the tumor site through the high permeability and long retention effect. 74% of the fluorescent EU (BTC) nanoparticles synthesized in this study have a particle size of 100~200 nm. In the meantime, more than 85% of the nanoparticles have a particle size between 50 and 200 nm, which meets the basic requirements of high permeability and long retention effect [18]. PEG has good compatibility with many organic substances and can improve the surface characteristics of nanoparticles [19], so the rare earth metal-organic framework material nanoparticles modified by PEG have
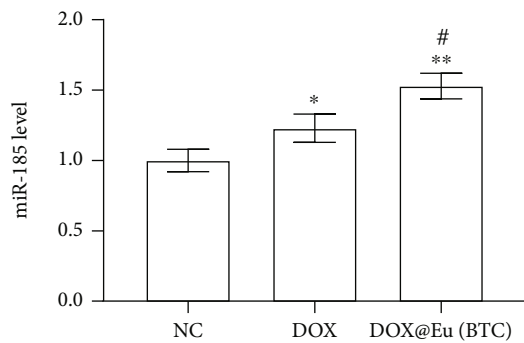
(a)
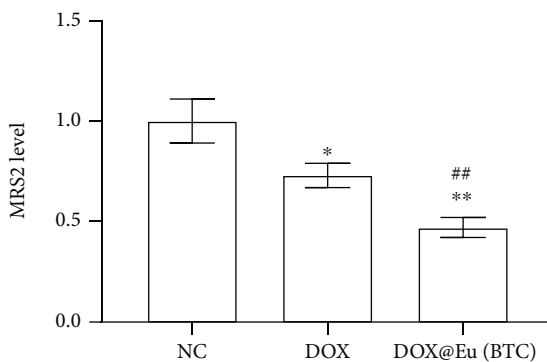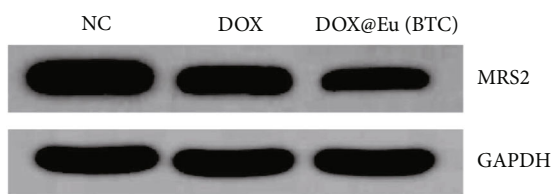
(b)
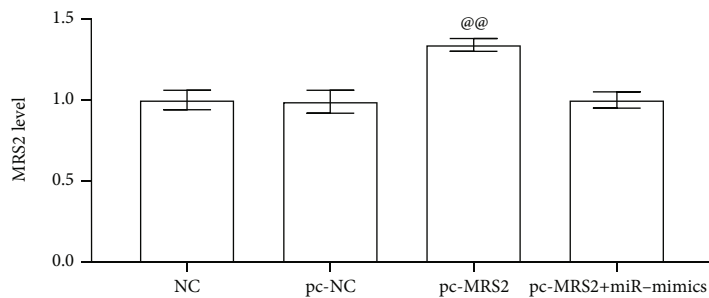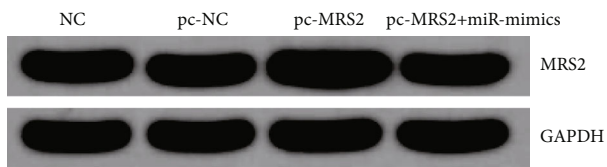
(c)
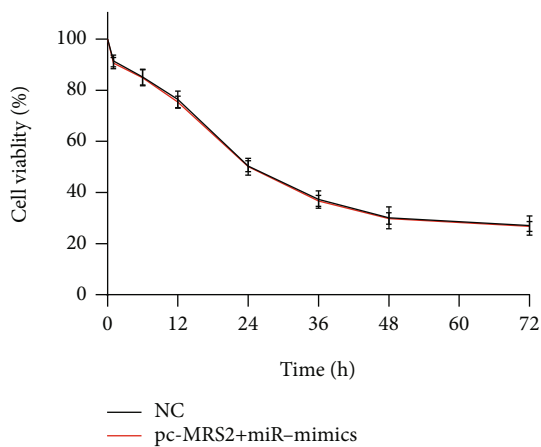
(d)

FIGURE 6: Continued.

(e)

(f)
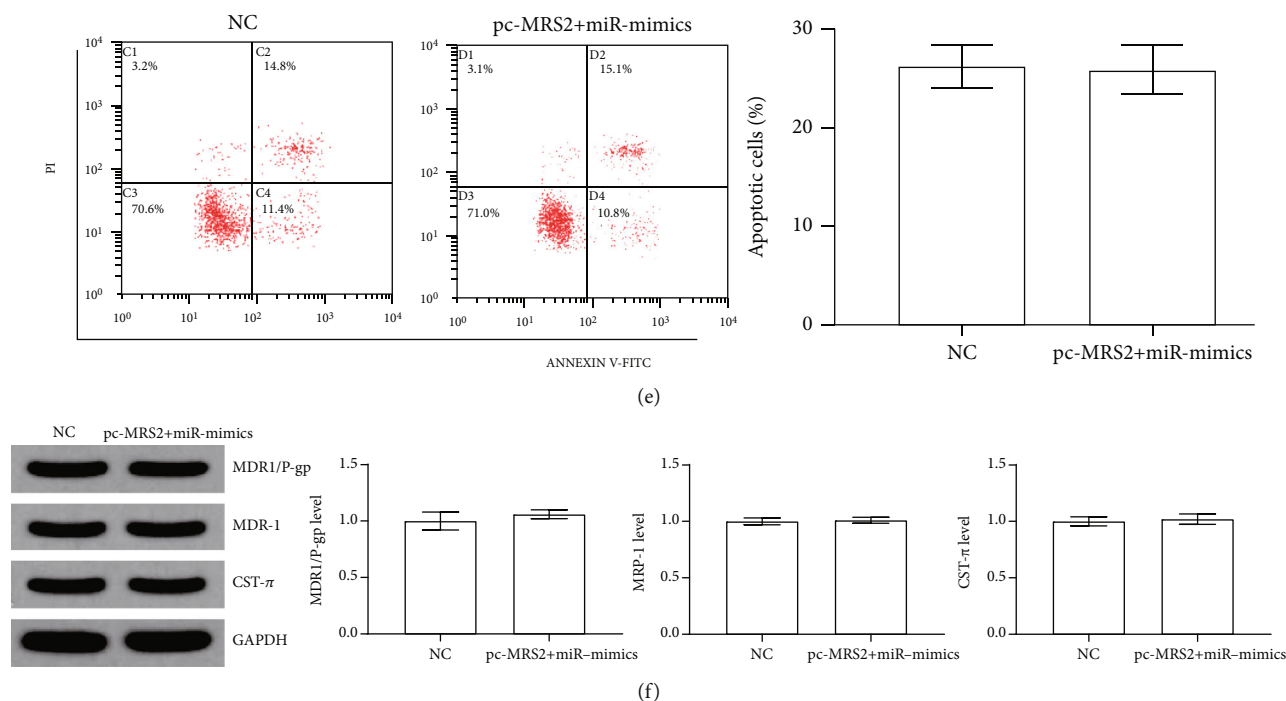
Figure 6: DOX@Eu (BTC) fluorescent nanoparticles enhance the chemotherapy sensitivity of SGC7901/ADR cells through miR-185/MRS2. $^*P < 0.05$ and $^{**}P < 0.01$ vs. NC group; $^\#P < 0.05$ and $^{\#\#}P < 0.01$ vs. DOX group. (a) The expression level of miR-185 in SGC7901/ADR cells. (b, c) The expression level of MRS2 in SGC7901/ADR cells. (d) Comparison of DOX@Eu (BTC) on cell viability SGC7901/ADR cell by different transfection. (e) Comparison of DOX@Eu (BTC) on cell apoptosis rate SGC7901/ADR cell by different transfection. (f) Comparison of DOX@Eu (BTC) on multidrug resistance protein relative expression SGC7901/ADR cell by different transfection.

become a better choice for nano-medicine carriers. Fluorescent EU (BTC) nanoparticles are modified by PEG to form a "molecular brush" on their surface, which improves the biocompatibility and prolongs the circulation time in the body without affecting the pore performance of fluorescent EU (BTC) nanoparticles. The specific surface area test of PEG-modified fluorescent EU (BTC) nanoparticles confirmed the above point of view. DOX is loaded on PEG-modified fluorescent EU (BTC) nanoparticles to obtain fluorescent DOX@Eu (BTC) nanoparticles. The results of laser confocal microscope observation showed that fluorescent DOX@Eu (BTC) nanoparticles are present in the cytoplasm of SGC7901/ADR cells or on the cell membrane, while DOX is fixed in EU (BTC) nanoparticles. Besides, the results of the thermogravimetric analysis showed that the effective drug loading of the nanoparticles was about 29%, which was much higher than the drug loading of traditional nano-medicine [20]. The ability to prevent the drug burst effect in the drug delivery system is an important index to evaluate its performance. Studies have shown that the pH of tumor tissue is usually between 5 and 6, which is acidic [21]. The in vitro release test results showed that the fluorescent DOX@Eu (BTC) nanoparticles prepared in this study have pH-responsive release performance, were not easy to release in a neutral environment, but can be released quickly in an acidic environment, which will not cause harm to normal tissues, and can ensure the concentration of the drug in the tumor tissue. In summary, the fluorescent DOX@Eu (BTC)

nanoparticles prepared in this study can target tumor tissues through high permeability and long retention effect, reduce the release of drugs in normal tissues, which can in turn reduce the side effects of chemotherapy drugs on patients, and enhance the killing effect of chemotherapy drugs on tumor tissues and cells. At the same time, the follow-up cell experiment results also showed that fluorescent DOX@Eu (BTC) nanoparticles have stronger cytotoxicity to SGC7901/ADR cells than free DOX, and enhanced the induction of SGC7901/ADR cell apoptosis. Also, it can effectively inhibit the expression of multidrug resistance protein in SGC7901/ADR cells.

miRNA is a noncoding single-stranded RNA molecule with a length of about 22 nucleotides, which is closely related to the multidrug resistance of tumor cells. Studies have shown that miR-185 is not only closely related to a variety of tumors but also related to the multidrug resistance of tumor cells. Xia et al. demonstrated that transfected miR-185 mimics could effectively reverse the multidrug resistance of SGC7901/ADR cells [11]. In this study, it was found that compared with the GES-1 cell line, the expression of miR-185 in SGC7901 and SGC7901/ADR cells was significantly reduced, and the expression in SGC7901/ADR cells was lower than that in SGC7901 cells. Transfection of miR-185 mimics can significantly enhance the toxicity of fluorescent DOX@Eu (BTC) nanoparticles to SGC7901/ADR cells, but significantly downregulate the expression of multidrug resistance protein. Human mitochondrial MRS2 protein (MRS2) is a magnesium transporter in the inner mitochondrial

membrane, responsible for the transportation of magnesium ions (Mg^{2+}) in the mitochondria. As one of the more abundant cations in cells, Mg^{2+} plays a role in cell apoptosis [22]. The homeostasis of Mg^{2+} in the body is mainly maintained by the expression of magnesium transporters. When the homeostasis of Mg^{2+} is destroyed, the prevalence of cancer will increase [23]. Studies have shown that the expression of Mg^{2+} in drug-resistant gastric cancer cell lines is significantly higher than that of nonresistant gastric cancer cell lines [24]. This study found that the expression of MRS2 protein in SGC7901 and SGC7901/ADR cell lines increased significantly, and the expression of MRS2 protein in SGC7901/ADR was significantly higher than that in SGC7901 cells. After the transfection of si-MRS2, the sensitivity of SGC7901/ADR to fluorescent DOX@Eu (BTC) nanoparticles was enhanced, and the inhibitory effect of fluorescent DOX@Eu (BTC) nanoparticles on the expression of multidrug resistance protein in SGC7901/ADR was also enhanced. Also, the bioinformatics prediction website showed that miR-185 has a targeted binding sequence with MRS2. The dual-luciferase reporter gene experiment confirmed that MRS2 was the downstream target gene of miR-185, and miR-185 negatively regulated the expression of MRS2. In summary, the expression level of miR-185 in SGC7901/ADR cells was reduced, but the expression of MRS2 protein in SGC7901/ADR cells was increased. miR-185 and MRS2 proteins are closely related to the multidrug resistance of SGC7901/ADR cells.

Further research found that after fluorescent DOX@Eu (BTC) nanoparticles treated SGC7901/ADR cells, the expression of miR-185 in the cells increased significantly, the expression of MRS2 protein decreased significantly, and the magnitude of the change was more obvious than that of DOX treatment. After transfection of miR-185 mimics and pc-MRS2 at the same time, the expression of MRS2 protein in SGC7901/ADR cells did not change significantly, and simultaneous transfection does not affect the sensitivity of SGC7901/ADR cells to fluorescent DOX@Eu (BTC) nanoparticles. In summary, DOX and fluorescent DOX@Eu (BTC) nanoparticles inhibited the translation of MRS2 protein by upregulating the expression of miR-185, thereby affecting the chemotherapy sensitivity of SGC7901/ADR cells.

The fluorescent DOX@Eu (BTC) nanoparticles constructed in this study have both high-drug loading, pH-sensitive release and fluorescence characteristics. While controlling the slow release of antitumor drugs, it may also have the function of imaging contrast agent. In the future, it has great potential in targeted therapy and imaging applications for the treatment of gastric cancer. However, due to time and experimental conditions and other constraints, this study only explored the effect and mechanism of DOX@Eu (BTC) fluorescent nanoparticles on drug-resistant gastric cancer cells within a certain range. The DOX@Eu (BTC) fluorescent nanoparticles have a large number of carboxyl groups on the surface. The modified carboxyl group combined with the pH-sensitive release function enables it to regulate the distribution of chemotherapeutic drugs in the patient's body, reduce the side effects of chemotherapeutic drugs on the patient, and increase the concentration of the drug at the tumor site. In the follow-up study, we will modify the carboxyl groups on the surface of DOX@Eu (BTC) fluorescent nanoparticles and explore its influence on the distribution of DOX in model animals.

In conclusion, the results of this study indicated that fluorescent DOX@Eu (BTC) nanoparticles can effectively enhance the chemotherapeutic sensitivity of SGC7901/ADR cells to DOX, and the mechanism of action may be achieved by further increasing the expression of miR-185 and inhibiting the expression of MRS2 protein.

Data Availability

The data used to support the findings of this study are included within the article.

Conflicts of Interest

The authors declare that there are no conflicts of interest regarding the publication of this paper.

Acknowledgments

References

[1] N. Bizzaro, A. Antico, and D. Villalta, "Autoimmunity and gastric cancer," *International Journal of Molecular Sciences*, vol. 19, no. 2, p. 377, 2018.

[2] R. Zheng, H. Zeng, S. Zhang, and W. Chen, "Estimates of cancer incidence and mortality in China, 2013," *Chinese Journal of Cancer*, vol. 36, no. 1, p. 66, 2017.

[3] W. H. Zhang, X. H. Song, X. Z. Chen et al., "Characteristics and survival outcomes related to the infra-pyloric lymph node status of gastric cancer patients," *World Journal of Surgical Oncology*, vol. 16, no. 1, p. 116, 2018.

[4] Q. W. Wang, X. T. Zhang, M. Lu, and L. Shen, "Impact of duration of adjuvant chemotherapy in radically resected patients with T4bN1-3M0/TxN3bM0 gastric cancer," *World J Gastrointest Oncol*, vol. 10, no. 1, pp. 31–39, 2018.

[5] M. Rugge, R. M. Genta, F. Di Mario et al., "Gastric cancer as preventable disease," *Clinical Gastroenterology and Hepatology*, vol. 15, no. 12, pp. 1833–1843, 2017.

[6] Y. Li, B.-b. Tan, L.-q. Fan, Q. Zhao, Y. Liu, and D. Wang, "Heterogeneity of COX-2 and multidrug resistance between primary tumors and regional lymph node metastases of gastric cancer," *Tumori*, vol. 98, no. 4, pp. 516–522, 2018.

[7] F. Zhu, Q. Wu, Z. Ni, C. Lei, T. Li, and Y. Shi, "miR-19a/b and MeCP2 repress reciprocally to regulate multidrug resistance in gastric cancer cells," *International Journal of Molecular Medicine*, vol. 42, no. 1, pp. 228–236, 2018.

[8] Y. Gu, J. Li, Y. Li et al., "Nanomicelles loaded with doxorubicin and curcumin for alleviating multidrug resistance in lung cancer," *International Journal of Nanomedicine*, vol. Volume 11, no. 11, pp. 5757–5770, 2016.

[9] M. Li, Y. Li, X. Huang, and X. Lu, "Captopril-polyethyleneimine conjugate modified gold nanoparticles for co-delivery of drug and gene in anti-angiogenesis breast cancer therapy," *Journal of Biomaterials Science. Polymer Edition*, vol. 26, no. 13, pp. 813–827, 2015.

[10] J. Zhong, R. K. Kankala, S. B. Wang, and A. Z. Chen, "Recent advances in polymeric nanocomposites of metal-organic frameworks (MOFs)," *Polymers (Basel)*, vol. 11, no. 10, p. 1627, 2019.

[11] D. Xia, X. Li, Q. Niu et al., "MicroRNA-185 suppresses pancreatic cell proliferation by targeting transcriptional coactivator with PDZ-binding motif in pancreatic cancer," *Experimental and Therapeutic Medicine*, vol. 15, no. 1, pp. 657–666, 2018.

[12] Y. Xiang, N. Ma, D. Wang et al., "MiR-152 and miR-185 co-contribute to ovarian cancer cells cisplatin sensitivity by targeting DNMT1 directly: a novel epigenetic therapy independent of decitabine," *Oncogene*, vol. 33, no. 3, pp. 378–386, 2014.

[13] B. Tan, Y. Li, Q. Zhao, L. Fan, and D. Wang, "ZNF139 increases multidrug resistance in gastric cancer cells by inhibiting miR-185," *Bioscience Reports*, vol. 38, no. 5, article BSR20181023, 2018.

[14] J. Shi, Y. Su, and Z. Zhang, "A nanoliposome-based photoactivable drug delivery system for enhanced cancer therapy and overcoming treatment resistance," *International Journal of Nanomedicine*, vol. 14, no. 5, pp. 1840-1841, 2018.

[15] B. Pelaz, C. Alexiou, R. A. Alvarez-Puebla et al., "Diverse applications of nanomedicine," *ACS Nano*, vol. 11, no. 3, pp. 2313–2381, 2017.

[16] L. He, Y. Liu, J. Lau et al., "Recent progress in nanoscale metal-organic frameworks for drug release and cancer therapy," *Nanomedicine (London, England)*, vol. 14, no. 10, pp. 1343–1365, 2019.

[17] D. Wang, C. Zhao, G. Gao, L. Xu, G. Wang, and P. Zhu, "Multifunctional NaLnF4@MOF-Ln nanocomposites with dual-mode luminescence for drug delivery and cell imaging," *Nanomaterials (Basel)*, vol. 9, no. 9, p. 1274, 2019.

[18] M. Sang, R. Luo, Y. Bai et al., "Mitochondrial membrane anchored photosensitive nano-device for lipid hydroperoxides burst and inducing ferroptosis to surmount therapy-resistant cancer," *Theranostics*, vol. 9, no. 21, pp. 6209–6223, 2019.

[19] I. Abánades Lázaro, S. Haddad, J. M. Rodrigo-Muñoz et al., "Mechanistic investigation into the selective anticancer cytotoxicity and immune system response of surface-functionalized, dichloroacetate-loaded, UiO-66 nanoparticles," *ACS Applied Materials & Interfaces*, vol. 10, no. 6, pp. 5255–5268, 2018.

[20] J. M. Lim, T. Cai, S. Mandaric et al., "Drug loading augmentation in polymeric nanoparticles using a coaxial turbulent jet mixer: Yong investigator perspective," *Journal of Colloid and Interface Science*, vol. 538, pp. 45–50, 2019.

[21] Y. X. Zhang, Y. Y. Zhao, J. Shen et al., "Nanoenabled modulation of acidic tumor microenvironment reverses anergy of infiltrating T cells and potentiates anti-PD-1 therapy," *Nano Letters*, vol. 19, no. 5, pp. 2774–2783, 2019.

[22] L. Merolle, G. Sponder, A. Sargenti et al., "Overexpression of the mitochondrial Mg channel MRS2 increases total cellular Mg concentration and influences sensitivity to apoptosis," *Metallomics*, vol. 10, no. 7, pp. 917–928, 2018.

[23] X. Zhu, M. J. Shrubsole, R. M. Ness et al., "Calcium/magnesium intake ratio, but not magnesium intake, interacts with genetic polymorphism in relation to colorectal neoplasia in a two-phase study," *Molecular Carcinogenesis*, vol. 55, no. 10, pp. 1449–1457, 2016.

[24] Y. Chen, X. Wei, P. Yan et al., "Human mitochondrial Mrs 2 protein promotes multidrug resistance in gastric cancer cells by regulating p 27, cyclin D1 expression and cytochrome C release," *Cancer Biology & Therapy*, vol. 8, no. 7, pp. 607–614, 2014.

Research Article

Surface Modification of a Stable CdSeZnS/ZnS Alloy Quantum Dot for Immunoassay

Jaehyun An,[1] Kim-Hung Huynh,[1] Yuna Ha,[1] Heung Su Jung,[2] Hyung-Mo Kim,[1] Dong-Min Kim,[1] Jaehi Kim,[1] Xuan-Hung Pham,[1] Dong-Eun Kim,[1] Jin-Nyoung Ho,[3] Sangchul Lee,[3] Ho-Young Lee,[4] Dae Hong Jeong,[5] and Bong-Hyun Jun [1]

[1]*Department of Bioscience and Biotechnology, Konkuk University, Seoul 143-701, Republic of Korea*
[2]*Company of GLOBAL ZEUS, Osan, Gyeonggi-do 18364, Republic of Korea*
[3]*Department of Urology, Seoul National University Bundang Hospital, Seoul 13620, Republic of Korea*
[4]*Department of Nuclear Medicine, Seoul National University Bundang Hospital, Seoul 13620, Republic of Korea*
[5]*Department of Chemistry Education, Seoul National University, Seoul 151-019, Republic of Korea*

Correspondence should be addressed to Bong-Hyun Jun; bjun@konkuk.ac.kr

Quantum dots (QDs) are powerful materials in various bioapplications based on their excellent optical and electronic properties. For the application of various fields of QDs, surface modification of QDs is necessary. However, surface modification in QDs may result in a reduction in quantum yield (QY). This reduction of QY causes many weaknesses in the biological application of QDs. In this study, CdSeZnS/ZnS alloy QDs were used to prepare antibody-conjugated QDs for a sandwich immunoassay. The alloy QDs displayed a QY of 84.5% that was maintained at 83.0% (98.2% of QY was maintained) after surface modification with the anti-rabbit IgG as a model study. Surface-modified QDs successfully detected their corresponding target through antibody-antigen binding. The limit of detection was $1.1 \times 10^2 \, \text{ng mL}^{-1}$ for rabbit IgG.

1. Introduction

Semiconductor quantum dots (QDs) are increasingly being used in both fundamental and applied research because of their optical and electronic properties [1–3]. QDs can absorb a broad range of light and emit the specific wavelength of light which depends on their size. With this property, one of the useful applications of QDs is fluorescent probes in biological imaging [4]. While traditional fluorescent probes have disadvantages such as easy photodegradation, low fluorescence, and photobleaching [5], QDs have excellent optical characteristics and chemical stability including higher photostability, wide band-edge absorption, narrow emission, and high quantum yield (QY) [6]. However, QDs also have limitations for bioapplication. Typically, QDs are dispersed only in nonpolar solvents and limited with severe intermittency in emission. Furthermore, their nonspecific binding can lead to

misinterpretation of experimental results. The critical issue of QDs is toxicity which can cause acute or chronic diseases. Another issue of QDs is their instability in biological media because of their high hydrophobic property. Thus, surface modification is required to make QDs which have hydrophilic characteristic and more stable in a biological environment [7–14].

Many studies have been sought to overcome these limitations of QDs. The hydrophobic surface of QDs was changed as a hydrophilic surface via encapsulation with a silica shell, and these silica encapsulated QDs were more suitable for biomedical applications compared to bare QDs [7, 15–19]. Amphiphilic polymer-covered QDs displayed improved stability over a wide pH range and were less prone to nonspecific binding [20, 21]. Studies which aimed at enhancing the safety of QDs described that a thick shell of ZnS could reduce QDs' toxicity to cells and increase photoluminescence.

Moreover, the thick shell of ZnS makes the fluorescence quantum yield more stable and decrease the blinking, and it extends the absorption and emission spectrum [2, 22–26].

Enzyme-linked immunosorbent assay (ELISA) is a biochemical method for detecting or measuring a molecule, mostly a protein. It is based on the antigen-antibody reaction which has been applied in various different fields such as diagnosis, toxicology, food industry, pharmaceutical industry, immunology, and vaccine development [27]. ELISA possesses advantages that include high sensitivity, specificity, and fast reaction, but it also has many disadvantages such as size limitations, disposal of sensitivity to temperature, and easy decay. To overcome these weaknesses, enormous innovations such as ultrasensitive enzymes and better antibodies have been developed. As good fluorescence probes, QDs were utilized for signal enhancement [28–32].

In many studies, CdSe/ZnS core/shell QDs were fabricated and applied in biological detection [33–42]. Li's group synthesized CdSe/ZnS QDs and proceeded an assay for the detection of C-reactive protein (CRP). The test for CRP detection in the above study had good detection results, but the QY of QDs was 63% in hydrophobic modification and the QY showed an 8% reduction after hydrophilic modification [43]. For another study, the protein was introduced on CdSe/ZnS QDs. The particle that conjugated with antibody was identified with luminescence images on various proteins and compared the efficiency of each particle. It was a good result in biological application. However, in the case of QY of CdSe/ZnS QDs used in the above paper, it was 35-50% before the ligand exchange, and the QY after ligand exchange was not checked correctly [44]. In general, QDs showed a sharp decrease in QY after ligand exchange, so maintaining QY which is not dropped significantly after surface modification is needed [45–47].

In this study, we fabricated a cadmium selenide zinc sulfide/zinc sulfide (CdSeZnS/ZnS) alloy QDs that displayed a high QY which was 84.5%; after surface modification, QY was 83.0% (98.2% of QY was maintained). The surface of alloy QDs was modified via conjugation with antibody molecules, and commercial QDs were used as a control. The conjugation of the commercial QDs markedly reduced QY. By contrast, alloy QDs retained a high QY after surface modification and then were successful in sensitive detecting rabbit IgG. The results indicated that alloy QDs have better stability in QY and better capability in bioconjugation than commercial QDs.

2. Materials and Methods

2.1. Chemical and Materials.
All reagents were used as received from the suppliers without further purification. Cadmium oxide (CdO, 99.9%) was purchased from Alfa Aesar (Ward Hill, MA, USA). Tri-n-octylphosphine (TOP, 97%) was purchased from STREM Chemicals (Newburyport, MA, USA). Selenium (Se, 99.5%) was purchased from Acros Organics (Geel, Belgium). Sulfur (S, 99%) and ammonium hydroxide (NH_4OH, 27%) were purchased from Daejung (Siheung, Korea). Zinc acetate ($Zn(Ac)_2$, 99.99%), 3-mercaptopropionic acid (MPA), oleic acid

(OA, 90%), 1-octadecene (ODE, 90%), 1-octanethiol (98.5%), acetone (99.9%), chloroform ($CHCl_3$, 99.5%), 1-ethyl-3-(3-dimethylaminopropyl) carbodiimide (EDC), sulfo-N-hydroxysulfosuccinimide (sulfo-NHS), phosphate-buffered saline (PBS, pH 7.4), TWEEN® 20, bovine serum albumin (BSA), and commercial QDs (CdSeS/ZnS-alloyed quantum dot) [48] were purchased from Sigma-Aldrich (St. Louis, MO, USA). NH_2-PEG-COOH (MW 600) was purchased from NANOCS. Rabbit immunoglobulin G (IgG) and anti-rabbit IgG antibody were purchased from Bore Da Biotech Co. (Seongnam, Korea). QE-2000 (Otsuka Electronics Co., Ltd.) was used to measure the QY of alloy QDs.

2.2. Preparation of Alloy QDs.
Hydrophobic QDs were prepared by mixing 75 mL of ODE and 15 mL of OA and adding 1.1 g $Zn(Ac)_2$ and 0.384 g of CdO in a three-necked flask, and the mixture was incubated under a vacuum at 150°C for 1 h. After 1 h, moisture in the flask was removed and the flask was heated to 300°C in the presence of nitrogen gas, with the addition of 0.6 mL of TOP and 0.048 g of Se for 3 min. This was followed by the addition of 0.5 mL of 1-dodecanethiol and reaction for 20 min. Three milliliters of TOP and 0.192 g of sulfur were added to the flask and reacted for 10 min, followed by 1 mL of 1-dodecanethiol and reacted for another 10 min. The flask was then cooled to room temperature. The QDs were washed in acetone and dispersed in $CHCl_3$. The hydrophobic alloy QDs were prepared by mixing 60 mL of ODE and 10 mL of OA, with the addition of 1.1 g $Zn(Ac)_2$ and 0.384 g of CdO in a three-necked flask under a vacuum at 150°C for 1 h. Moisture was removed, the flask was heated to 300°C in the presence of nitrogen gas, the prepared hydrophobic QDs were added, and the reaction was allowed to proceed for 10 min. Three milliliters of TOP and 0.192 g of S were added and reacted for 10 min, and the flask was cooled to room temperature. The alloy QDs were washed in acetone and dispersed in $CHCl_3$.

2.3. Characterization of QDs.
The photoluminescence quantum efficiency of heat-treated specimens excited at 390 nm was measured using a quantum efficiency measurement system (QE-2000, Otsuka Electronics Co., Ltd.). While measuring the quantum efficiency, the emission and excitation sources were also collected by the integrated spheres.

2.4. Ligand Exchange of QDs.
Ligands of alloy QD and commercial QD were exchanged using the carboxyl group-contained ligands as per a previous description for modification. First, the reaction solution containing 1.0 mL of MPA, 1 mL of NH_4OH, and 30 mL of $CHCl_3$ was prepared in a Falcon tube, which was mixed by rotation for 2 h. Then, 10 mg of each QD, 10 mL of distilled water, and 10 mL of reaction buffer were mixed in a Falcon tube and allowed to react by rotation for 2 h. The supernatant was collected and was washed several times with $CHCl_3$. After alloy QD ligands were exchanged with the carboxyl group, they were washed with acetone and then passed through an Amicon filter-sized 100,000 MWCO and dispersed in distilled water.

2.5. Preparation of Anti-Rabbit IgG-Conjugated QDs.
The carboxyl group-functionalized commercial QDs or alloy
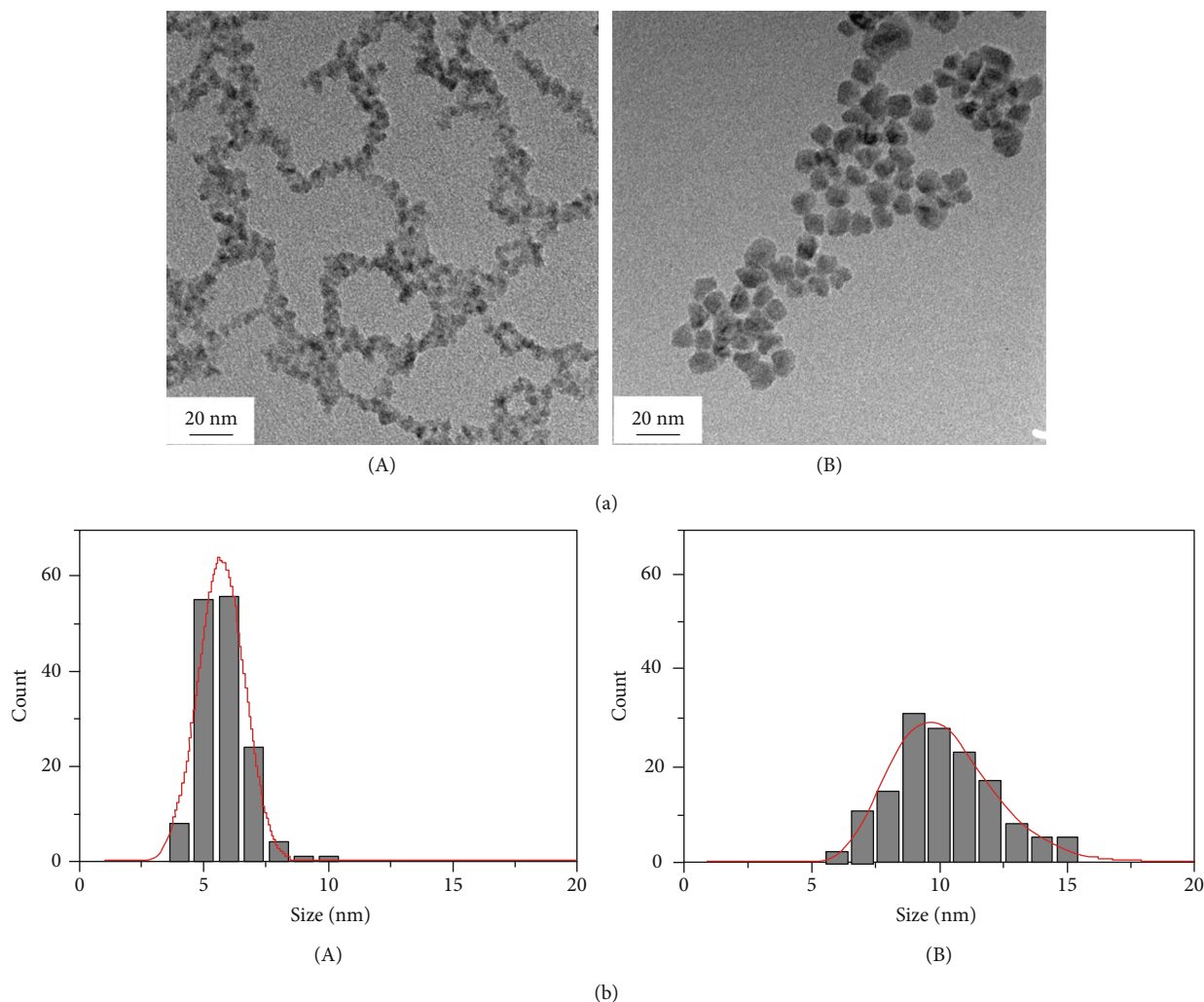
FIGURE 1: (a) TEM image of bare QDs: (A) commercial QDs; (B) alloy QDs. (b) Size distribution and relative standard deviation plot for each QDs: (A) commercial QDs; (B) alloy QDs.

QDs ($1.0\,\text{mg}\,\text{mL}^{-1}$ in deionized water) were incubated with sulfo-NHS (2 mg), EDC (2 mg), and PBS buffer for 30 min at 25°C to activate the carboxyl groups. The reaction mixture was washed several times with PBS buffer and centrifuged at 13,000 rpm for 10 min at 4°C. Then, it was incubated with NH_2-PEG-COOH ($10\,\mu\text{L}$) for 2 h at 25°C, and unreacted carboxyl groups were blocked with ethanolamine ($3.2\,\mu\text{L}$) for 30 min at 25°C. After repeating the process of leading to sulfo-NHS, EDC, NH_2-PEG-COOH, and ethanolamine once again to prevent steric hindrance that occurred immunoassay experiment, the QDs were reacted with anti-rabbit IgG ($15\,\mu\text{g}$) for 1 h at 25°C. The reaction mixture was washed several times with PBS and centrifuged at 13,000 rpm for 10 min at 4°C. The sulfo-NHS-activated QDs were reacted with anti-rabbit IgG ($15\,\mu\text{g}$) for 1 h at 25°C. The reaction mixture was washed with PBS containing 0.1 wt.% TWEEN® 20 and centrifuged at 13,000 rpm for 10 min at 4°C, and antibody-conjugated QDs were redispersed in PBS containing 5.0 wt.% BSA for 2 h at 25°C to prevent nonspecific binding. The solution was washed several times with PBS

containing 0.1 wt.% TWEEN® 20, centrifuged at 13,000 rpm for 10 min at 4°C, and redispersed in PBS.

2.6. QD-Based Sandwich Immunoassay for Detection of Rabbit IgG.

The assay was performed in 96-well immune plates (SPL Life Science Co., Ltd, Seoul, Korea). First, $1.0 \times 10^5\,\text{ng}\,\text{mL}^{-1}$ of antibody in PBS, as the capture antibody of IgG (target), was added to the wells. After incubation for 1 h with shaking the plate at 25°C, the plate was stored overnight at 4°C. To remove the unbound antibody, each microwell was washed three times with PBS ($300\,\mu\text{L}\,\text{well}^{-1}$). This step was followed by adding 0.5 wt.% BSA solution to the microwells ($300\,\mu\text{L}\,\text{well}^{-1}$) and incubating for 2 h at 25°C. Then, the BSA solution was removed and wells were washed three times using PBS containing 0.1 wt.% TWEEN® 20 ($300\,\mu\text{L}\,\text{well}^{-1}$). Next, $100\,\mu\text{L}$ of target (rabbit IgG) solution with corresponding concentrations was added to the microwells. The microplate was incubated for 2 h at 37°C, followed by three washes with PBS containing 0.1 wt.% TWEEN® 20 ($300\,\mu\text{L}\,\text{well}^{-1}$). IgG antibody-conjugated QDs (2.0×10^5
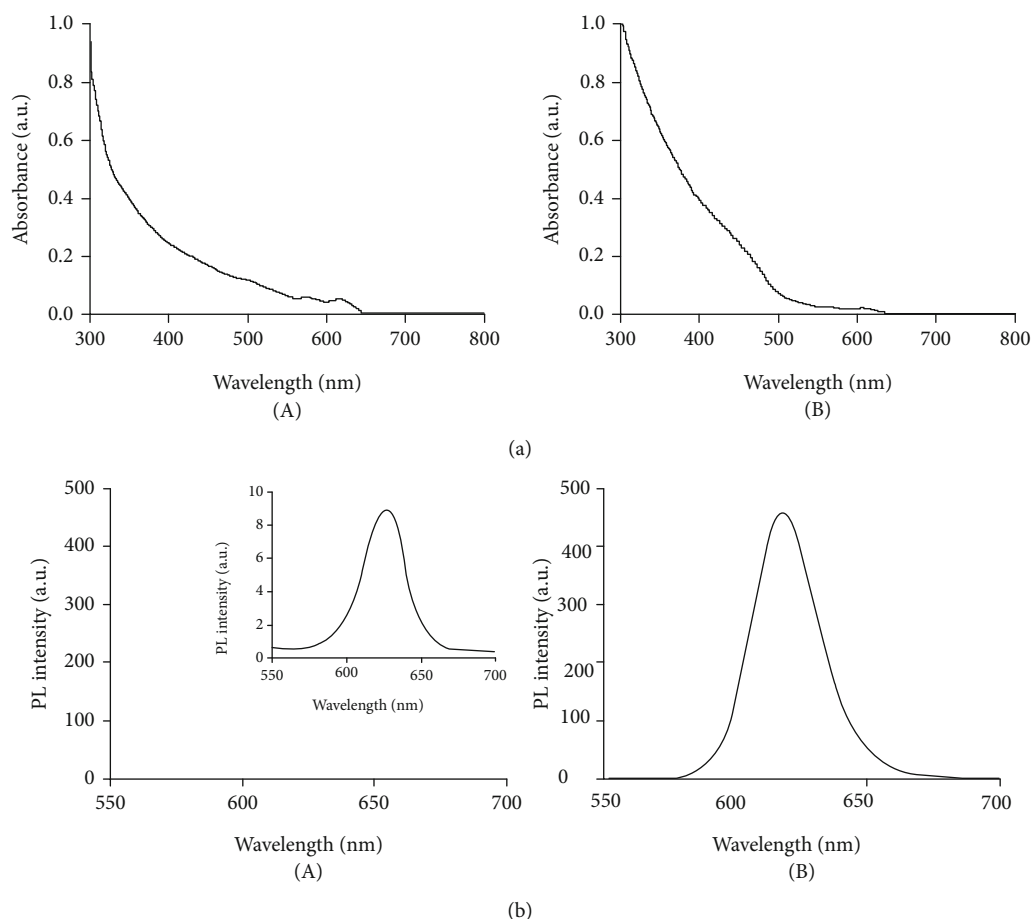
FIGURE 2: (a) UV-Vis absorbance of two kinds of QDs: (A) antibody-conjugated commercial QDs; (B) antibody-conjugated alloy QDs. (b) photoluminescence intensity of antibody-conjugated QDs at 550–700 nm: (A) commercial QDs (inlet: an enlarged image of measured PL intensity); (B) alloy QDs.

ng mL^{-1}) were added to each microwell and incubated for 2 h at 37°C. Then, we washed the microwell three times using PBS containing 0.1 wt.% TWEEN® 20 (300 μL well^{-1}) and 300 μL of PBS was added into each microwell. After the immunoassay experiment, fluorescence intensity was measured (excitation wavelength filter was used to 385 nm; emission wavelength filter was used to 630 nm).

3. Results and Discussion

3.1. Synthesis and Characterization of Anti-Rabbit IgG Antibody-Conjugated QDs. Our new alloy QDs was established via three strategies to improve the final stability of particles. First, the method of depositing a secondary shell after the primary refining core was used in the core synthesis method of the alloy QDs. Second, the ligand of the primary shell in the synthetic method was applied with a mixture of various thiol-contained ligands (1-octanethiol, 1-dodeca-nethiol, 1-decanrthiol...) which reduced the lattice mismatch in the next response to increase the stability of the core in the alloy QDs. Third, in the synthetic method, the precursor of the shell was added sequentially to enhance particle stability.

Figure 1(a) shows a representative transmission electron microscopy image of bare QDs, and Figure 1(b) shows QD

size distribution, respectively. The average size of commercial QDs was 5.6 ± 1.0 nm, and its relative standard deviation was 0.16. The average size of alloy QDs was 10.1 ± 2.1 nm, and its relative standard deviation was 0.21. They were also sized through DLS with water as a solvent (Figures S1 and S2).

The surfaces of QDs were functionalized with MPA to produce a hydrophilic surface with carboxyl groups. To conjugate an antibody, the carboxyl groups were activated using EDC and sulfo-NHS. To evaluate the quality of two kinds of antibody-conjugated QDs, ultraviolet-visible (UV-Vis) absorbance, fluorescence intensity, zeta potential, and QY examination were performed at the same concentrations. The UV-Vis absorbance at 300-400 nm was higher in alloy QDs than in commercial QDs (Figure 2(a)). Fluorescence intensity was measured at an emission and excitation wavelength of 385 nm and 600–650 nm in 0.05 mg mL^{-1} of QD concentration, respectively (Figure 2(b)). As a result of comparing fluorescence intensity at the same concentration, the fluorescence intensity of alloy QDs was relatively stronger than that of commercial QDs. To confirm the anti-rabbit IgG antibody conjugation, we compared the QY and zeta potential of carboxyl group-functionalized QDs and antibody-conjugated QDs. After conjugating antibodies to QDs, QY was measured to determine how different the efficiency of
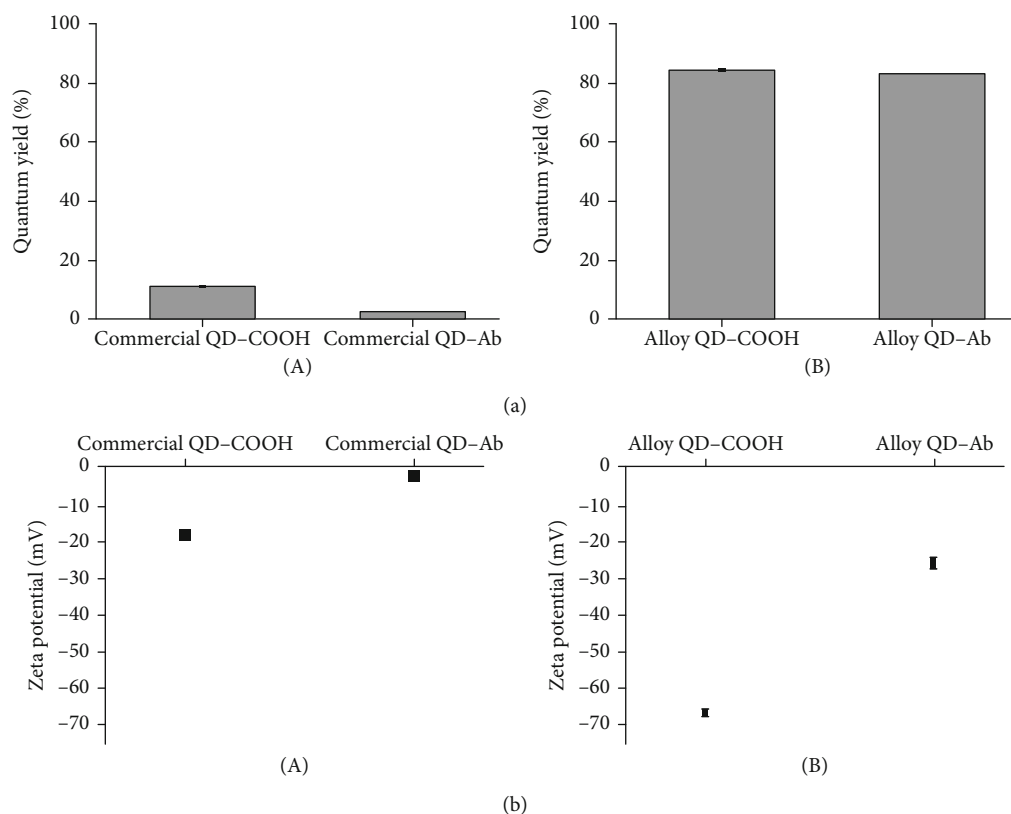
FIGURE 3: Comparison between 2 kinds of anti-rabbit IgG antibody-conjugated QDs. (a) Quantum yield comparison between carboxyl group-functionalized and antibody-conjugated QDs: (A) commercial QDs; (B) alloy QDs. (b) Zeta potential comparison between carboxyl group-functionalized and antibody-conjugated QDs: (A) commercial QDs; (B) alloy QDs.

commercial QDs and alloy QDs were. Carboxyl group-functionalized commercial QDs displayed a relatively low level of QY at 11.3%, with QY decreasing to 2.5% after antibody conjugation. On the other hand, carboxyl group-functionalized alloy QDs displayed a high QY of 84.5%, and this high QY was maintained even after antibody conjugation (83.0%) (Figures 3(a) and S3).

Before antibody conjugation, both QDs showed a higher negative charge due to the carboxyl group on the surface, whereas antibody-conjugated QDs showed less negative charge due to the antibody on the surface (Figure 3(b)). These findings indicated that the antibodies were successfully conjugated onto the surface of carboxyl group-functionalized QDs.

Additionally, cell viability experiments were conducted to confirm the suitability of biological experiments and particle stability of alloy QDs and common QDs (Figure S4). The results indicated the superiority of alloy QDs, which were used in further experiments.

3.2. QD-Based Sandwich Immunoassay Strategy. The anti-rabbit IgG antibody was used as a capture antibody, and it was used to the detection of rabbit IgG as target. The capture antibody was attached to the wells of high-binding immune plates through physical absorption. BSA was used to block the uncoated active sites to prevent nonspecific adsorption of the target in microplates. Different concentrations of the target were added for testing. Subsequently, detection

antibody-conjugated QDs were bound with the target-capture antibody complex and formed the sandwich immunocomplex. As the decreased target concentration, the amount of capture antibody-conjugated QDs which bound as sandwich immunocomplex was also decreased, and as a result, the fluorescence intensity declined. Thus, it was feasible to determine the concentration of the target by monitoring the fluorescence intensity.

3.3. Optimization of Antibody-Conjugated QD Concentration. To get the optimized concentration of QDs (for sandwich immunoassay), we set the concentration of detection antibody- (anti-rabbit IgG) conjugated alloy QD variously between 0 and 1.0×10^7 ng mL^{-1}. The experiment group proceeded with the capture antibody, target antibody, and detection antibody-conjugated QDs. Control group 1 used alloy QD-conjugated antibody and capture antibody, without target. Control group 2 used alloy QD-conjugated antibody and target, without capture antibody. The concentration of both capture antibody and target antibody was not changed during optimizing the concentration of detection antibody-conjugated QDs. As shown in Figure 4, we performed sandwich immunoassay and achieved strong fluorescence intensity at the experiment group, meanwhile weak fluorescence intensity at the control group. Weak fluorescence intensity of the control group is indicated for proving nonspecific binding. Consequentially, we confirmed that there was distinct fluorescence intensity at the experiment group and no
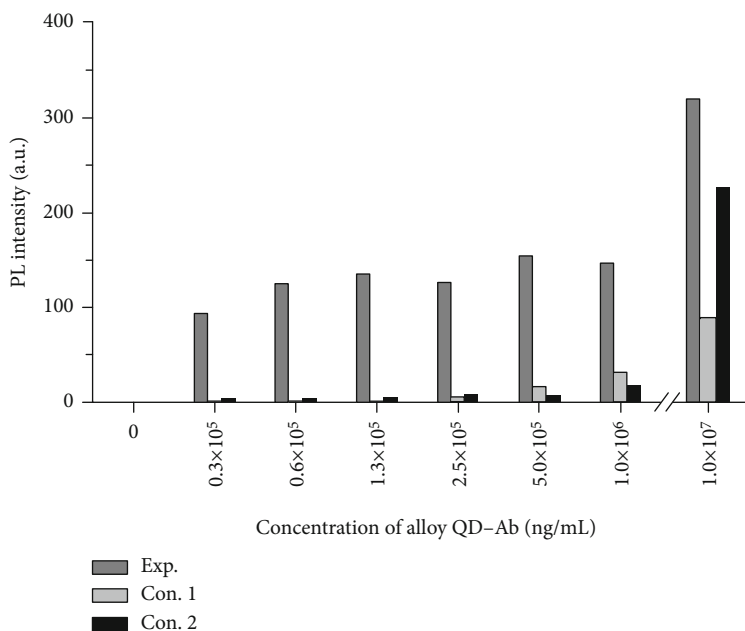
FIGURE 4: Fluorescence intensity to achieve the concentration of antibody-conjugated QDs. Compared with the experiment group, the target antibody was absent in control group 1 and the capture antibody was absent in control group 2.
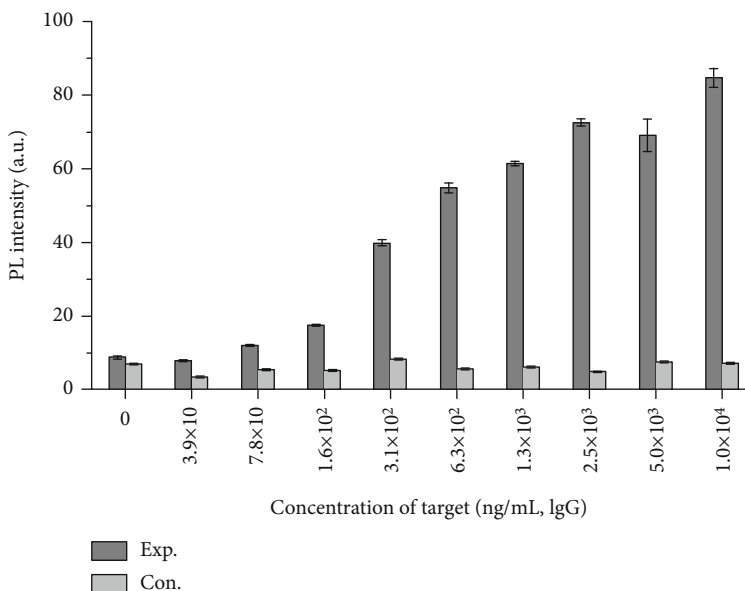
FIGURE 5: Fluorescence intensity of anti-rabbit IgG antibody-conjugated alloy QDs for rabbit IgG detection. Compared with the experiment group, the target was absent in the control group.

significant nonspecific binding at control group 1 below the 2.5×10^5 ng mL^{-1} of detection antibody-conjugated QDs. So, the concentration of detection antibody-conjugated QDs was optimized as 2.5×10^5 ng mL^{-1}, and QDs with optimized concentration were used by the same concentration (2.5×10^5 ng mL^{-1}) for the rabbit IgG detection experiment.

3.4. Performance of the Sandwich Immunoassay Using Alloy QDs for Rabbit IgG Detection. Under the optimized condition of detecting anti-rabbit IgG antibody-conjugated QDs (2.5×10^5 ng mL^{-1} of detection antibody-conjugated QDs),

we performed the sandwich immunoassay experiment for detecting of the rabbit IgG. To determine the limit of detection (LOD) of the rabbit IgG, the concentration of rabbit IgG was increased gradually from 0 (PBS buffer only) to 1.0 $\times 10^4$ ng mL^{-1}. The fluorescence intensity was gradually increased according to the increase of rabbit IgG concentration. Meanwhile, in the control group in which the capture antibody was absent, fluorescence intensity was almost the same at all concentrations of rabbit IgG. The maximum fluorescence intensity of both the experimental and control groups was compared to achieve the limit of detection; the

LOD for the rabbit IgG was 1.1×10^2 ng mL^{-1} (3 S/N criteria) (Figures 5 and S5). Although these sensitivities were not exceptional [49], the results are important as they were the demonstration of the potential biological applications of new alloy QDs that QY was rarely dropped after surface modification. Alloy QDs could have diverse uses due to their remarkably bright fluorescence.

4. Conclusions

We fabricated the alloy QDs which have a high QY of 84.5%, and their ligand has a carboxyl group that can easily be used and versatile in surface modification. After surface modification, the alloy QDs have a QY of 83%. We compared the optical characteristics between commercial QDs and alloy QDs. The QY of commercial QDs decreased sharply after surface modification from 11.3% to 2.5%, whereas the QY of alloy QDs was stable even after surface modification. These results indicate that alloy QDs are more applicable than commercial QDs. Further experiments established the bioapplication of alloy QDs. In a sandwich immunoassay to detect rabbit IgG, the LOD was 1.1×10^2 ng mL^{-1}. Combining these results, alloy QDs are more suitable for bioapplication than commercial QDs and have the potential for development.

Data Availability

The data used to support the findings of this study are available from the corresponding author upon request.

Conflicts of Interest

The authors declare that there is no conflict of interest regarding the publication of this paper.

Authors' Contributions

Jaehyun An and Kim-Hung Huynh are co-first authors.

Acknowledgments

Supplementary Materials

Figure S1 shows the DLS analysis result of alloy QDs. For the alloy QDs, the size of the particles in the water solvent was measured at 25.8 nm. Figure S2 shows the DLS analysis result of commercial QDs. For the commercial QDs, the size of the particles in the water solvent was measured at 762.3 nm. Figure S3 checked the digital image of each QDs. Prior to the conjugation of antibodies, the original alloy QDs had the strongest fluorescence intensity in the image. Figure S4 shows cell viability assay to assess cytotoxicity of alloy QDs. Human retinal pigment epithelial ARPE-19 cells were treated with various concentrations of alloy QDs or conventional QDs. Figure S5 shows LOD calculation. We used 3 S/N criteria to calculate LOD. (Supplementary Materials)

References

[1] M. Frasco and N. Chaniotakis, "Semiconductor quantum dots in chemical sensors and biosensors," Sensors, vol. 9, no. 9, pp. 7266–7286, 2009.

[2] A. R. AbouElhamd, K. al-Sallal, and A. Hassan, "Review of core/shell quantum dots technology integrated into building's glazing," Energies, vol. 12, no. 6, article 1058, 2019.

[3] D. Mocatta, G. Cohen, J. Schattner, O. Millo, E. Rabani, and U. Banin, "Heavily doped semiconductor nanocrystal quantum dots," Science, vol. 332, no. 6025, pp. 77–81, 2011.

[4] H. R. Chandan, J. D. Schiffman, and R. G. Balakrishna, "Quantum dots as fluorescent probes: synthesis, surface chemistry, energy transfer mechanisms, and applications," Sensors and Actuators B: Chemica, vol. 258, pp. 1191–1214, 2018.

[5] I. L. Medintz, H. T. Uyeda, E. R. Goldman, and H. Mattoussi, "Quantum dot bioconjugates for imaging, labelling and sensing," Nature Materials, vol. 4, no. 6, pp. 435–446, 2005.

[6] Z. Pan, K. Zhao, J. Wang, H. Zhang, Y. Feng, and X. Zhong, "Near infrared absorption of CdSexTe1–x alloyed quantum dot sensitized solar cells with more than 6% efficiency and high stability," ACS Nano, vol. 7, no. 6, pp. 5215–5222, 2013.

[7] Y. Ha, H. S. Jung, S. Jeong et al., "Fabrication of remarkably bright QD densely-embedded silica nanoparticle," Bulletin of the Korean Chemical Society, vol. 40, no. 1, pp. 9–13, 2019.

[8] A. Foubert, N. V. Beloglazova, A. Rajkovic et al., "Bioconjugation of quantum dots: review & impact on future application," Trac-Trends in Analytical Chemistry, vol. 83, pp. 31–48, 2016.

[9] D. Kalinowska, I. Grabowska-Jadach, M. Drozd, and M. Pietrzak, "Comparative studies of biological activity of cadmium-based quantum dots with different surface modifications," Applied Nanoscience, vol. 8, no. 3, pp. 309–321, 2018.

[10] M. Abdelhameed, D. R. Martir, S. Chen et al., "Tuning the optical properties of silicon quantum dots via surface functionalization with conjugated aromatic fluorophores," Scientific Reports, vol. 8, no. 1, article 3050, 2018.

[11] N. Bajwa, N. K. Mehra, K. Jain, and N. K. Jain, "Pharmaceutical and biomedical applications of quantum dots," Artificial Cells, Nanomedicine, and Biotechnology, vol. 44, no. 3, pp. 758–768, 2016.

[12] R. D. Singh, R. Shandilya, A. Bhargava et al., "Quantum dot based nano-biosensors for detection of circulating cell free miRNAs in lung carcinogenesis: from biology to clinical translation," Frontiers in Genetics, vol. 9, p. 616, 2018.

[13] D. H. Ren, B. Wang, C. Hu, and Z. You, "Quantum dot probes for cellular analysis," Analytical Methods, vol. 9, no. 18, pp. 2621–2632, 2017.

[14] D. Yoo, Y. Park, B. Cheon, and M. H. Park, "Carbon dots as an effective fluorescent sensing platform for metal ion detection," Nanoscale Research Letters, vol. 14, no. 1, p. 272, 2019.

[15] V. V. Goftman, T. Aubert, D. V. Ginste et al., "Synthesis, modification, bioconjugation of silica coated fluorescent quantum dots and their application for mycotoxin detection," Biosensors & Bioelectronics, vol. 79, pp. 476–481, 2016.

[16] B. H. Jun, D. W. Hwang, H. S. Jung et al., "Ultrasensitive, biocompatible, quantum-dot-embedded silica nanoparticles for bioimaging," *Advanced Functional Materials*, vol. 22, no. 9, pp. 1843–1849, 2012.

[17] S. Kyeong, C. Jeong, H. Y. Kim et al., "Fabrication of mono-dispersed silica-coated quantum dot-assembled magnetic nanoparticles," *RSC Advances*, vol. 5, no. 41, pp. 32072–32077, 2015.

[18] D. Drozd, H. Zhang, I. Goryacheva, S. De Saeger, and N. V. Beloglazova, "Silanization of quantum dots: challenges and perspectives," *Talanta*, vol. 205, article 120164, 2019.

[19] O. A. Goryacheva, C. Guhrenz, K. Schneider et al., "Silanized luminescent quantum dots for the simultaneous multicolor lateral flow immunoassay of two mycotoxins," *ACS Applied Materials & Interfaces*, vol. 12, no. 22, pp. 24575–24584, 2020.

[20] E. S. Speranskaya, N. V. Beloglazova, P. Lenain et al., "Polymer-coated fluorescent CdSe-based quantum dots for application in immunoassay," *Biosensors & Bioelectronics*, vol. 53, pp. 225–231, 2014.

[21] S. Kyeong, H. Kang, J. Yim et al., "Quantum dot-assembled nanoparticles with polydiacetylene supramolecule toward label-free, multiplexed optical detection," *Journal of Colloid and Interface Science*, vol. 394, pp. 44–48, 2013.

[22] M. Chern, T. T. Nguyen, A. H. Mahler, and A. M. Dennis, "Shell thickness effects on quantum dot brightness and energy transfer," *Nanoscale*, vol. 9, no. 42, pp. 16446–16458, 2017.

[23] M. Grabolle, J. Ziegler, A. Merkulov, T. Nann, and U. Resch-Genger, "Stability and fluorescence quantum yield of CdSe–ZnS quantum dots—influence of the thickness of the ZnS shell," *Annals of the New York Academy of Sciences*, vol. 1130, no. 1, pp. 235–241, 2008.

[24] J. Vela, H. Htoon, Y. Chen et al., "Effect of shell thickness and composition on blinking suppression and the blinking mechanism in 'giant' CdSe/CdS nanocrystal quantum dots," *Journal of Biophotonics*, vol. 3, no. 10-11, pp. 706–717, 2010.

[25] D. Li, J. Bai, T. Zhang et al., "Blue quantum dot light-emitting diodes with high luminance by improving the charge transfer balance," *Chemical Communications*, vol. 55, no. 24, pp. 3501–3504, 2019.

[26] X. Jin, K. Xie, T. Zhang et al., "Cation exchange assisted synthesis of ZnCdSe/ZnSe quantum dots with narrow emission line widths and near-unity photoluminescence quantum yields," *Chemical Communications*, vol. 56, no. 45, pp. 6130–6133, 2020.

[27] S. Hosseini, P. Vázquez-Villegas, M. Rito-Palomares, and S. O. Martinez-Chapa, "General overviews on applications of ELISA," in *Enzyme-Linked Immunosorbent Assay (ELISA)*, SpringerBriefs in Applied Sciences and Technology, pp. 19–29, Springer, Singapore, 2018.

[28] S. K. Vashist and J. H. T. Luong, "Chapter 1 - immunoassays: an overview," in *Handbook of Immunoassay Technologies*, S. K. Vashist and J. H. T. Luong, Eds., pp. 1–18, Academic Press, 2018.

[29] J. Amani, S. A. Mirhosseini, and A. A. Imani Fooladi, "A Review of Approaches to Identify Enteric Bacterial Pathogens," *Jundishapur Journal of Microbiology*, vol. 8, no. 2, article e17473, 2014.

[30] M. S. Draz and H. Shafiee, "Applications of gold nanoparticles in virus detection," *Theranostics*, vol. 8, no. 7, pp. 1985–2017, 2018.

[31] X. Pei, B. Zhang, J. Tang, B. Liu, W. Lai, and D. Tang, "Sandwich-type immunosensors and immunoassays exploiting nanostructure labels: a review," *Analytica Chimica Acta*, vol. 758, pp. 1–18, 2013.

[32] S. Sakamoto, W. Putalun, S. Vimolmangkang et al., "Enzyme-linked immunosorbent assay for the quantitative/qualitative analysis of plant secondary metabolites," *Journal of Natural Medicines*, vol. 72, no. 1, pp. 32–42, 2018.

[33] M. Čadková, V. Dvořáková, R. Metelka, Z. Bílková, and L. Korecká, "Verification of antibody labelling efficiency as an important step in ELISA/QLISA development," *Monatshefte für Chemie-Chemical Monthly*, vol. 147, no. 1, pp. 69–73, 2016.

[34] D. Gomes, M. Algarra, M. J. Diez de los Rios et al., "CdSe and ZnSe quantum dots capped with PEA for screening C-reactive protein in human serum," *Talanta*, vol. 93, pp. 411–414, 2012.

[35] J. Li, M. Mao, F. Wu, Q. Li, L. Wei, and L. Ma, "Amino-functionalized CdSe/ZnS quantum dot-based lateral flow immunoassay for sensitive detection of aflatoxin B1," *Analytical Methods*, vol. 10, no. 29, pp. 3582–3588, 2018.

[36] Y. Lv, F. Wang, N. Li et al., "Development of dual quantum dots-based fluorescence-linked immunosorbent assay for simultaneous detection on inflammation biomarkers," *Sensors and Actuators B: Chemical*, vol. 301, article 127118, 2019.

[37] A. A. Mansur, H. S. Mansur, A. J. Caires, R. L. Mansur, and L. C. Oliveira, "Composition-tunable optical properties of Zn_x $Cd_{(1-x)}$ S quantum dot–carboxymethylcellulose conjugates: towards one-pot green synthesis of multifunctional nanoplatforms for biomedical and environmental applications," *Nanoscale Research Letters*, vol. 12, no. 1, pp. 1–18, 2017.

[38] S. L. Sahoo, C.-H. Liu, M. Kumari, W.-C. Wu, and C.-C. Wang, "Biocompatible quantum dot-antibody conjugate for cell imaging, targeting and fluorometric immunoassay: crosslinking, characterization and applications," *RSC Advances*, vol. 9, no. 56, pp. 32791–32803, 2019.

[39] E. Song, M. Yu, Y. Wang et al., "Multi-color quantum dot-based fluorescence immunoassay array for simultaneous visual detection of multiple antibiotic residues in milk," *Biosensors and Bioelectronics*, vol. 72, pp. 320–325, 2015.

[40] C. Wang, R. Xiao, S. Wang et al., "Magnetic quantum dot based lateral flow assay biosensor for multiplex and sensitive detection of protein toxins in food samples," *Biosensors and Bioelectronics*, vol. 146, article 111754, 2019.

[41] S. Wang, J. J. Li, Y. Lv et al., "Synthesis of reabsorption-suppressed type-II/type-I ZnSe/CdS/ZnS core/shell quantum dots and their application for immunosorbent assay," *Nanoscale Research Letters*, vol. 12, no. 1, p. 380, 2017.

[42] Y. Wang, N. Gan, T. Li, Y. Cao, F. Hu, and Y. Chen, "A novel aptamer–quantum dot fluorescence probe for specific detection of antibiotic residues in milk," *Analytical Methods*, vol. 8, no. 15, pp. 3006–3013, 2016.

[43] Y. Lv, R. Wu, K. Feng et al., "Highly sensitive and accurate detection of C-reactive protein by CdSe/ZnS quantum dot-based fluorescence-linked immunosorbent assay," *Journal of Nanobiotechnology*, vol. 15, no. 1, p. 35, 2017.

[44] W. C. Chan and S. Nie, "Quantum dot bioconjugates for ultrasensitive nonisotopic detection," *Science*, vol. 281, no. 5385, pp. 2016–2018, 1998.

[45] H. C. Kim, H.-G. Hong, C. Yoon et al., "Fabrication of high quantum yield quantum dot/polymer films by enhancing dispersion of quantum dots using silica particles," *Journal of Colloid and Interface Science*, vol. 393, pp. 74–79, 2013.

[46] M. Gao, S. Kirstein, H. Möhwald et al., "Strongly photoluminescent CdTe nanocrystals by proper surface modification," *The Journal of Physical Chemistry B*, vol. 102, no. 43, pp. 8360–8363, 1998.

[47] J. Mao, J.-N. Yao, L.-N. Wang, and W.-S. Liu, "Easily prepared high-quantum-yield CdS quantum dots in water using hyperbranched polyethylenimine as modifier," *Journal of Colloid and Interface Science*, vol. 319, no. 1, pp. 353–356, 2008.

[48] G. Vastola, Y. W. Zhang, and V. B. Shenoy, "Experiments and modeling of alloying in self-assembled quantum dots," *Current Opinion in Solid State & Materials Science*, vol. 16, no. 2, pp. 64–70, 2012.

[49] Q. Ma, T.-Y. Song, P. Yuan, C. Wang, and X.-G. Su, "QDs-labeled microspheres for the adsorption of rabbit immunoglobulin G and fluoroimmunoassay," *Colloids and Surfaces B: Biointerfaces*, vol. 64, no. 2, pp. 248–254, 2008.

Research Article

Fluorescent Mitoxantrone Hydrochloride Nanoparticles Inhibit the Malignant Behavior of Giant Cell Tumor of Bone via miR-125b/PTH1R Axis

Baohui Su,[1] Yanguang Yuan,[2] Junshan Zhang,[1] Yuezhong Li,[1] and Qihui Zhang [3]

[1]*Department of Spinal Surgery, Weifang People's Hospital, Weifang, Shandong 261041, China*
[2]*Department of Orthopaedics, Anqiu People's Hospital, Weifang, Shandong 262100, China*
[3]*Department of Nursing, Anqiu People's Hospital, Weifang, Shandong 262100, China*

Correspondence should be addressed to Qihui Zhang; 2580332003@qq.com

Objective. To explore the therapeutic effects and mechanism of fluorescent mitoxantrone hydrochloride nanoparticles on giant cell tumor of bone. *Methods*. The adsorption capacity of nanoparticles to hydroxyapatite (HA), cell adsorption capacity, encapsulation rate, particle size, and potential of the nanoparticles were determined by HPLC and Zetasizer Nano ZS nanomicelle potentiometer. MTT assay was used to determine the toxicity of nanoparticles to cells. The fluorescent intensity of the nanoparticles and their location in the cells were observed under a fluorescence microscope. RT-qPCR and Western blotting were then used to measure the expression levels of miRNA, mRNA, and proteins in cells. Transwell and Annexin V-FITC/PI staining tests were used to study the cell invasion and apoptotic rate, respectively. The dual-luciferase reporter gene experiment was then carried out to verify the binding relationship between miR-125b and its predicted target. *Results*. ALN-FOL-MTO-NLC nanoparticles showed a stronger adsorption capacity for HA and stronger toxicity to GCTB28 cells. Compared to normal tissues, the expression level of miR-125b in giant bone tumor tissue and cells was significantly downregulated, and the expression level of miR-125b was upregulated to some extent after treatment. Overexpression of miR-125b or treatment of ALN-FOL-MTO-NLC nanoparticles can inhibit the malignant behavior of GCTB28 cells, whereas the inhibition of the expression of miR-125b can promote the malignant behavior of GCTB28 cells. The result showed that parathyroid hormone receptor 1 (PTH1R) was a downstream target gene for miR-125b. Rescue experiment showed that the treatment of GCTB28 with ALN-FOL-MTO-NLC nanoparticles while inhibiting miR-125b expression can reduce the inhibitory effect of miR-125b on the malignant behavior of GCTB28 cells, whereas upregulating the expression levels of miR-125b and PTH1R in GCTB28 cells had no significant effect on the malignant behavior of GCTB28 cells. *Conclusion*. ALN-FOL-MTO-NLC nanoparticles have a certain inhibitory effect on the malignant behavior of giant cell tumor of bone through the miR-125b/PTH1R molecular axis.

1. Introduction

Giant cell tumor of bone (GCT) is a bone tumor with high invasiveness and osteolytic nature [1] with potential malignancy [2]. GCT is mainly composed of three kinds of cells, including bone cell-like multinucleated giant cells, spindle-like stromal cells, and monocytes [3]. At present, the preferred treatment for GCT is local treatment with assisted surgery, but this treatment has a higher postoperative recurrence rate [4]; therefore, it is important to find a new way for GCT treatment.

Considering the structural characteristics of human tissues, nanoparticles have good advantages in size, can interact with the biological components of the human body, and regulate various biological behaviors of the human body [5]. Nanomaterial-based drug delivery systems are smaller in size, giving them quantum size effects, interfacial effects, and macrochain tunneling effects. Therefore, the nanodrug showed strong permeability, greater solubility, better adsorption, and so on in biology. Due to the small size and large surface area of nanoparticles, nanodrugs are easy to pass

through blood vessels in vivo and are not easy to cause damage to the inner wall of blood vessels. In addition, the nanoparticles have the advantages of high surface activity, many active centers, and good catalytic efficiency, so nanodrugs can be prepared into sustained-release drugs, change the half-life of drugs in vivo, and extend the action time of drugs. Based on the above advantages, the drug delivery system based on nanomaterials can have better targeting, so that the nanodrug-carrying system can pass through the biological barrier and reach the lesion area [6]. Not surprisingly, a large number of studies have shown that drug delivery systems based on nanomaterials can be used to treat a variety of orthopedic diseases that are difficult to treat with conventional clinical therapies, such as arthritis, osteoporosis, bone cancer, and related bone diseases [7–11]. Although nanoparticles have certain advantages in the treatment of bone diseases, there are still several problems, such as the low drug loading of bone-targeted macromolecular carriers and its easy excretion through the kidney.

Mitoxantrone hydrochloride (Mitoxantro, MTO) is usually used as an anticancer drug in cancer treatment. Shi et al. took MTO as a model drug and developed a new kind of nanodrug-carrying system, and the results of in vivo and in vitro experiments confirmed that the nanodrug-carrying system has a good long-circulation effect and an increased ability to target bone tissue [12]. However, the above research only discussed the theoretical advantages of the new nanodrug-loading system and does not study whether the nanodrug-loading system can improve the therapeutic effect on bone tumors.

MicroRNA (miRNA, miR) is a group of endogenous noncoding RNAs with a length of 20 to 25 nucleotides. It can negatively regulate the expression of mRNA by inhibiting the translation of mRNA or reducing the stability of mRNA [13]. Studies have shown that miRNA can play an important role in many biological processes. Parathyroid hormone-related protein (PTHrP) plays a pivotal role in the development of bones [14], and its expression in various cancer tissues and cells is also significantly upregulated [15]. PTH1R as a PTHrP receptor is also positively expressed in various cancers and cells [16]. In the previous research, PTH1R was found to be the target gene of miR-125b through the prediction of biological gene database. Therefore, in this article, we will discuss the treatment effects of GCT with the nanodrug-loaded particles at the cellular level and verify the mechanism of action of miR-125b/PTH1R in GCT.

2. Materials and Methods

2.1. Experimental Materials

2.1.1. Tissues and Cells. Bone giant cell tumor tissues and corresponding paracancerous tissues were collected from patients who were diagnosed and operated in our hospital from October 2010 to October 2019. This study was approved by the ethics committee of our hospital. Both patients and their families knew the purpose and significance of this study and signed the informed consent. MG-63 cells

and hFOB1.9 cells were purchased from Tongpai (Shanghai) Biotechnology Co., Ltd. GCTB28 cells were purchased from China Center for Type Culture Collection.

2.1.2. Experimental Reagents. Phospholipid, glyceryl trilaurate, cholesterol, mitoxantrone hydrochloride, sodium lauryl sulfate, methanol, methylene chloride, FOL-S100, ALN-S100, hydroxyphosphorus lime, coumarin-6, dimethyl sulfoxide, and polyoxyethylene castor oil were all purchased from Shanghai Houcheng Fine Chemical Co., Ltd. RPMI 1640 medium, Annexin V-FITC/PI kit, and QuikChange site-directed mutation kit were purchased from Shanghai Kemin Biotechnology Co., Ltd. The BCA kit and TRIZOL kit were purchased from Beijing Kairuiji Biotechnology Co., Ltd. The MTT test kit was purchased from Shanghai Yiyan Biotechnology Co., Ltd. The RT kit (reverse transcription kit) was purchased from Shanghai Zeye Biotechnology Co., Ltd. RIPA lysate was purchased from Shanghai Yuanye Biotechnology Co., Ltd., and the dual-luciferase reporter gene kit was purchased from Beijing Baierdi Biotechnology Co., Ltd.

2.2. Preparation of Mitoxantrone Hydrochloride Nanoparticles. 250 mg of a phospholipid, 25 mg of glyceryl trilaurate, 25 mg of cholesterol, 10 mg of mitoxantrone hydrochloride, and 10 mg of sodium lauryl sulfate were weighed and added to a 250 mL eggplant-shaped bottle, and 10 mL of methanol-dichloromethane (volume ratio 1 : 1) mixture was then added. The solution was then distilled at 37°C under reduced pressure and vacuum dried overnight. After that, 10 mL of 2% polyoxyethylene castor oil aqueous solution was added and hydrated at 37°C for 30 min. It was then immersed in an ice bath (200 W) for 300 times and squeezed through a 0.22 μm filter to obtain toxantrone hydrochloride nanoparticles (MTO-NLCs).

To obtain the ALN-FOL-MTO-NLCs, 20 mg of folic acid-polyoxyethylene monostearate (FOL-S100) and 100 mg of alenic acid-polyoxyethylene monostearate (ALN-S100) were added to the eggplant-shaped flask before distillation under reduced pressure. The subsequent steps were the same as above, and the double-ligand modified nanoparticles (ALN-FOL-MTO-NLCs) were then obtained.

2.3. Measurement of Nanoparticle Encapsulation Rate, Particle Size, and Potential. 0.1 mL of nanoparticle was added with 0.4 mL of distilled water for dilution, which was then centrifuged at 8000 runs/min for 5 min. The encapsulation rate was then calculated based on the drug content in supernatant and nanoparticle determined by HPLC. 0.1 mL of nanoparticle preparation was added in 3.9 mL of distilled water for dilution. Particle size and potential of nanoparticles were then determined with the Zetasizer Nano ZS nanomicelle potentiometer.

2.4. Identification of HA Adsorption Capacity of Nanoparticles. The nanoparticles were diluted with distilled water to make the drug content reach 0.1 mg/mL. Two grams of hydroxyapatite (hydroxylapatite, HA) was then weighed and added into 50 mL of the diluted nanoparticle preparation and stirred at room temperature for 60 min, which was then sampled every 15 minutes. After filtering the sample through

a 0.45 μm filter membrane, the drug content in the unabsorbed nanoparticles and the diluted nanoparticle preparation in the filtrate were determined by HPLC, and the adsorption ratio of the nanoparticles was then calculated.

2.5. Cellular Adsorption Capacity of Nanoparticles. Instead of mitoxantrone hydrochloride and sodium lauryl sulfate, coumarin-6 (C6) was used to prepare the C6-coated nanoparticles according to the method in Section 2.2. GCTB28 cells in the logarithmic growth phase were seeded in 96-well plates at a density of 1×10^5 per well and incubated at 37°C for 24 h. After discarding the culture solution, the nanoparticle preparation diluted with RPMI 16140 medium without folic acid was added, the cells were then incubated at different temperatures for 4 h and washed 3 times with PBS after the incubation. After lysing the cells, the BCA kit and HPLC were then used to determine the concentration of protein and C6 in the sample. The uptake index was calculated according to the formula: uptake (%) = intracellular C6 concentration/intracellular protein concentration × 100.

2.6. Determination of Cytotoxicity of Nanoparticles. GCTB28 cells in the logarithmic growth phase were seeded in 96-well plates at a density of 5×10^3 per well. MTO-NLCs and ALN-FOL-MTO-NLCs were diluted with folic acid-free PRMI 1640 medium and added to each well, and the cells were then incubated for 48 h. After that, each well was rinsed 3 times with 37°C HBSS, and 20 μL of MTT solution was then added to each well. After incubation for another 4 h, 150 μL of DMSO was then added. A microplate reader was then used to measure the absorbance of each well at 570 nm after the solution was thoroughly mixed.

2.7. Cell Transfection. Cells in the logarithmic growth phase were taken and prepared into a cell suspension, seeded in 96-well plates at a density of 1×10^5 per well, and cultured at 37°C for 24 h. The Liposome 2000 kit instructions were then strictly followed for cell transfection, and the transfection efficiency was determined with the RT-qPCR experiment.

2.8. RT-qPCR. The total RNA in the cells was extracted with the TRIzol kit, and then reverse transcription was performed using the reverse transcription kit according to the reaction system shown in Table 1. The expression levels of miRNA and mRNA in cells were quantitatively measured based on the reaction system shown in Table 2. The U6 and GAPDH were used as internal references for miRNA and mRNA, respectively. The setting for PCR was as follows: 40 total cycles, 95°C for 10 min, 95°C for 30 s, 58°C for 30 s, 72°C for 10 s, and 72°C for 10 min.

2.9. MTT Experiment. Cells in the logarithmic growth phase of each group were pipetted into single cells in a serum-free medium for suspension culture. Cells were then seeded in 96-well plates at a density of 5×10^3 cells per well. After different treatments, 20 μL of MTT solution dissolved in PBS was added. After incubating at 37°C for 4 h, the culture medium in each well was discarded, and 150 μL of DMSO

TABLE 1: Reverse transcription reaction system.

Material	Volume (μL)
RNA	2
oligoDT	1
Random primers	1
5X buffer	4
Mix	1
Deionized water	12

TABLE 2: PCR reaction system.

Material	Volume (μL)
SYBR Green Mix	9
cDNA	2
Primer	1
Deionized water	8

was added and thoroughly mixed. The absorbance of each well at 570 nm was then measured with a microplate reader.

2.10. Transwell Experiment. Cells in the logarithmic growth phase were seeded on the upper layer of the Transwell chamber coated with Matrigel gel, and the conventional medium was added to the lower layer of the Transwell chamber. After 24 h, the cells were fixed with a mixture of acetic acid and formaldehyde for 15 min, which was then rinsed three times with the PBS buffer. The cells that did not pass through the chamber were then gently wiped out with a cotton swab. Cells that passed through the chamber were then stained with crystal violet and washed three times with PBS buffer. To determine the cell invasiveness, the stained cells were then put under a microscope, and a number of field views were randomly selected to take pictures.

2.11. Western Blotting. Cells were lysed with RIPA lysate, and the proteins in the cells were separated using 10% SDS-PAGE, which was then transferred to PVDF membranes. The PVDF membranes were then blocked and subsequently incubated with primary antibody (PTH1R, 1:1000) at 4°C overnight. After washing with PBS, the PVDF membranes were incubated with secondary antibody (1:5000) for 1 h at room temperature. Using GAPDH as an internal parameter, ImageJ was then used to determine the gray value of the band.

2.12. Annexin V-FITC/PI Double-Staining Experiment. After treating the cells of each group according to the experimental design, the cell culture was centrifuged at 3000 runs/min for 5 min, and the supernatant was discarded. The pellet was then rinsed with PBS for 3 times. The collected cells were then seeded in a 96-well plate at a density of 1×10^5 per well and incubated for 12 h. The Annexin V-FITC/PI double-staining experiment was then carried out according to the instructions of Annexin V-FITC/PI Apoptosis Detection Kit. The apoptotic rates of each group of cells were then measured with flow cytometry.

(a)

(b)
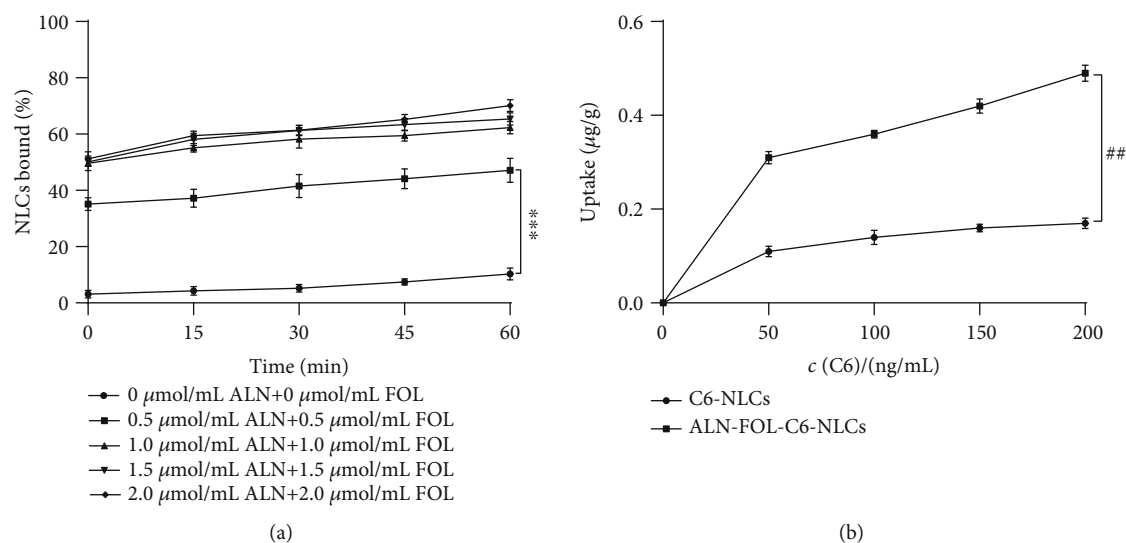
FIGURE 1: Preparation and identification of nanoparticles. (a) The binding ability of MTO-loaded NLCs to HA. (b) Cell uptake of C6-NLCs and ALN-FOL-C6-NLCs ($\bar{x} \pm s$, $n = 3$). $***P < 0.001$ compared with the 0 μmol/L ALN + 0 μmol/L FOL group; $^{\#\#}P < 0.01$ compared with the C6-NLCs group.

2.13. Dual-Luciferase Reporter Gene Experiment. The PTH1R 3′-UTR fragment was amplified and cloned into a vector to construct wild-type PTH1R (PTH1R-wt). And the mutant PTH1R (PTH1R-mut) was constructed using the Quik-Change site-directed mutation kit. The liposome transfection kit was then used to transfect miR-NC or miR-125b mimics and PTH1R-wt or PTH1R-mut into GCTB28 cells. After incubation for 48 h, the luciferase activity was determined using the dual-luciferase reporter gene system.

2.14. Localization of Drugs in Cells via Immunofluorescence Microscopy. GCTB28 cells in the logarithmic growth phase were inoculated in a special laser confocal Petri dish. After 24 h of incubation, ALN-FOL-MTO-NLC nanoparticles were added and further incubated for another 1 h. After that, the medium was removed, and the cells were rinsed with PBS twice. An immunofluorescence microscope was then used to detect the fluorescence intensity and localization of ALN-FOL-MTO-NLCs in the cells.

2.15. Statistical Analysis. GraphPad Prism 8.0 was used for drawing and statistical analysis. The *t*-test was used for the comparison between two groups, and the single-factor analysis of variance was used for the comparison between multiple groups. $P < 0.05$ was used to indicate that the difference is statistically significant.

3. Results

3.1. Preparation and Identification of Mitoxantrone Hydrochloride Nanoparticles. Microscopic examination results showed that MTO-NLCs and ALN-FOL-MTO-NLCs were spherical and regular in shape. The test results showed that the encapsulation rate, particle size, and potential of MTO-NLCs were $99.37 \pm 0.26\%$, 50.62 ± 3.34 nm, and -3.42 ± 1.13 mV, respectively; the encapsulation rate, par-

ticle size, and potential of ALN-FOL-MTO-NLCs were $99.87 \pm 0.17\%$, 46.18 ± 2.53 nm, and -17.11 ± 2.24 mV, respectively. The HA adsorption test showed that compared with MTO-NLCs, the adsorption capacity of ALN-FOL-MTO-NLCs on HA was significantly enhanced, and with the increase of the modification of ALN-S100 and FOL-S100, the adsorption capacity of nanoparticles on HA also increased ($P < 0.001$), as shown in Figure 1(a). The results of cell uptake experiments showed that compared with C6-NLCs, the uptake of ALC-FOL-C6-NLCs by GCTB28 cells was higher ($P < 0.01$), as shown in Figure 1(b).

3.2. The Effects of Mitoxantrone Hydrochloride Nanoparticles on GCTB28 Cells. The cytotoxicity test results showed that ALN-FOL-MTO-NLCs in GCTB28 cells showed stronger cytotoxicity ($P < 0.05$) than MTO-NLCs, as shown in Figure 2(a). After the treatment of GCTB28 cells with ALN-FOR-MTO-NLC nanoparticles, the red fluorescence of the drug can be observed and mainly distributed in the cytoplasm, as shown in Figure 2(b). Based on the above results, we believe that ALN-FOL-MTO-NLCs have a better inhibitory effect on the malignant behavior of GCTB28 cells.

The results of RT-qPCR experiments showed that the expression of miR-125b in MG-63 cells and GCTB28 cells was significantly downregulated ($P < 0.05$), consistent with the results of Fei et al. [17]. And the expression level of miR-125b in hFOB1.19 cells was 4.82 times than that of GCTB28 cells, as shown in Figure 2(c). The expression of miR-125b in normal tissues was 5.16 times higher than that of cancer tissues, as shown in Figure 2(d). After GCTB28 cells were treated with nanoparticles, the expression levels of miR-125b in the MTO-NLCs group and ALN-FOL-MTO-NLCs group were 3.67 and 4.89 times higher than that of the control group, respectively, as shown in Figure 2(e), which is consistent with our predictions; therefore, ALN-FOL-MTO-NLCs were selected for the subsequent experiments.

(a)

DAPI   ALN-FOL-MTO-NLCs   Merge

(b)

(c)

(d)

(e)

(f)

FIGURE 2: Continued.

(g)

(h)

(i)
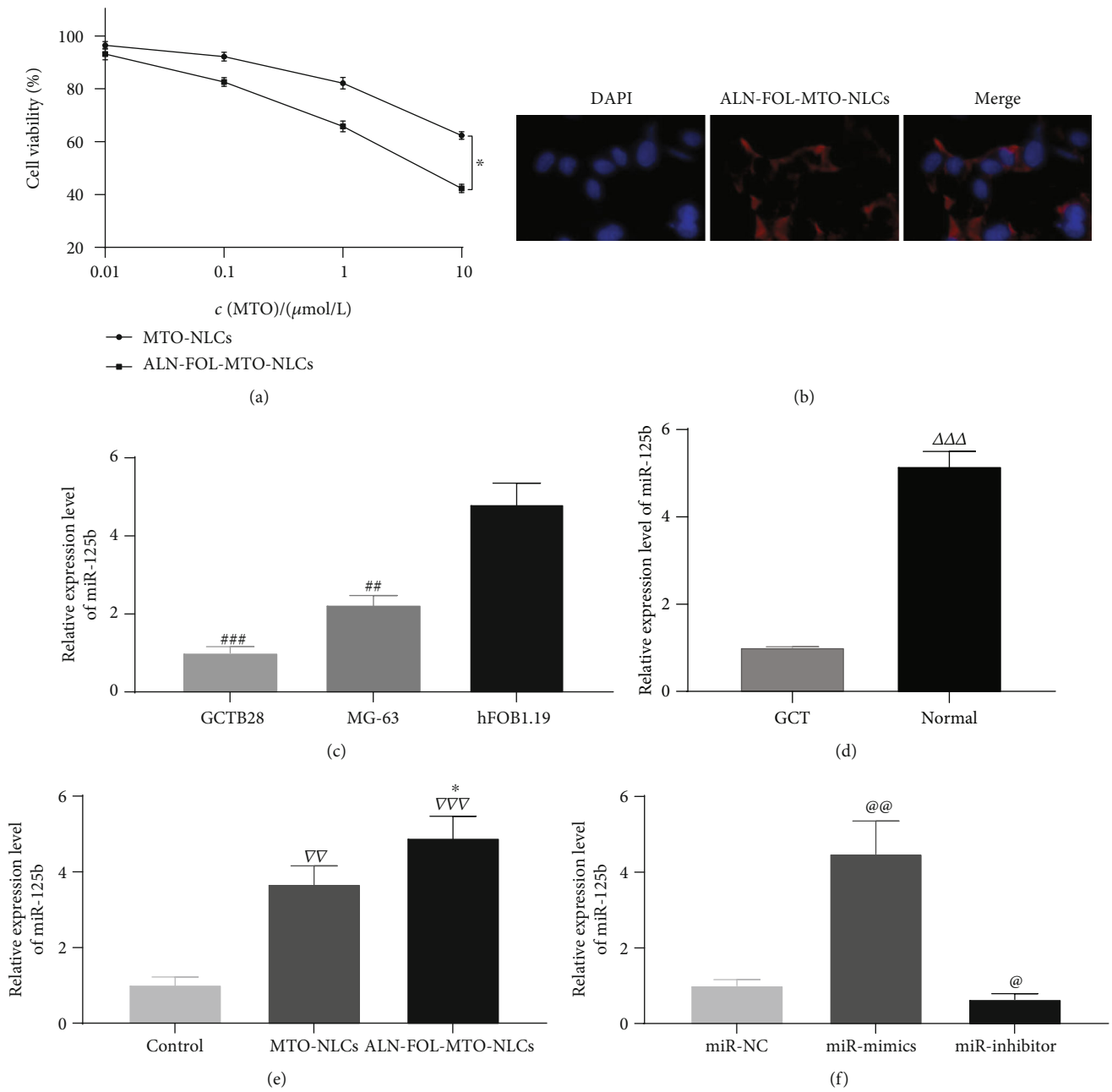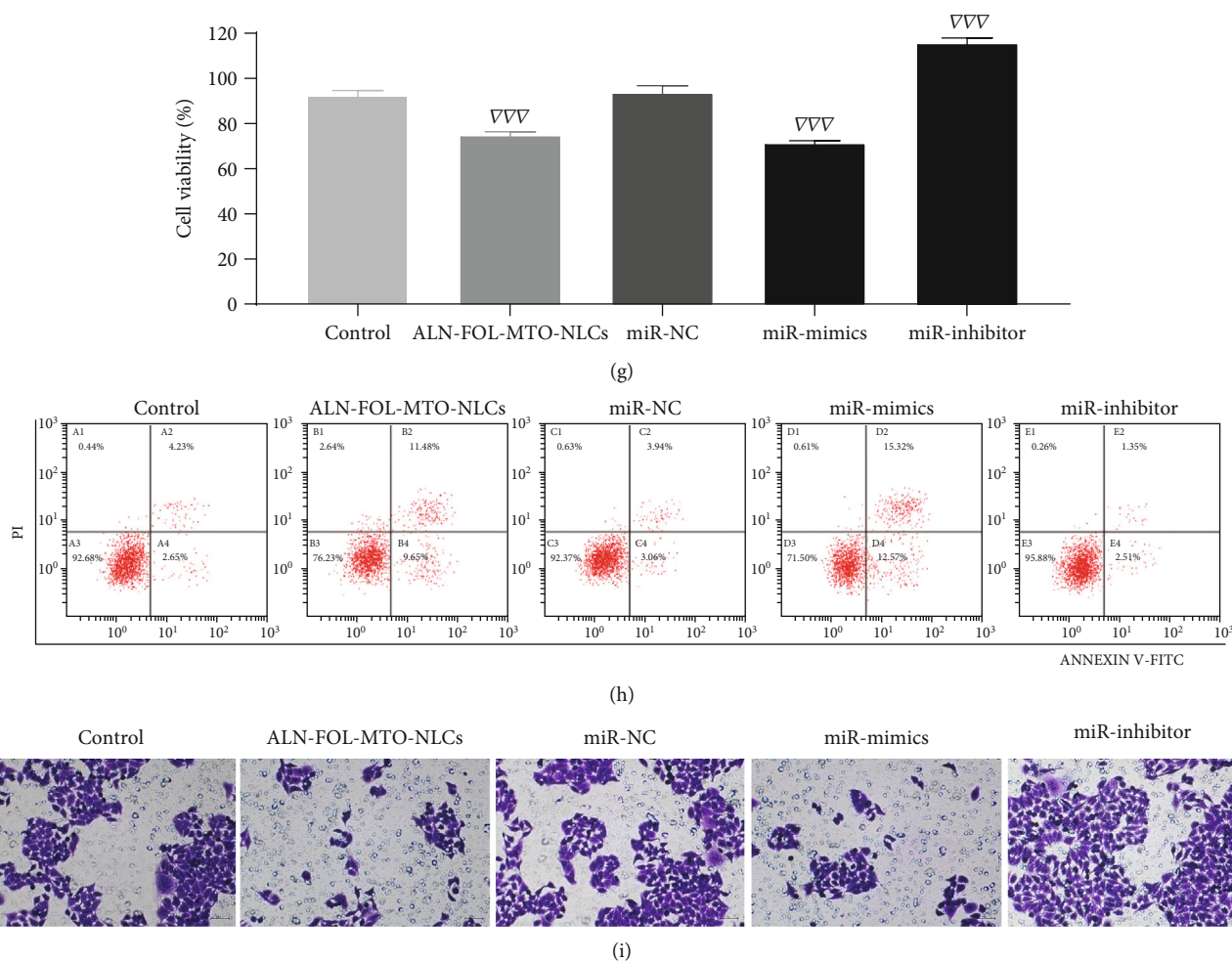
FIGURE 2: Effects of MTO-NLCs and ATL-FOL-MTO-NLCs on GCTB28 cells. (a) In vitro cytotoxicity test of MTO-NLCs and ALN-FOL-MTO-NLCs with different concentrations. (b) Drug localization in the GCTB28 cell. (c–f) Relative expression level of miR-125b. (g) GCTB28 cell proliferation activity. (h) GCTB28 cell apoptosis rate. (i) GCTB28 cell invasion number. ($\bar{x} \pm s$, $n = 3$). $*P < 0.05$ compared with the MTO-NLCs group. $^{\#\#}P < 0.01$ and $^{\#\#\#}P < 0.001$ compared with the hFOB1.9 cell group; $^{\triangle\triangle\triangle}P < 0.001$ compared with the GCT tissue group; $^{@}P < 0.05$ and $^{@@}P < 0.01$ compared with the miR-NC group; $^{\triangledown\triangledown}P < 0.01$ and $^{\triangledown\triangledown\triangledown}P < 0.01$ compared with the control group.

After transfection with miR-NC, miR-125b mimics, and miR-125b inhibitor, RT-qPCR was used to detect the transfection efficiency, and the results are shown in Figure 2(d). Furthermore, the MTT test showed that the proliferation capabilities of GCTB28 cells transfected with miR-NC liposomes were not significantly different from that of the control group, whereas the proliferation capabilities of GCTB28 cells after transfection with miR-125b mimics and ALN-FOL-MTO-NLCs was significantly reduced compared with the control group ($P < 0.05$), and the proliferation capabilities of GCTB28 transfected with miR-125b inhibitor liposomes was significantly increased compared with the control group ($P < 0.05$), as shown in Figure 2(g). Annexin V/PI double-staining results showed that the apoptotic rates of GCTB28 cells transfected with miR-NC liposomes were not significantly different from that of the control group. GCTB28 cells transfected with miR-125b mimics and ALN-FOL-MTO-NLCs had higher apoptotic rates compared with the control group ($P < 0.05$), and the apoptotic rates of GCTB28 cells transfected with miR-125b inhibitor liposome were signifi-

cantly reduced compared with the control group ($P < 0.05$) as shown in Figure 2(h) and Figure S1. The Transwell experiments showed that the number of migratory GCTB28 cells transfected with miR-NC liposomes was not significantly different from that of the control group, whereas GCTB28 cells transfected with miR-125b mimics and GCTB28 cells treated with ALN-FOL-MTO-NLCs had a significantly lower migration rate compared with the control group ($P < 0.05$). Furthermore, the number of migratory GCTB28 cells transfected with miR-125b inhibitor liposomes was significantly higher than that of the control group ($P < 0.05$), as shown in Figure 2(i) and Figure S2.

3.3. The Targeting Relationship between miR-125b and PTH1R. The bioinformatic analysis showed that parathyroid hormone receptor 1 (PTH1R) is the target gene of miR-125b, and the binding sequence is shown in Figure 3(a). The results of the dual-luciferase reporter gene experiment showed that overexpression of miR-125b induced a decrease in the luciferase activity of PTH1R-wt ($P < 0.05$); however,

miR-125b: AGUGUUCAAUCCCAGAGUCCCU

PTH1R: UGAAUGAUUUCCCACUCAGGGC

(a)

(b)

PTH1R

GAPDH

(c)

(d)
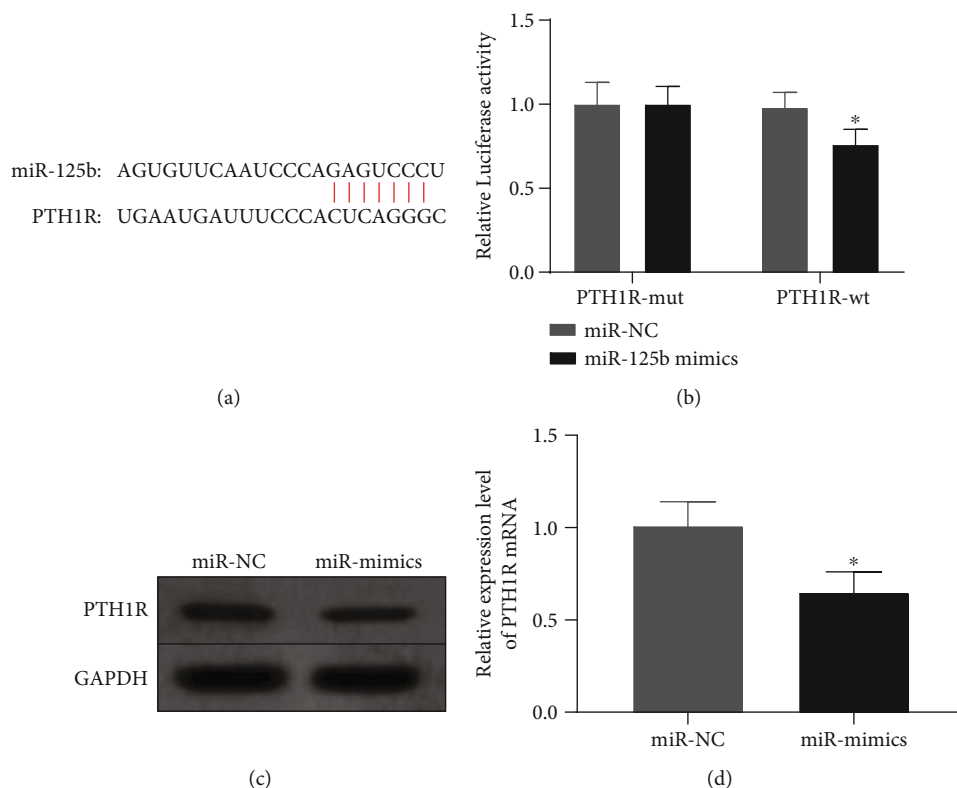
FIGURE 3: Targeting relationship between miR-125b and PTH1R. (a) miR-125b and PTH1R-binding sequence. (b) Results of dual-luciferase reporter experiments. (c) Expression of PTH1R protein in GCTB28 cells. (d) The relative expression level of PTH1R in GCTB28 cells. ($\bar{x} \pm s$, $n = 3$). ∗$P < 0.05$ compared with the miR-NC group.

it had no significant effect on the luciferase activity of PTH1R-mut, as shown in Figure 3(b). Thus, the above dual-luciferase reporter gene experiment verified the targeting relationship between PTH1R and miR-125b. Western blotting experiments and RT-PCR results also showed that overexpression of miR-125b significantly inhibited the expression of PTH1R protein and mRNA ($P < 0.05$), as shown in Figures 3(c) and 3(d).

3.4. ALN-FOL-MTO-NLCs Inhibit the Malignant Behavior of GCTB28 Cells through the miR-125b/PTH1R Molecular Axis.

RT-qPCR results showed that the expression of PTH1R mRNA in GCTB28 cells was significantly increased after transfection with pc-PTH1R ($P < 0.05$), and the expression of PTH1R mRNA in GCTB28 cells was significantly decreased after transfection with si-PTH1R ($P < 0.05$), as shown in Figure 4(a). MTT results showed that compared with the control group, the proliferation activity of GCTB28 cells in the si-PTH1R group and ALN-FOL-MTO-NLCs group was significantly reduced ($P < 0.05$), whereas the proliferation activities of GCTB28 cells in the miR-inhibitor + ALN-FOL-MTO-NLCs group and miR-mimics + pc-PTH1R group did not show significant changes, as shown in Figure 4(b). The Annexin V/PI double-staining results showed that compared with the control group, the apoptotic rates of GCTB28 cells in the si-PTH1R group and the ALN-FOL-MTO-NLCs group increased significantly ($P < 0.05$), whereas there was no significant change in the apoptotic

rates of GCTB28 cells in the miR-inhibitor + ALN-FOL-MTO-NLCs group and miR-mimics + pc-PTH1R group, as shown in Figure 4(c) and Figure S3. Transwell experiment showed that compared with the control group, the number of invasive GCTB28 cell in the si-PTH1R group and the ALN-FOL-MTO-NLCs group was significantly reduced ($P < 0.05$), whereas the number of invasive GCTB28 cells in the miR-inhibitor + ALN-FOL-MTO-NLCs group and miR-mimics + pc-PTH1R group did not change significantly from the control group, as shown in Figure 4(d) and Figure S4.

4. Discussion

As one of the most common primary bone tumors, GCT is frequently occurred in young people and often happens around the knee joint. Although the malignant degree of GCT is low, it still has strong invasiveness and osteolysis, and the recurrence rate after surgical treatment is extremely high, which seriously affects the quality of patients' life. Therefore, finding new treatment strategies is essential to improve the quality of life for patients and reduce their recurrence rates after surgery. Studies have shown that nanoparticles have unparalleled advantages in the treatment of bone tumors. In this study, based on the research of Shi et al., MTO-NLC and ALN-FOL-MTO-NLC nanoparticles were prepared. Careful examination of the prepared nanoparticles revealed that both nanoparticles were spherical and regular

(a)

(b)

(c)

(d)
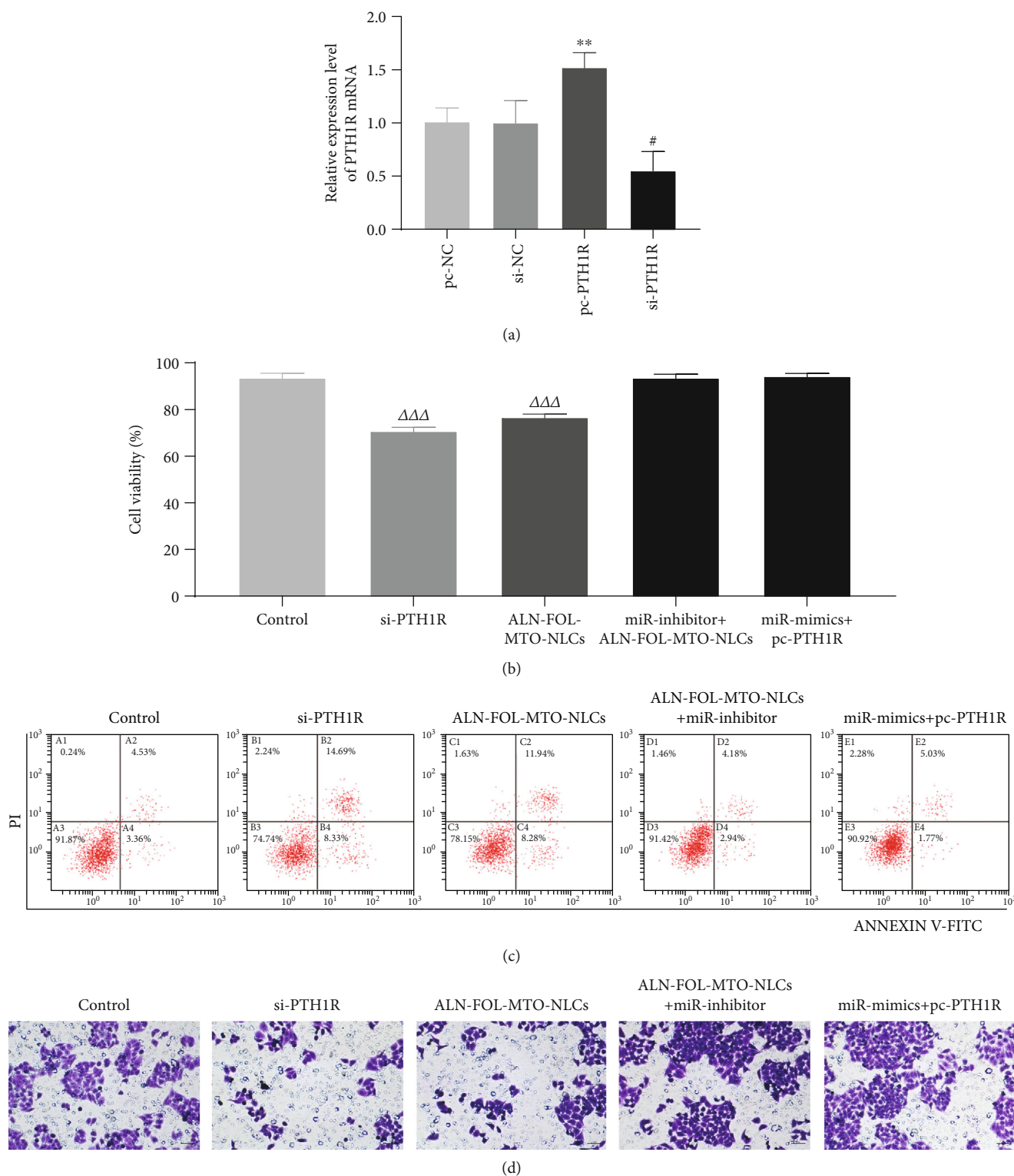
Figure 4: Reply experiment. (a) The relative expression level of PTH1R mRNA. (b) GCTB28 cell proliferation activity. (c) GCTB28 cell apoptosis rate. (d) GCTB28 cell invasion number. ($\bar{x} \pm s$, $n = 3$). $**P < 0.01$ compared with the pc-NC group; $^\#P < 0.05$ compared with the si-NC group; $^{\triangle\triangle\triangle}P < 0.001$ compared with the control group.

in shape, and the rate of drug coverage, particle size, and potential was consistent with the results of Shi et al. Furthermore, compared with MTO-NLCs, ALN-FOL-MTO-NLCs have a certain degree of improvement in terms of HA adsorption capacity, cellular uptake capacity, and toxicity to cancer cells. This improvement is partially attributed to ALN. As a

bone metabolism regulator, ALN has a strong affinity with HA. Therefore, the modifications of nanoparticles with FOL not only ensured the steric hindrance of PEG but also increased the ingestion of nanoparticles by target cells. Immunofluorescence microscopy results showed that the ALN-FOR-MTO-NLC nanoparticles in GCTB28 cells were red fluorescent and mainly distributed in the cytoplasm, which is also consistent with the results of Vibet et al. [18].

Specifically, various studies have confirmed the expression changes of miR-125b in a variety of cancer tissues and cells. For example, miR-125b as a tumor suppressor gene was downregulated in breast cancer tissues and cells [19], and miR-125b expression in gastric cancer tissues and cells was also significantly downregulated [20]. In this study, it was found that the expression level of miR-125b in GCT tissues and cells was also significantly downregulated. The expression of miR-125b in GCT cells was upregulated to varying degrees after treatment with MTO-NLCs and ALN-FOL-MTO-NLCs, and the overexpression of miR-125b produced certain effects on proliferation, invasion, and apoptosis of GCT cells. Therefore, we think miR-125b played a role in the occurrence and development of GCT, which may be related to the role of ALN-FOL-MTO-NLC nanoparticles.

In this study, inhibiting the expression of PTH1R in GCTB28 cells reduced the proliferation and invasion of GCTB28 cells and induced its apoptosis. Moreover, bioinformatics analysis showed that PTH1R and miR-125b have partially complementary sequences, and their targeting relationship was further verified via the dual-luciferase reporter gene experiment, Western blotting, and RT-qPCR.

At the end of the study, through a series of rescue experiments, it was confirmed that ALN-FOL-MTO-NLCs inhibited the malignant behavior of GCTB28 cells by upregulating the expression level of miR-125b which then inhibited the expression of PTH1R. This result provides a theoretical basis for clarifying the mechanism of ALN-FOL-MTO-NLCs in the treatment of GCT, and ALN-FOL-MTO-NLCs combined with surgery may become a new strategy for the treatment of GCT.

Data Availability

All the data is available with the handwritten notebook documented in our lab.

Conflicts of Interest

The authors declare that there are no conflicts of interest regarding the publication of this paper.

Acknowledgments

Supplementary Materials

Figure S1: GCTB28 cell apoptosis rate. Figure S2: GCTB28 cell invasion number. Figure S3: GCTB28 cell apoptosis rate. Figure S4: GCTB28 cell invasion number ($\bar{x} \pm s$, $n = 3$); $*P < 0.05$, $**P < 0.01$, and $***P < 0.001$, compared with the control group. (Supplementary Materials)

References

[1] B.-J. Noh and Y.-K. Park, "Giant cell tumor of bone: updated molecular pathogenesis and tumor biology," *Human Pathology*, vol. 81, pp. 1–8, 2018.

[2] E. Palmerini, P. Picci, P. Reichardt, and G. Downey, "Malignancy in giant cell tumor of bone: a review of the literature," *Technology in Cancer Research & Treatment*, vol. 18, article 1533033819840000, 2019.

[3] J. Lüke, M. Hasenfratz, P. Möller, and T. F. E. Barth, "New aspects on giant cell tumor of bone," *Der Pathologe*, vol. 39, no. 2, pp. 125–131, 2018.

[4] H. Cheng, A. Chawla, Y. Yang et al., "Development of nanomaterials for bone-targeted drug delivery," *Drug Discovery Today*, vol. 22, no. 9, pp. 1336–1350, 2017.

[5] S. Aftab, A. Shah, A. Nadhman et al., "Nanomedicine: an effective tool in cancer therapy," *International Journal of Pharmaceutics*, vol. 540, no. 1-2, pp. 132–149, 2018.

[6] B. Bahrami, M. Hojjat-Farsangi, H. Mohammadi et al., "Nanoparticles and targeted drug delivery in cancer therapy," *Immunology Letters*, vol. 190, pp. 64–83, 2017.

[7] S. Qadri, Y. Haik, E. Mensah-Brown, G. Bashir, M. J. Fernandez-Cabezudo, and B. K. al-Ramadi, "Metallic nanoparticles to eradicate bacterial bone infection," *Nanomedicine*, vol. 13, no. 7, pp. 2241–2250, 2017.

[8] I. Takeuchi, S. Kobayashi, Y. Hida, and K. Makino, "Estradiol-loaded PLGA nanoparticles for improving low bone mineral density of cancellous bone caused by osteoporosis: application of enhanced charged nanoparticles with iontophoresis," *Colloids and Surfaces B: Biointerfaces*, vol. 155, pp. 35–40, 2017.

[9] S. Huang, X. Song, T. Li et al., "Pellet coculture of osteoarthritic chondrocytes and infrapatellar fat pad-derived mesenchymal stem cells with chitosan/hyaluronic acid nanoparticles promotes chondrogenic differentiation," *Stem Cell Research & Therapy*, vol. 8, no. 1, p. 264, 2017.

[10] S. Jie, X. Guo, and Z. Ouyang, "Tumor ablation using novel photothermal Nax WO3 nanoparticles against breast cancer osteolytic bone metastasis," *International Journal of Nanomedicine*, vol. 14, pp. 7353–7362, 2019.

[11] J. Liu, Y. Zeng, S. Shi et al., "Design of polyaspartic acid peptide-poly(ethylene glycol)-poly(epsilon-caprolactone) nanoparticles as a carrier of hydrophobic drugs targeting cancer metastasized to bone," *International Journal of Nanomedicine*, vol. 12, pp. 3561–3575, 2017.

[12] Y. Shi, Z. Su, S. Li et al., "Multistep targeted nano drug delivery system aiming at leukemic stem cells and minimal residual disease," *Molecular Pharmaceutics*, vol. 10, no. 6, pp. 2479–2489, 2012.

[13] M. Pu, J. Chen, Z. Tao et al., "Regulatory network of miRNA on its target: coordination between transcriptional and post-transcriptional regulation of gene expression," *Cellular and Molecular Life Sciences*, vol. 76, no. 3, pp. 441–451, 2019.

[14] S. Nishimori, F. Lai, M. Shiraishi et al., "PTHrP targets HDAC4 and HDAC5 to repress chondrocyte hypertrophy," *JCI Insight*, vol. 4, no. 5, 2019.

[15] R. Zhang, J. Li, G. Assaker et al., "Parathyroid hormone-related protein (PTHrP): an emerging target in cancer progression and metastasis," *Advances in Experimental Medicine and Biology*, vol. 1164, pp. 161–178, 2019.

[16] R. W. Cowan, G. Singh, and M. Ghert, "PTHrP increases RANKL expression by stromal cells from giant cell tumor of bone," *Journal of Orthopaedic Research*, vol. 30, no. 6, pp. 877–884, 2012.

[17] F. Wang, D. Yu, Z. Liu et al., "MiR-125b functions as a tumor suppressor and enhances chemosensitivity to cisplatin in osteosarcoma," *Technology in Cancer Research & Treatment*, vol. 15, no. 6, pp. NP105–NP112, 2016.

[18] S. Vibet, K. Mahéo, J. Goré, P. Dubois, P. Bougnoux, and I. Chourpa, "Differential subcellular distribution of mitoxantrone in relation to chemosensitization in two human breast cancer cell lines," *Drug Metabolism and Disposition: The Biological Fate of Chemicals*, vol. 35, no. 5, pp. 822–828, 2007.

[19] G. Hu, X. Zhao, J. Wang et al., "miR-125b regulates the drug-resistance of breast cancer cells to doxorubicin by targeting HAX-1," *Oncology Letters*, vol. 15, no. 2, pp. 1621–1629, 2018.

[20] X. Zhang, J. Yao, K. Guo et al., "The functional mechanism of miR-125b in gastric cancer and its effect on the chemosensitivity of cisplatin," *Oncotarget*, vol. 9, no. 2, pp. 2105–2119, 2018.

Research Article

Chemosensing Test Paper Based on Aggregated Nanoparticles of a Barbituric Acid Derivative

Jinzhen Xu,[1] Hanjun Zhang,[1] Zhen Xu,[1] Furong Tao,[1] Yuezhi Cui ⓘ,[1] and William W. Yu ⓘ[2]

[1]*School of Chemical and Pharmaceutical Engineering, Qilu University of Technology (Shandong Academy of Sciences), Jinan 250353, China*
[2]*Louisiana State University, Shreveport, Louisiana 71115, USA*

Correspondence should be addressed to Yuezhi Cui; yuezhicui@163.com and William W. Yu; wyu6000@gmail.com

The development of sensitive, cheap, and portable methods for detecting nitroaromatics explosives has a profound significance and value for public health and environmental protection. For this purpose, a new D-π-A barbituric acid derivative CB-CYH with aggregation-induced emission (AIE) behavior was synthesized, which can interact with picric acid through photoinduced electron transfer (PET). Scanning electron microscopy (SEM) and dynamic light scattering (DLS) indicate that the enhanced emission of the compounds is related to the formation of nano-aggregates. It is well known that an important source of mechanochromic fluorescence (MCF) characteristic materials is the compound with AIE characteristics. The chemosensing test paper prepared by aggregated nanoparticles based on AIE properties is often subjected to external friction or squeeze during transportation or storage, resulting in changes of their optical properties, and destruction of test paper followed. Therefore, the development of compounds with AIE properties and stable optical properties in the presence of external stimuli is particularly important for chemosensing test paper. Molecular dynamics simulation (MDS) shows that the presence of hydrophobic cycloalkyl group in CB-CYH, which caused the molecules to be closely interspersed with each other; hence, it is difficult to change the microstructure and stacking mode of molecules by external stimulation simultaneously; the optical properties are not changed by external stimuli. Therefore, the test paper based on the AIE effect of CB-CYH was developed as chemosensing test paper for the detection of nitroaromatics.

1. Introduction

The problem of human health is threatened by explosive residues from terrorist bombings, and military exercises are becoming more and more serious. The nitroaromatics are commonly used as explosive materials, and the methods of detection of nitroaromatic explosives are various [1], such as metal detectors [2], thermal neutron analysis [3], electrochemical assays [4], Raman spectroscopy [5], gas chromatography [6], X-ray imaging [7], and mass spectrometry [8]. However, the disadvantages are obvious, such as time-consuming, or expensive, or complicated processing. So many researchers turn their attention to photoluminescence (PL) sensor [9–12], which is a low-cost with high-sensitivity, easy-to-operate, and a new type of very promising method. The PL sensor is usually based on a photoinduced electron

transfer (PET) mechanism that is from an electron-rich group of the sensor to an electron-deficient nitroaromatic. However, the practical application of traditional PL sensor is hindered by the phenomenon of aggregation quenching (ACQ) [13].

Since Tang's group [14–16] discovered compounds with aggregate-induced emission (AIE) feature, more and more people have paid attention to this; these compounds can not only be widely used in luminescent polymers, explosive detection [17, 18], mechanochromic fluorescence [19], optoelectronic materials, biosensors, and gels but also successfully solve the ACQ problem [20–28]. Compounds with AIE properties are nonluminous when dissolved in a good solvent but are completely opposite in the aggregated state. The reason for strong emission in the aggregate state is that the formation of aggregated nanoparticles restricted intramolecular

rotation (RIR), the nonradiative channels are blocked and radiation paths are opened [29]. PL sensors based on AIE have successfully solved the problems of traditional sensors with ACQ properties.

Chemosensing test papers are widely used due to their portability, low price, and easy storage [30–32]. It is well known that an important source of mechanochromic fluorescence (MCF) characteristic materials is the compounds with AIE characteristics. Chemosensing test paper based on AIE properties is often subjected to external friction or squeeze during transportation or storage, resulting in changes in their optical properties. Fortunately, a new D-π-A barbituric acid derivative CB-CYH with aggregation-induced emission (AIE) behavior was synthesized, of which the optical properties are not changed by external stimuli. Hence, the chemosensing test paper was prepared by aggregated nanoparticles of CB-CYH, which was developed for the detection of nitroaromatics.

2. Experimental Section

2.1. Materials. 1,3-Dicyclohexylurea, dimethylformamide, malonyl chloride, and 9-phenyl-9H-carbazole (A.R., 99%) were purchased from Jiu ding Chemical, and which without further purification. DMF is usually dried sequentially by molecular sieves (4 Å), CaH_2 and sodium sand successively, and distilled prior to use.

2.2. Characterizations. UV-vis spectra were registered by UV-2500 spectrometer. Emission spectra were recorded on an F-4600 fluorescence spectrophotometer. ^{1}H NMR (400 MHz) spectra were recorded on AVANCE II 400 spectrometer. FT-IR spectra were measured by a Nicolet 380 spectrometer using the KBr pellet method.

2.3. Computation. The optimizations and electronic structure calculation for the CB-CYH were done at B3LYP/def2-SVP level with Gaussian09 software. Solvation effects were incorporated by molecular dynamics simulations (MDS) [33] solvation models with water as solvent. The dispersion correction was conducted by Grimme's D3 version with BJ damping function [34].

Eight optimized molecules of CB-CYH were randomly dissolved in 400 water molecules, respectively, to form initial systems with the same cubic simulation lattice ($x = 28.89$ Å, $y = 28.89$ Å, and $z = 28.89$ Å). Subsequently, all-atomic molecular dynamics simulations (MDS) were performed for the system in BIOVIA Materials Studio 2019 Forcite packages. The simple point charge (SPC) model [35, 36], which can accurately describe the water solution environment [37], is adopted for all water molecules.

The MD simulation of all systems can be performed after charges and potentials are assigned to each atom. The long-range electrostatic interactions have been accounted for using the Ewald method. The total energy is written as a combination of valence terms including diagonal and off-diagonal cross-coupling terms and nonbond interaction terms, which include the Coulombic and Lennard-Jones functions for electrostatic and van der Waals interactions,

$$E = E_{\text{bonds}} + E_{\text{angles}} + E_{\text{dihedrals}} + E_{\text{cross}} + E_{\text{VDW}} + E_{\text{elec}}, \quad (1)$$

where E_{VDW} and E_{elec} are given by the Eq. (2):

$$E_{\text{non-bond}} = E_{\text{VDW}} + E_{\text{elec}} = \sum \varepsilon_{ij} \left[2\left(\frac{\sigma_{ij}}{r_{ij}}\right)^9 - 3\left(\frac{\sigma_{ij}}{r_{ij}}\right)^6 \right] + \sum \frac{q_i q_j}{r_{ij}}. \quad (2)$$

The MDS was performed using the COMPASS force field [38, 39], which is a force field for atomistic simulation of common organic molecules based on the state-of-the-art ab initio and empirical parametrization techniques. The simulations were equilibrated at constant temperature (298.15 K) and volume (NPT) for 30 ns.

2.4. Synthesis of Compounds. The synthetic routes of CB-CYH which include are illustrated in Scheme 1. In addition to this, the synthesis step of 1,3-dicyclohexylbarbituric acid (1) and 9-phenyl carbazole-3-carbaldehyde (2) can be found from Ref. [40, 41], respectively.

2.4.1. Synthesis of CB-CYH. A mixture of 2 (3 mmol) and 1 (3 mmol) in (10 ml) EtOH was refluxed for 4 hr. After filtration, the filtrate was concentrated under reduced pressure and purified by column chromatography (ethyl acetate : petroleum ether = 2 : 1). Production: 90%. ^{1}H NMR (400 MHz, Chloroform-*d*) δ 8.35 (s, 1H), 8.14 (d, *J* = 8.8 Hz, 2H), 7.36 (t, *J* = 7.8 Hz, 4H), 7.21 (d, *J* = 7.6 Hz, 6H), 6.95 (d, *J* = 8.7 Hz, 2H), 4.74 (dd, *J* = 14.0, 10.5 Hz, 2H), 2.37 (q, *J* = 12.5 Hz, 4.H), 1.84 (s, 3H), 1.67 (s, 4H), 1.42-1.33 (m, 4H), 1.31-1.22 (m, 3H) (Figure S1) FT-IR (KBr): 1669 cm^{-1} (C=O) (Figure S2). HRMS (ESI) *m/z*: [M + H]$^+$ calcd for $C_{35}H_{35}N_3O_3$, 545.38328; found, 545.27512 (Figure S3). ^{13}C NMR (126 MHz, Chloroform-*d*) δ 163.54, 161.57, 156.45, 1482.84, 145.37, 138.22, 129.60, 128.72, 127.25, 126.59, 115.47, 55.15, 29.39, 25.67, 25.12 (Figure S4).

3. Results and Discussion

3.1. Optical Properties. The absorption and emission spectra for CB-CYH are presented in Figure 1(a). The maximum absorption wavelength of CB-CYH was at 421 nm, which can be attributed to the intramolecular charge transfer (ICT) [42] from the carbazole group to the barbituric acid group, which can also be confirmed by density functional theory (DFT) calculations (Figure 1(b)). It should note that the absorption peak at 230-350 nm belongs to the π-$\pi *$ electron transition of the corresponding benzene ring unit. In dilute THF solution, CB-CYH showed dim emission with emission wavelengths at 517 nm.

The AIE property of CB-CYH was studied in THF/H$_2$O system. As shown in Figure 2(a), the emission intensity of CB-CYH increased by 4.4 folds with f_w increased from 0% to 80%, because of the formation of nano-aggregates; however, as the f_w increases further, the emission intensity decreases, which is due to the the low solubility of CB-CYH
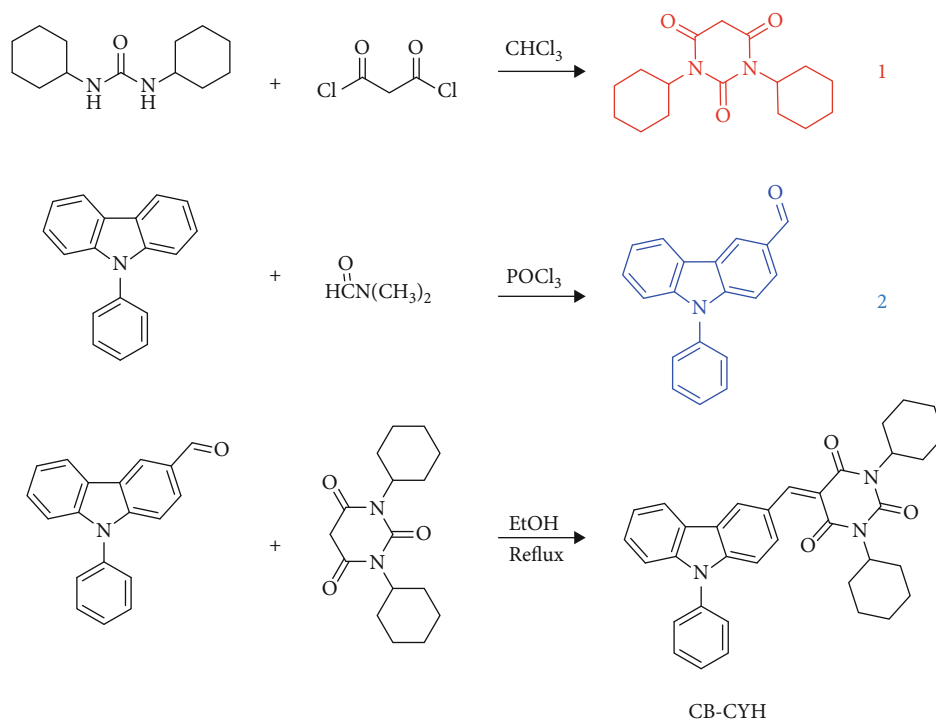
Scheme 1: Synthetic routes to CB-CYH.

(a)

(b)
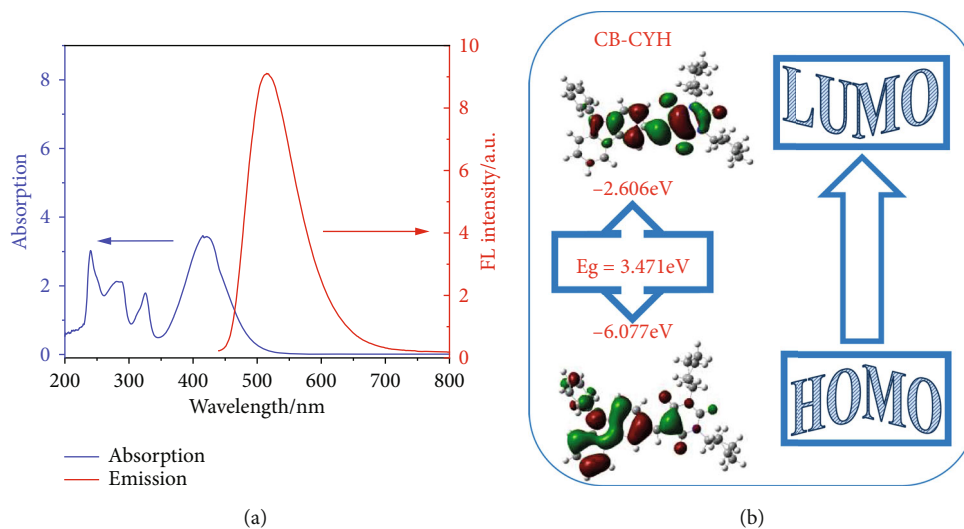
Figure 1: (a) UV-visible absorption spectrum and emission spectrum of CB-CYH in pure THF (10^{-4} M). (b) Electron density distributions of LUMO and HOMO molecular orbitals of CB-CYH calculated by the B3LYP/6-31Gd program. (HOMO: the highest occupied molecular orbital energy; LUMO: the lowest unoccupied molecular orbital energy).

at high water content, resulting in rapid precipitation of the compounds, the total number of emission molecules decreases in the solution, and fluorescence reduction follows [43]. Fluorescent photograph of CB-CYH in THF/H_2O mixtures with different f_w, irradiated by 365 nm wavelength also demonstrate that CB-CYH is AIE active compound.

The fluorescence quantum yields of pure solution and aggregate state are determined relative to coumarin 307 in ethanol solution as a quantum yield standard (ΦF (fluorescence quantum yield) = 56%). The coumarin 307 is selected as a standard to study the ΦF due to its maximum absorption and emission wavelength (395 nm and 500 nm, respectively), which are close to the synthesized AIE compounds in this work; the fluorescence quantum yields of compound in the pure solution and aggregate state are 1.8% and 7.4%, respectively.

Scanning electron microscopy (SEM) and dynamic light scattering (DLS) were used to detect the morphology and size of nano-aggregates in $f_w = 80\%$ (Figure 3) which show the presence of spherical and blocky aggregates. As shown in

(a)

(b)
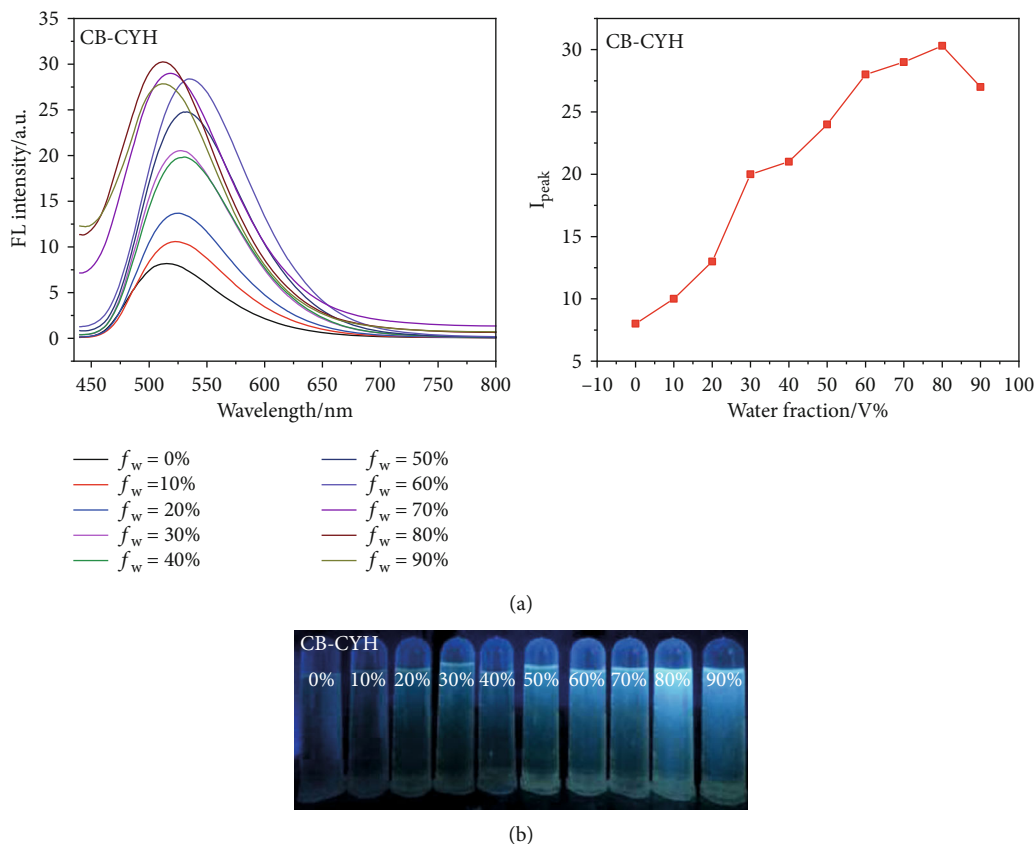
FIGURE 2: (a) Fluorescence spectrum of CB-CYH in THF/H_2O mixtures with different f_w. (b) Fluorescent photograph of CB-CYH in THF/H_2O mixtures with different f_w, irradiated by 365 nm wavelength.
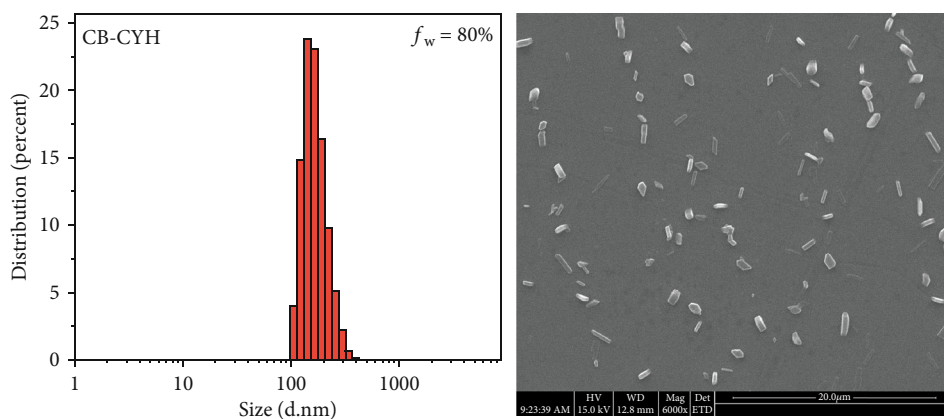
FIGURE 3: SEM images and particle size distribution histograms of CB-CYH in a THF/H_2O mixture ($f_w = 80\%$) (solution concentration: 10^{-4} M).

Figure 3, the solution was uniformly stable at a water content of 80%, and the average diameters (d) of the CB-CYH aggregates was 180 nm, respectively. These data indicate that the enhanced emission of the compound is related to the formation of nano-aggregates.

As shown in Figure S5, The fluorescence intensity of CB-CYH ($f_w = 80\%$) did not change within 30 minutes. These results mean that CB-CYH ($f_w = 80\%$) has excellent photo-

stability. In addition, the average diameter (d) of CB-CYH aggregate has basically no change within half an hour (Figure S6).

It is well known that an important source of mechano-chromic fluorescence (MCF) property materials are compounds with AIE properties. However, it can be seen from Figure 4(a) that there is almost no change in color and fluorescence after grinding of CB-CYH; simultaneously,

(a)

(b)

(c)
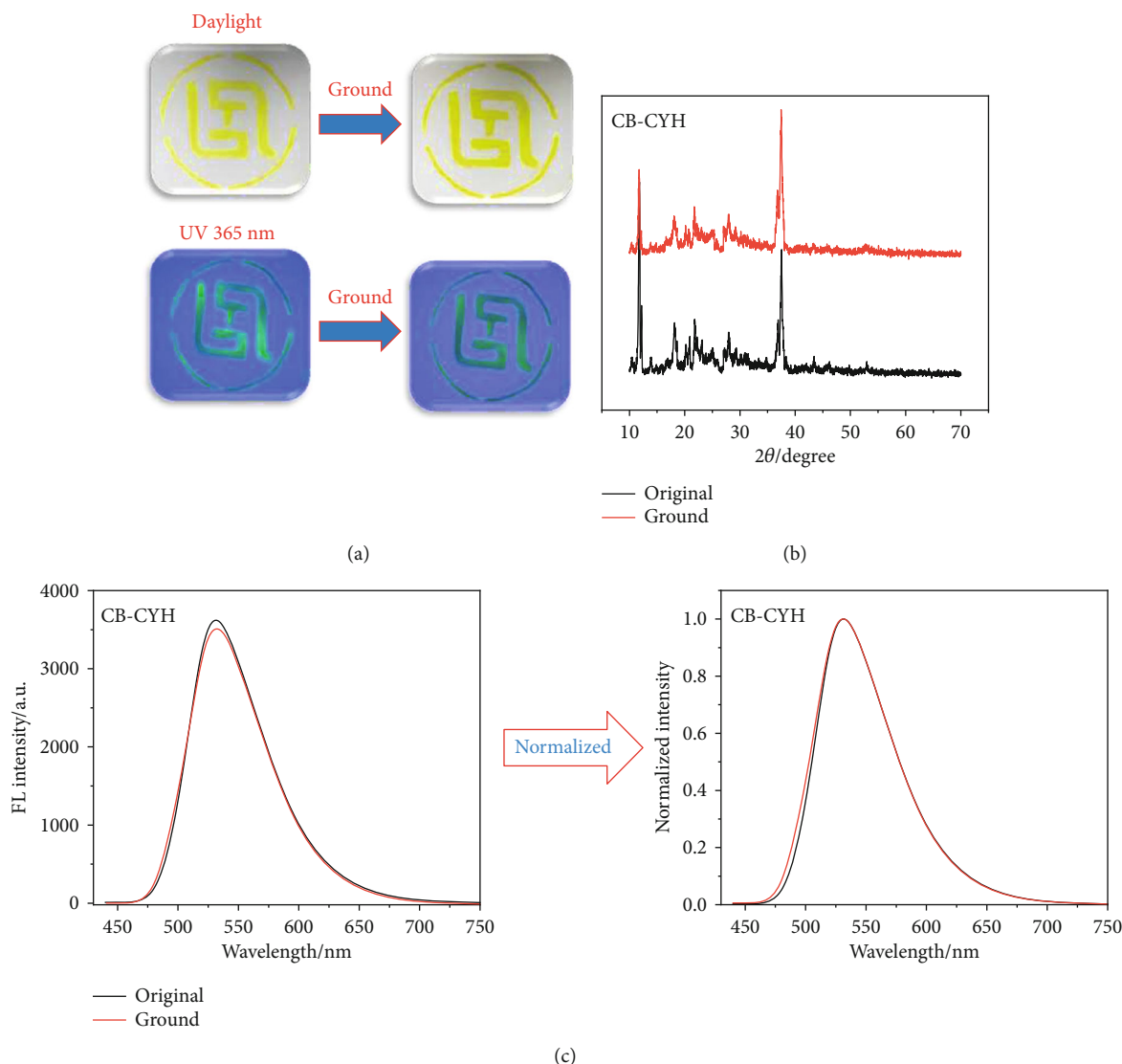
FIGURE 4: (a) Photographs of colour and fluorescence of CB-CYH in original and ground under daylight and UV 365 nm. (b) XRD patterns of CB-CYH in original and ground. (c) Left: fluorescence spectrum of CB-CYH of solid powder in original and ground. Right: normalized fluorescence spectrum of CB-CYH of solid powder in original and ground.

the XRD diffraction peak of CB-CYH almost unchanged (Figure 4(b)). It can also be seen from Figure 4(c) that the emission spectrum of CB-CYH has almost no change before and after grinding, regardless of the emission wavelength or intensity. The structure of the CB-CYH showed strong distortion, but not MCF property, which inspired our intense curiosity.

3.2. Molecular Dynamics Simulations (MDS). The behavior of CB-CYH in the aggregated state was studied by MDS. As shown in Figure 5(a), all the molecules of the formed nano-aggregates together under high water content, and at the same time, the structure of CB-CYH shows a strong defor-mation. Among them, the electron repulsion and strong intermolecular interactions between aryl rings in carbazoles lead to extremely curved configurations (Figure 5(b)), and from the distribution of dihedral angles between several moieties, the main dihedral angles of angle-1, angle-2, and

angle-3 are 50°, 155°, and 155°, respectively. Meanwhile, the cyclohexane on the N atom of the barbiturate acid exhibits extremely distorted chair conformation, which further increases the degree of distortion of the molecule CB-CYH (Figure 5(c)). These data indicate that the molecule takes 3D conformation, which makes it easy to pack closely in the crystalline state. As shown in Figure 4(d), because of hydrophobic interactions, the substituents cyclohexane in CB-CYH tend to aggregate together. Hydrophobic interac-tions pull all molecules together and spread each other, which formed aggregated nanoparticles to lock the molecules. This also proves why CB-CYH does not have MCF property.

3.3. Chemosensing Test Paper. The chemosensing test paper was prepared by soaking Whatman filter paper in CB-CYH ($f_w = 80\%$) (10^{-4} M) solution (aggregated nanoparticles) and then dried it in the air stream. Picric acid (PA) was selected as representative of nitroaromatic explosives. First,

(a)

(b)

(c)

(d)
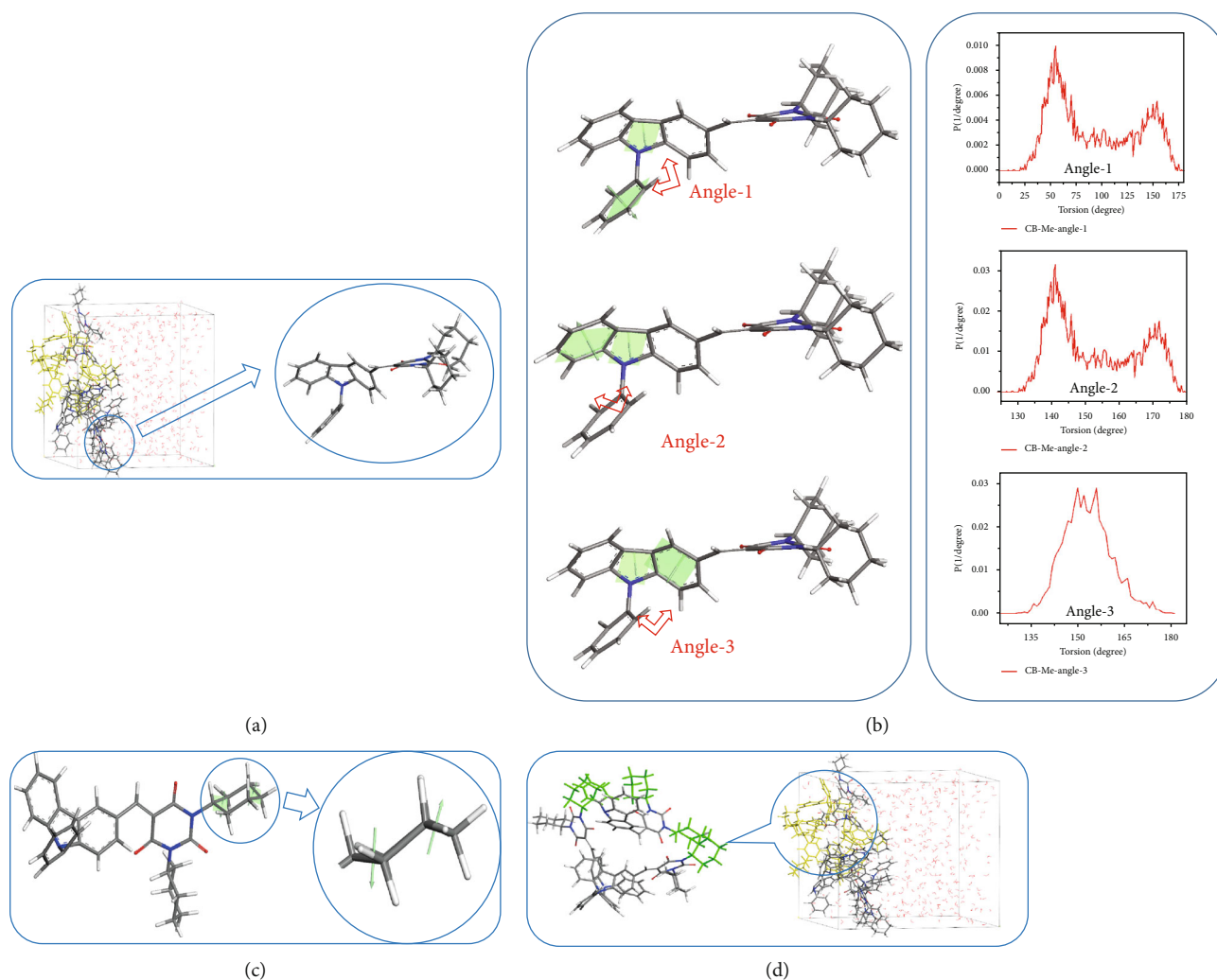
FIGURE 5: (a) The molecule conformation and aggregation structure of CB-CYH by MDS. (b) Dihedral angle of the substituted carbazole in CB-CYH. (c) Configurations of substituted cyclohexane on the N atom of barbituric acid in CB-CYH. (d) Hydrophobic force of cyclohexane in CB-CYH.

(a)

(b)
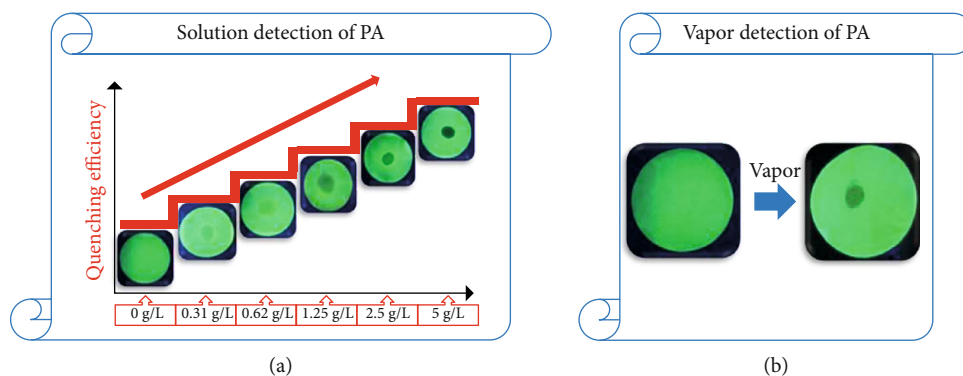
FIGURE 6: Paper test. (a) Solution mode detection of PA. (b) Gas phase mode detection of PA.

the PA test was performed at solution state. As shown in Figure 6(a), the test paper emits bright blue-green fluorescence without adding PA solution, when adding 0.31 g/L PA solution, the test paper shows a slight quenching. It is found that the quenching efficiency increases with the increase of PA concentration, when the concentration reaches to 5 g/L, the area of adding PA solution is completely quenched. Next, perform a steam mode test. Place the chemical sensing test paper in a cylindrical glass container filled with solid PA (0.2 g) maintained at a constant temperature

FIGURE 7: (a) Absorption spectrum of PA and emission spectrum of CB-CYH. (b) Energy levels, energy gaps, and electron cloud distributions of the HOMO and LUMO of PA and CB-CYH calculated by the B3LYP/6-325 31G (d) program.

of 45°C for 5 minutes (under standard atmospheric pressure). The circular area of the test paper was exposed to PA vapor. It can be seen from Figure 6(b) that the fluorescence of the test paper is significantly quenched in the area exposed to the PA vapor. These results showed that CB-CYH-based chemosensing test paper can detect picric acid.

3.3.1. Sensing Mechanism. As shown in Figure 7, the absorption spectrum of PA and emission spectrum of CB-CYH were tested, which to explore the quenching mechanism. It noticed from Figure 7(a) that the absorption spectrum of PA and the emission spectrum of CB-CYH hardly overlap, and the results showed that the quenching mechanism of CB-CYH was photoinduced electron transfer (PET) [44–46].

In explosives containing nitro groups, which has a strong electron-withdrawing ability, resulting in that is extremely deficient in electrons. However, the fluorescent compound as the electron-donor is rich in electrons, and it is easy to interact with the electron-deficient substance by charge transfer interaction and bind under the condition of light irradiation. In the process of the photoinduced electron transfer (PET) mechanism, the fluorescent material provides electrons to the ground state of the electron-deficient nitroaromatic explosive, and part of it will return to the ground state in the form of a complex, thus losing fluorescence. Some electrons will return to the electron donor and still emit fluorescence. The driving force for the PET mechanism is the difference between the LUMO energy levels between the donor and acceptor, namely, the size of the energy gap difference.

As shown in Figure 7(b), the energy levels and electron cloud distributions of the HOMO and LUMO of TNT and CB-CYH were calculat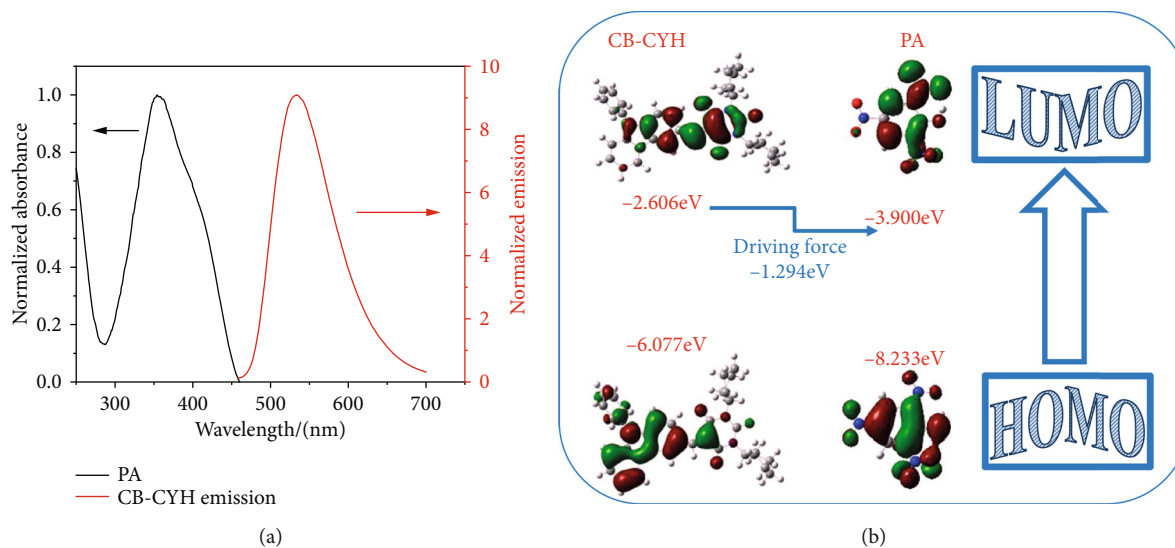ed by the B3LYP/6-325 31G (d) program. When the excited CB-CYH is exposed to TNT, the excited electrons are transferred from the LUMO of CB-CYH to the LUMO of PA. The main driving force of PET is the difference between the LUMO value of CB-CYH and PA, which is -1.924 eV.

4. Conclusions

In summary, the chemosensing test paper was prepared by aggregated nanoparticles of CB-CYH, which was developed for the detection of nitroaromatics. MDS showed that CB-CYH with a strong twist structure cannot cause changes in fluorescence, color, and emission wavelength by external stimuli due to the close interpenetration between molecules. Hence, the chemosensing test paper will not be damaged by squeeze and friction during transportation and storage.

Data Availability

The data used to support the findings of this study are available from the corresponding author upon request.

Conflicts of Interest

The authors declare that they have no conflicts of interest.

Acknowledgments

Supplementary Materials

In the supplementary materials mainly included with 1H NMR, 13C NMR, FT-IR, and mass spectra of CB-CYH, light stability of CB-CYH nano-aggregates, and particle size distribution of CB-CYH in a THF/H2O mixture (fw = 80%). Figure S1. 1H NMR of CB-CYH in Chloroform-d. Figure S2. FT-IR spectra of CB-CYH. Figure S3. HRMS spectra of CB-CYH. Figure S4. 13C NMR of CB-CYH in Chloroform-d. Figure S5. CB-CYH light stability in nano-aggregates state.

Figure S6. Particle size distribution histograms of CB-CYH in a THF/H2O mixture (fw = 80%) was left at room temperature for half an hour (solution concentration: 10-4 M). *(Supplementary Materials)*

References

[1] H. Zhou, M. H. Chua, B. Z. Tang, and J. Xu, "Aggregation-induced emission (AIE)-active polymers for explosive detection," *Polymer Chemistry*, vol. 10, no. 28, pp. 3822–3840, 2019.

[2] J. M. Sylvia, J. A. Janni, J. D. Klein, and K. M. Spencer, "Surface-enhanced Raman detection of 2, 4-dinitrotoluene impurity vapor as a marker to locate landmines," *Analytical chemistry*, vol. 72, no. 23, pp. 5834–5840, 2000.

[3] W. Dong, S. Xue, P. Lu et al., "Functionality of peripheral side chain for enhanced performance of conjugated polymer-F8BT as an example," *Journal of Polymer Science Part A: Polymer Chemistry*, vol. 49, no. 21, pp. 4549–4555, 2011.

[4] H. Ma, L. Yao, P. Li, O. Ablikim, Y. Cheng, and M. Zhang, "Highly sensitive and selective fluorometric/electrochemical dual-channel sensors for TNT and DNT explosives," *Chemistry-A European Journal*, vol. 20, no. 37, pp. 11655–11658, 2014.

[5] G. A. Eiceman and J. A. Stone, "Ion Mobility Spectrometers in National defence," *Analytical Chemistry*, vol. 76, no. 21, pp. 390A–397A, 2004.

[6] K. Håkansson, V. Ramal, A. Coorey Roman, L. Zubarev Victor, and T. P. Håkansson, "Low-mass ions observed in plasma desorption mass spectrometry of high explosives," *Journal of mass spectrometry*, vol. 35, no. 3, pp. 337–346, 2000.

[7] S. F. Hallowell, "Screening people for illicit substances: a survey of current portal technology," *Talanta*, vol. 54, no. 3, pp. 447–458, 2001.

[8] J. C. Mathurin, T. Faye, A. Brunot, J. C. Tabet, G. Wells, and C. Fuché, "High-pressure ion source combined with an in-axis ion trap mass spectrometer. 1. Instrumentation and applications," *Analytical chemistry*, vol. 72, no. 20, pp. 5055–5062, 2000.

[9] N. Venkatramaiah, S. Kumar, and S. Patil, "Fluoranthene based fluorescent chemosensors for detection of explosive nitroaromatics," *Chemical Communications*, vol. 48, no. 41, pp. 5007–5009, 2012.

[10] N. Venkatramaiah, S. Kumar, and S. Patil, "Femtogram detection of explosive nitroaromatics: fluoranthene-based fluorescent chemosensors," *Chemistry-A European Journal*, vol. 18, no. 46, pp. 14745–14751, 2012.

[11] H. Nie, Y. Lv, L. Yao et al., "Fluorescence detection of trace TNT by novel cross-linking electropolymerized films both in vapor and aqueous medium," *Journal of Hazardous Materials*, vol. 264, pp. 474–480, 2014.

[12] K. R. Ghosh, S. K. Saha, and Z. Y. Wang, "Ultra-sensitive detection of explosives in solution and film as well as the development of thicker film effectiveness by tetraphenyl-lethene moiety in AIE active fluorescent conjugated polymer," *Polymer Chemistry*, vol. 5, no. 19, pp. 5638–5643, 2014.

[13] B. Chen, Y. Jiang, B. He et al., "Synthesis, structure, photoluminescence, and electroluminescence of siloles that contain planar fluorescent chromophores," *Chemistry - An Asian Journal*, vol. 9, no. 10, pp. 2937–2945, 2014.

[14] M. H. Chua, H. Zhou, T. T. Lin, J. Wu, and J. W. Xu, "Aggregation-induced emission active 3, 6-bis (1, 2, 2-triphenylvinyl) carbazole and bis (4-(1, 2, 2-triphenylvinyl) phenyl) amine-based poly (acrylates) for explosive detection," *Journal of Polymer Science Part A: Polymer Chemistry*, vol. 55, no. 4, pp. 672–681, 2017.

[15] H. Zhou, X. Wang, T. T. Lin, J. Song, B. Z. Tang, and J. Xu, "Poly (triphenyl ethene) and poly (tetraphenyl ethene): synthesis, aggregation-induced emission property and application as paper sensors for effective nitro-compounds detection," *Polymer Chemistry*, vol. 7, no. 41, pp. 6309–6317, 2016.

[16] H. Zhou, Q. Ye, W. T. Neo et al., "Electrospun aggregation-induced emission active POSS-based porous copolymer films for detection of explosives," *Chemical Communications*, vol. 50, no. 89, pp. 13785–13788, 2014.

[17] K. Li, R. H. Yu, C. M. Shi, F. R. Tao, T. D. Li, and Y. Z. Cui, "Electrospun nanofibrous membrane based on AIE-active compound for detecting picric acid in aqueous solution," *Sensors and Actuators B: Chemical*, vol. 262, pp. 637–645, 2018.

[18] D. Ding, K. Li, B. Liu, and B. Z. Tang, "Bioprobes based on AIE fluorogens," *Accounts of Chemical Research*, vol. 46, no. 11, pp. 2441–2453, 2013.

[19] Z. Zhao, B. He, and B. Z. Tang, "ChemInform Abstract: Aggregation-Induced Emission of Siloles," *Cheminform*, vol. 46, no. 45, pp. 5347–5365, 2015.

[20] H. Zhou, J. Li, M. H. Chua, H. Yan, B. Z. Tang, and J. Xu, "Poly (acrylate) with a tetraphenylethene pendant with aggregation-induced emission (AIE) characteristics: highly stable AIE-active polymer nanoparticles for effective detection of nitro compounds," *Polymer Chemistry*, vol. 5, no. 19, pp. 5628–5637, 2014.

[21] W. Z. Yuan, Z.-Q. Yu, Y. Tang et al., "High solid-state efficiency fluorescent main chain liquid crystalline polytriazoles with aggregation-induced emission characteristics," *Macromolecules*, vol. 44, no. 24, pp. 9618–9628, 2011.

[22] H.-J. Zhang, Y. Tian, F.-r. Tao et al., "Detection of nitroaromatics based on aggregation induced emission of barbituric acid derivatives," *Spectrochimica Acta Part A: Molecular and Biomolecular Spectroscopy*, vol. 222, pp. 117168–117168, 2019.

[23] H. Zhang, Y. Cui, F. Tao, D. Zhang, Z. Xu, and L. Guo, "Multi-purpose barbituric acid derivatives with aggregation induced emission," *Spectrochimica Acta Part A: Molecular and Biomolecular Spectroscopy*, vol. 223, pp. 1386–1425, 2019.

[24] R. Yoshii, K. Suenaga, K. Tanaka, and Y. Chujo, "Mechano-fluorochromic materials based on aggregation-induced emission-active boron ketoiminates: regulation of the direction of the emission color changes," *Chemistry-A European Journal*, vol. 21, no. 19, pp. 7231–7237, 2015.

[25] J. Wang, J. Mei, R. Hu, J. Z. Sun, A. Qin, and B. Z. Tang, "Click synthesis, aggregation-induced emission, E/Z isomerization, self-organization, and multiple chromisms of pure stereoisomers of a tetraphenylethene-cored luminogen," *Journal of the American Chemical Society*, vol. 134, no. 24, pp. 9956–9966, 2012.

[26] X. Gu, G. Zhang, Z. Wang, W. Liu, L. Xiao, and D. Zhang, "A new fluorometric turn-on assay for alkaline phosphatase and inhibitor screening based on aggregation and deaggregation

of tetraphenylethylene molecules," *Analyst*, vol. 138, no. 8, pp. 2427–2431, 2013.

[27] P. Xue, B. Yao, J. Sun, Z. Zhang, and R. Lu, "Emission enhancement of a coplanar π-conjugated gelator without any auxiliary substituents," *Chemical Communications*, vol. 50, no. 71, pp. 10284–10286, 2014.

[28] Z. Zhu, J. Qian, X. Zhao et al., "Stable and size-tunable aggregation-induced emission nanoparticles encapsulated with nanographene oxide and applications in three-photon fluorescence bioimaging," *ACS Nano*, vol. 10, no. 1, pp. 588–597, 2015.

[29] D. Li, Y. Zhang, Z. Fan, J. Chen, and J. Yu, "Coupling of chromophores with exactly opposite luminescence behaviours in mesostructured organosilicas for high-efficiency multicolour emission," *Chemical Science*, vol. 6, no. 11, pp. 6097–6101, 2015.

[30] S. Li, Y. Shang, E. Zhao et al., "Color-tunable and highly solid emissive AIE molecules: synthesis, photophysics, data storage and biological application," *Journal of Materials Chemistry C*, vol. 3, no. 14, pp. 3445–3451, 2015.

[31] M. Wang, X. Liu, H. Lu, H. Wang, and Z. Qin, "Highly selective and reversible chemosensor for Pd2$^+$ detected by fluorescence, colorimetry, and test paper," *ACS Applied Materials & Interfaces*, vol. 7, no. 2, pp. 1284–1289, 2015.

[32] X. Yong, M. Su, W. Wang, Y. Yan, J. Qu, and R. Liu, "A naked-eye chemosensor for fluoride ions: a selective easy-to-prepare test paper," *Organic & Biomolecular Chemistry*, vol. 11, no. 14, pp. 2254–2257, 2013.

[33] A. V. Marenich, C. J. Cramer, and D. G. Truhlar, "Universal solvation model based on solute electron density and on a continuum model of the solvent defined by the bulk dielectric constant and atomic surface tensions," *The Journal of Physical Chemistry B*, vol. 113, no. 18, pp. 6378–6396, 2009.

[34] S. Grimme, S. Ehrlich, and L. Goerigk, "Effect of the damping function in dispersion corrected density functional theory," *Journal of Computational Chemistry*, vol. 32, no. 7, pp. 1456–1465, 2011.

[35] H. J. C. Berendsen, J. P. M. Postma, W. F. Van Gunsteren et al., *Intermolecular Forces*, B. Pullman, Ed., Reidel, Dordrecht, 1981.

[36] H. J. C. Berendsen, J. R. Grigera, and T. P. Straatsma, "The missing term in effective pair potentials," *Journal of Physical Chemistry*, vol. 91, no. 24, pp. 6269–6271, 1987.

[37] M. J. Wiedemair and T. S. Hofer, "Towards a dissociative SPC-like water model–probing the impact of intramolecular Coulombic contributions," *Physical Chemistry Chemical Physics*, vol. 19, no. 47, pp. 31910–31920, 2017.

[38] H. Sun, P. Ren, and J. R. Fried, "The COMPASS force field: parameterization and validation for phosphazenes," *Computational and Theoretical Polymer Science*, vol. 8, no. 1-2, pp. 229–246, 1998.

[39] H. Sun, "COMPASS: an ab initio force-field optimized for condensed-phase applications overview with details on alkane and benzene compounds," *The Journal of Physical Chemistry B*, vol. 102, no. 38, pp. 7338–7364, 1998.

[40] A. G. O'Brien, E. M. Ricci, and M. Journet, "Dehydration of an Insoluble Urea Byproduct Enables the Condensation of DCC and Malonic Acid in Flow," *Organic Process Research & Development*, vol. 22, no. 3, pp. 399–402, 2018.

[41] S. Xue, W. Liu, X. Qiu, Y. Gao, and W. Yang, "Remarkable isomeric effects on optical and optoelectronic properties of N-phenylcarbazole-capped 9, 10-divinylanthracenes," *The Journal of Physical Chemistry C*, vol. 118, no. 32, pp. 18668–18675, 2014.

[42] K. Li, Y. Zhang, B. Qiao et al., "Facile fabrication of AIE/AIEE-active fluorescent nanoparticles based on barbituric for cell imaging applications," *RSC Advances*, vol. 7, no. 48, pp. 30229–30241, 2017.

[43] K. Li, X. Su, Y. Wang et al., "D-π-A type barbituric derivatives: aggregation induced emission, mechanofluorochromic and solvatochromic properties," *Journal of Luminescence*, vol. 203, pp. 50–58, 2018.

[44] M. Natali, S. Campagna, and F. Scandola, "Photoinduced electron transfer across molecular bridges: electron-and hole-transfer superexchange pathways," *Chemical Society Reviews*, vol. 43, no. 12, pp. 4005–4018, 2014.

[45] M. Kaur, S. K. Mehta, and S. K. Kansal, "A fluorescent probe based on nitrogen doped graphene quantum dots for turn off sensing of explosive and detrimental water pollutant, TNP in aqueous medium," *Spectrochim Acta A Mol Biomol Spectrosc*, vol. 180, pp. 37–43, 2017.

[46] L. Yuan, W. Lin, K. Zheng, and S. Zhu, "FRET-based small-molecule fluorescent probes: rational design and bioimaging applications," *Accounts of Chemical Research*, vol. 46, no. 7, pp. 1462–1473, 2013.

Research Article

Green Synthesis of Carbon Dots from Grapefruit and Its Fluorescence Enhancement

Xinzhu Huo,[1] Yuxuan He,[1] Shiqi Ma,[1] Yingying Jia,[1] Jiaming Yu,[1] Yu Li,[2] and Qian Cheng [iD][1]

[1]*Key Laboratory of Bio-Based Material Science & Technology (Ministry of Education), College of Material Science and Engineering, Northeast Forestry University, Harbin 150040, China*
[2]*College of Science, Northeast Forestry University, Harbin 150040, China*

Correspondence should be addressed to Qian Cheng; chengqian66@163.com

In this study, undoped carbon quantum dots (UCQDs, UCQDs-peel) and N-doped carbon dots (NCQDs) were prepared by a facile one-pot environmentally friendly hydrothermal method using grapefruit as carbon sources in the absence and presence of area, respectively. The structure, morphology, and fluorescence properties of three samples were characterized by Fourier transform infrared spectroscopy (FT-IR), transmission electron microscopy (TEM), and photoluminescence (PL). It was found that three types of CQDs could emit blue fluorescence with different intensities when irradiated with ultraviolet light. Compared to the luminescence properties of UCQDs, NCQDs, and UCQDs-peel, it can be seen that the fluorescence intensity of NCQDs was strongest due to the presence of NH and C-N bonds.

1. Introduction

Carbon quantum dots (CQDs) have widespread application in light-emitting devices (LED), cancer therapy, thermometers, anticounterfeiting, and biosensors due to their unique and tunable optical properties, the low cost and environmentally friendly fabrication, and low cytotoxicity and a high resistance to photobleaching [1–5]. Recently, lots of researchers have been working on CQDs from the preparation to application, especially in green synthesis from some natural sources such as grass [6], leaves [7], flowers [8], cereal [9], and so on [10, 11]. However, in practice applications, CQDs are limited for its low luminescence intensity and single emission wavelength. So, the studies on the development of efficient and reproducible strategies to enhance the intensity and multicolor emission of CQDs would improve their practical applications in sensing, imaging, LED, and so on.

According to studies of the existing luminescence mechanism, the fluorescence intensity of CQDs was influenced by surface states [12] and the structure [13] and size [14] of the materials. So far, scientists have made some researches on the enhancement of fluorescence intensity and tunable multi-color emissions of CQDs in order to realize its practical application. All in all, there exist several strategies including prepared method [15], surface modification and passivation [16], different solvent [17] and heteroatom doping [18], high pressure [19], and so on [20]. For example, Wang and his coworkers successfully obtained fluorescence enhancement of CQDs via simple grinding, prepared using pyrene derivative (pyrene-1-butyric acid (PyBA)) as a carbon source; furthermore, they found that an apparent 20-30 times emission enhancement can be observed by the treatment of grinding, which was ascribed CQD-packed structure and morphology changes [21]. At the same time, Wang et al.'s team also studied the pressure-triggered aggregation-induced emission enhancement in red emission amorphous CQDs and revealed that the accumulation of R-CQD molecules triggered enhanced emissions under higher pressure by theoretical calculations [22]. Xu et al. reported a novel kind of (AA)-enhanced CQDs prepared based on the employment of green teas and ascorbic acid by adjusting its surface state. Moreover, they found that this new kind of (AA)-enhanced CQDs also reveals excellent antioxidant activity [23]. In addition, many studies have proved that
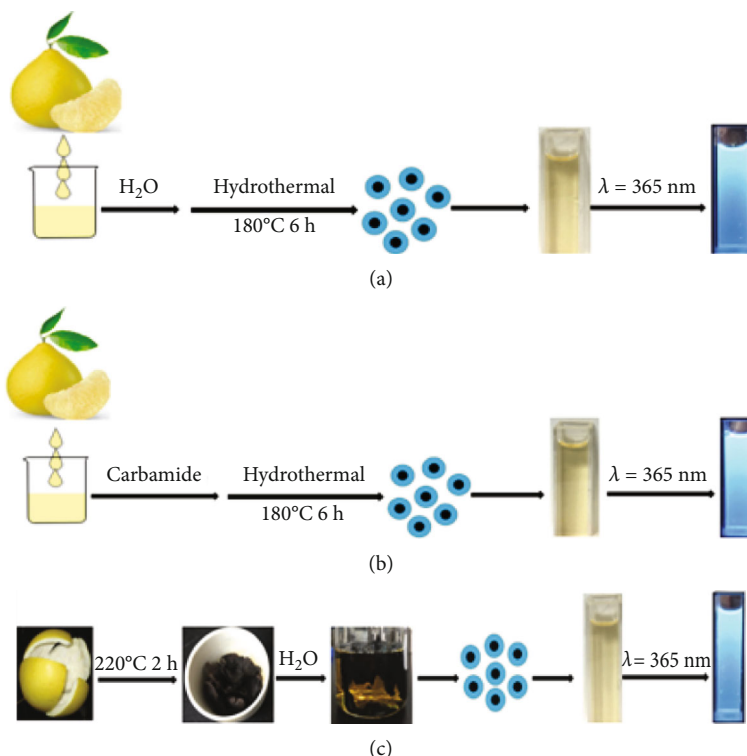
FIGURE 1: Illustration of the preparation procedures and fluorescence characterization of (a) UCQDs, (b) NCQDs, and (c) UCQDs-peel.

heteroatom like N, S, F, rear earth, and codoping can improve the luminescence performance of CQDs, such as tunable emission and multifunction properties [24, 25]. However, as we all know, there is little research on the fluorescence enhancement of CQDs by N-doping by a one-pot green synthesis method.

In this work, three kinds of carbon quantum dots (CQDs) are prepared using different sets of natural grapefruit and urea materials by a facile one-pot environmentally friendly hydrothermal method. Subsequently, the fluorescence properties of the prepared samples were investigated systematically. It was found that the prepared carbon quantum dots can emit blue fluorescence with different intensities when irradiated with ultraviolet light. Furthermore, the fluorescence intensity of CQDs can be improved by N-doping. Therefore, the method of enhancement fluorescence intensity by heteroatom doping holds a promising potential application in bioimaging, ion sensing, and LED.

2. Materials and Methods

2.1. Experimental Materials and Reagents. The fresh grapefruits were purchased from a local supermarket of Northeast Forestry University, China. Urea was obtained from Tianjin Tianli Chemical Reagents Ltd. Nitric acid was obtained from Xintian Chemical Reagents Ltd. (Shuangcheng, Heilongjiang Province). All of the reagents were of reagent grade and used without any further purification. The deionized water was prepared in the lab.
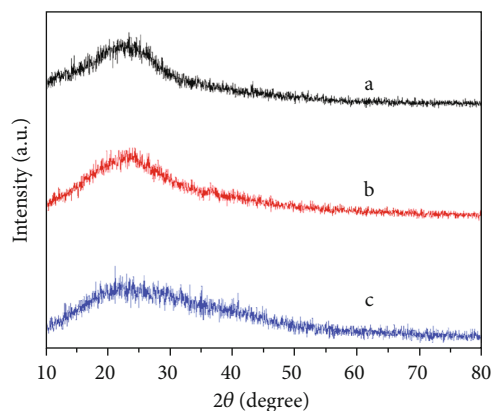
FIGURE 2: XRD patterns for (a) UCQDs, (b) NCQDs, and (c) UCQDs-peel.

2.2. Apparatus and Procedures. X-ray diffraction (XRD) patterns of the samples were recorded with a Rigaku D/max-γB diffractometer equipped with a rotating anode and a Cu Kα source ($\lambda = 0.154056$ nm). Transmission electron microscopy (TEM) images were obtained on a TecnaiG2 F20 electron microscope (FEI, Holland) with an accelerating voltage of 200 kV. Fourier-transform infrared spectra (FT-IR) were recorded on a Perkin Elmer TV1900 instrument (Waltham, MA, USA). Spectra were recorded from 650 to 4000 cm^{-1}, at a resolution of 4 cm^{-1}. UV–vis absorption spectra were examined by a U-3900 UV/Visible spectrometer (Hitachi Company). The fluorescence spectra were carried out on FluoroMax-4 fluorescence spectrometer.

(a)

(b)

(c)

(d)

(e)

(f)
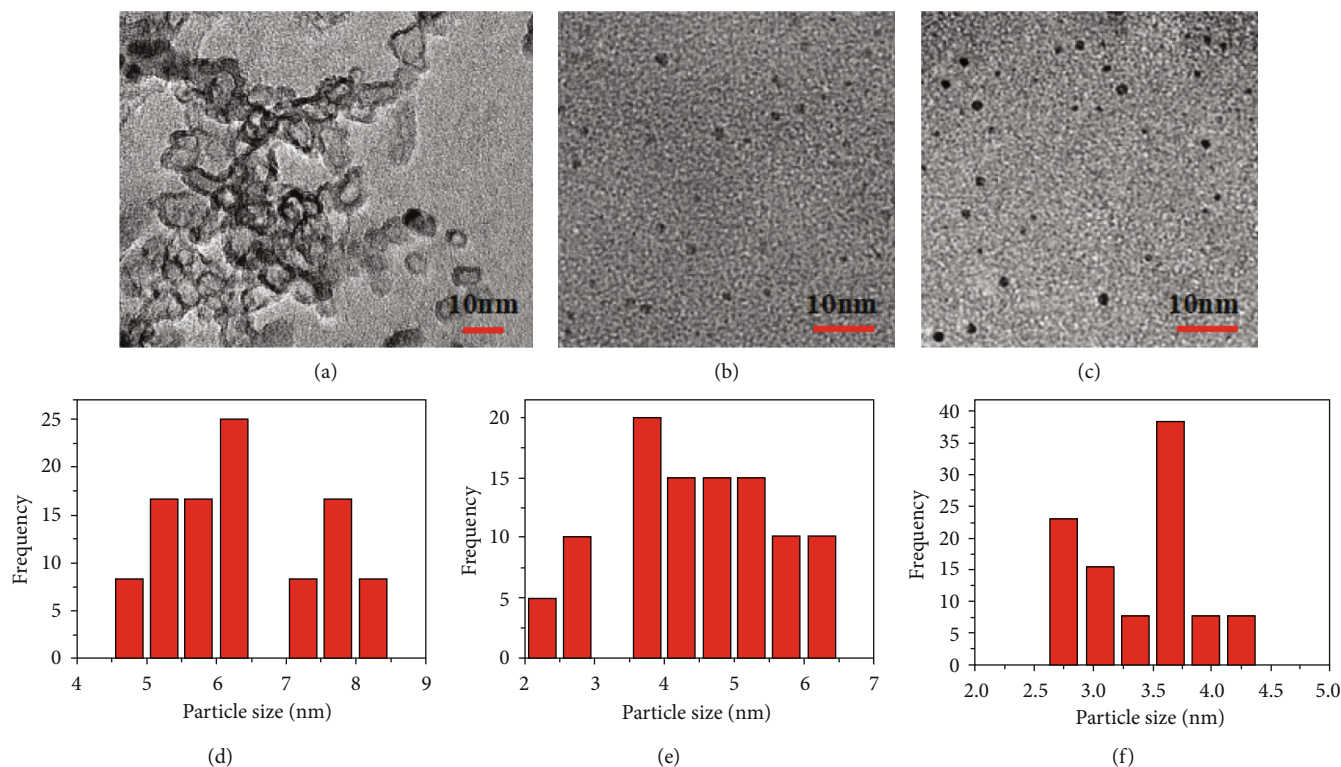
FIGURE 3: TEM images of (a) UCQDs, (b) NCQDs, and (c) UCQDs-peel. (d)–(f) are the corresponding size distributions obtained from TEM images.

2.3. Preparation of CQDs and NCQDs.

2.3. Preparation of CQDs and NCQDs. Figure 1 is the illustration of preparing three kinds of CQDs, and the process of the synthesizing CQDs is as follows:

After peeling the skin, the grapefruit was cut into small pieces and fresh juice was squeezed out. The obtained juice was centrifuged at 8000 rpm for 10 min; the above supernatant was passed through a filter paper to get pulp-free grapefruit juice. Then, 20 mL filtered grapefruit juice and 20 mL deionized water were mixed under stirring for 15 minutes. The above mixture was transferred into a Teflon-lined steel autoclave and heated at 180°C for 6 h. After the system was cooled to the room temperature, the obtained brown products were centrifuged for 15 min with a speed of 5000 rpm and then the resultant solution was dialyzed in a dialysis bag (MwCO = 3500 D) for 48 h. Finally, the products were freeze-dried for further analysis.

NCQDs were prepared by the same way by using grapefruit juice as the carbon source and carbamide (1 mol/L) as both the carbon and nitrogen source.

CQDs from grapefruit peel were prepared as follows: grapefruit peel was cleaned by the deionized water and then chopped. After that, the chopped grapefruit peel was heated at 220°C in a muffle furnace for 2 h. After cooling down at room temperature, 20 mL deionized water was added into the products and ultrasound stirred for 20 min. The solution was then filtered to remove precipitates and to obtain the CQDs-peel.

3. Results and Discussion

3.1. Structure and Morphology of Prepared Samples. The XRD patterns of three kinds of samples are shown in Figure 2. The
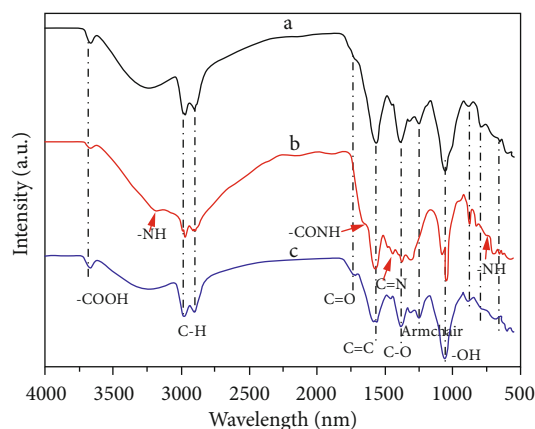
FIGURE 4: Comparison of Fourier transforms infrared spectra of carbon dots prepared by three carbon sources (a) UCQDs, (b) NCQDs, and (c) UCQDs-peel.

obvious broad peak around at 22.4° ($d = 0.396$ nm) were found in three samples of XRD patterns, which indicated highly disordered carbon atoms and graphitic structure of the CQDs. There is no other peak found in Figure 2, indicating three prepared samples were pure amorphous nature of CQDs.

The morphology and size of the prepared samples were measured by TEM. As shown in Figure 3, it was found that three kinds of samples had uniform spherical morphology. The diameter of the UCQDs is larger than those of NCQDs and UCQDs-peel. And their diameters are mainly distributed
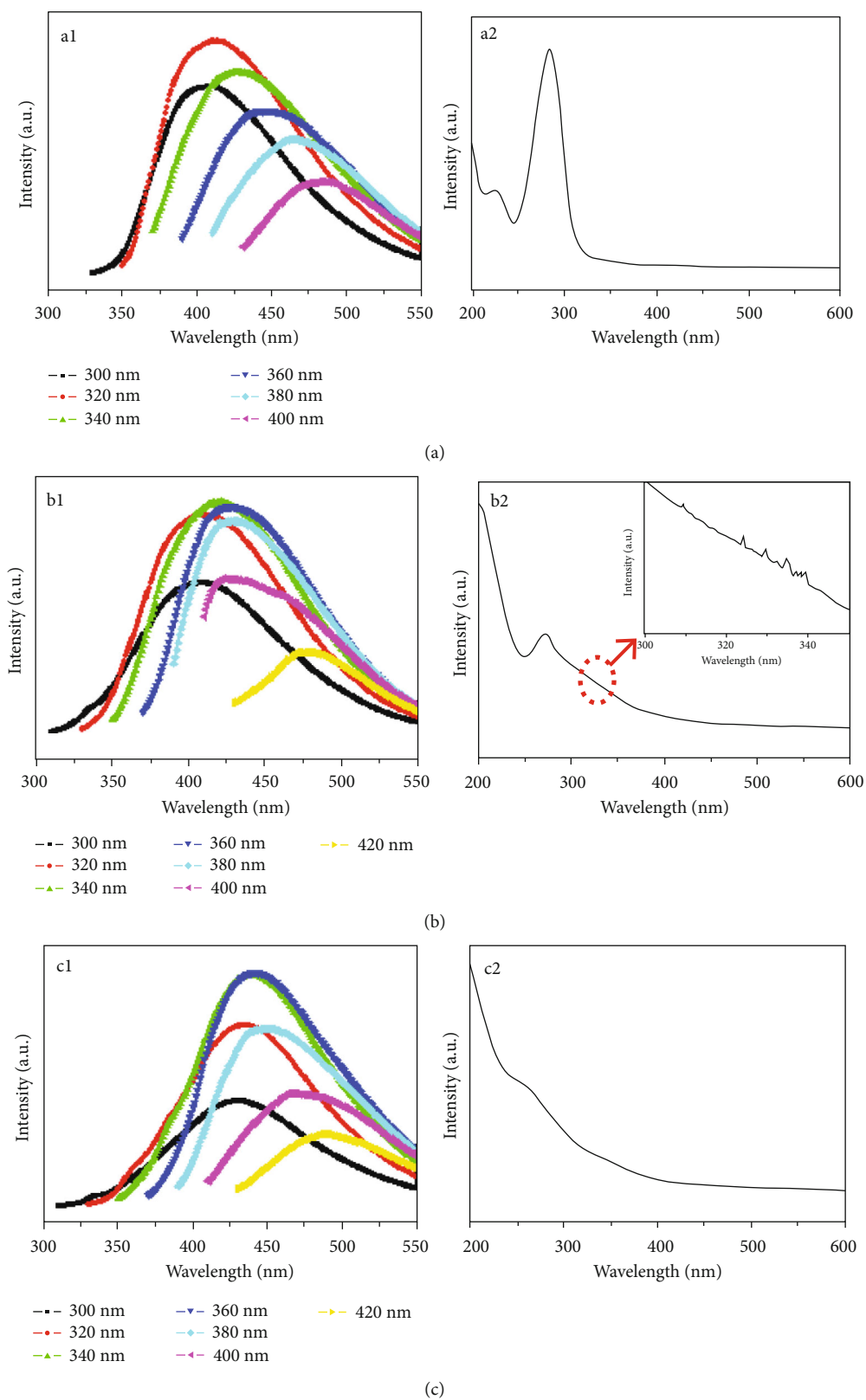
Figure 5: (a) The fluorescence spectra of UCQDs (a1), NCQDs (b1), and UCQDs-peel (c1), under the different excitation wavelengths. (b) The UV–vis absorption spectra of UCQDs (a2), NCQDs (b2), and UCQDs-peel (c2).
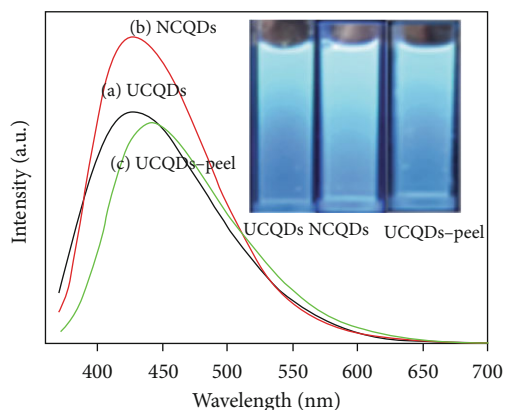
FIGURE 6: The fluorescence spectra of (a) UCQDs, (b) NCQDs and (c) UCQDs-peel with the same fixed concentration. The inset is the photos of solution of CQDs under the irradiation of 365 nm.

in the range of 4.74-8.20 nm with an average diameter of 6.34 nm and a range of 2.45~6.23 nm with maximum population at about 4.44 nm and 3.39 nm, respectively.

3.2. The Analysis of Surface Chemistry Compositions. To investigate the surface chemistry characteristics of the three kinds of CQDs from grapefruit, the prepared samples were characterized by FTIR spectroscopy. As shown in Figure 4, it can be seen that the similar absorption peaks were found in three prepared samples. And the absorption peaks at about $3675\,cm^{-1}$ and $1050\,cm^{-1}$ can be ascribed to the stretching vibration of carboxylic acid (-COOH) and hydroxyl group (O-H) [26]. The peaks at $2976\,cm^{-1}$ and $2900\,cm^{-1}$ corresponded to the vibration mode of C-H. The peaks observed at 1733, 1572, and $1388\,cm^{-1}$ corresponded to the stretching vibrations of the C=O, C=C, and C-N groups, respectively. Furthermore, three samples have similar IR bands within the range of $\sim1000\,cm^{-1}$ which are assigned to the stretching vibrations of C-H. In addition, the peak at $1250\,cm^{-1}$ is observed in UCQDs and UCQDs-peel assigned to armchair configuration, which appears at the edges of graphene layers being consistent with carbine and carbine structures at armchair sites [13]. And the presence at about 3173, 750, 1667, and $1448\,cm^{-1}$ in the NCQDs due to the stretching or bending vibration of the N-H, CONH, and C-N groups [27], which indicates the effective nitrogen doping into CQDs occurring from urea.

3.3. Fluorescence and UV–vis Absorption Spectra. The optical properties of three kinds of obtained samples were investigated by FL emission and UV–vis absorption spectra. Figures 5(a), 5(b), and 5(c) present CQDs, NCQDs, CQDs-1, respectively. It can be found that the three kinds of CQDs show the excitation-dependent emission spectral behavior with different maximum emission wavelengths when the excitation wavelength varied from 300 to 420 nm with an increment of 20 nm. The FL intensity increased gradually and then decreased, and the strong emission peaks were found at 411 nm (Figure 5 a1, ex: 320 nm), 418 nm (Figure 5 b1, ex: 340 nm), and 420 nm (Figure 5 c1, ex: 340 or 360 nm), respectively.

UV–vis absorption spectra of three kinds of CQDs exhibit different absorption bands due to different surface states. Two different absorption bands are found in Figure 5 a2 (for UCQDs), which are ascribed to a typical absorption of an aromatic system. The weak absorption peak at 225 nm can be attributed to the n-π * transition of C=C bonds. The strong peak at 283 nm is assigned to the π-π * transition of C=C bonds for aromatic sp^2 hybridisation (shown in Figure 5 a2) [28]. However, multiple absorption peaks were observed in Figure 5 b2 (for the NCQDs). The strong peak at 271 nm can be attributed to the transition of n-π * and π-π * with C=O bonds of carboxyl groups and aromatic sp^2 (C=C) domains, respectively [29]. And the absorption bands at about 308 nm, 324 nm, 329 nm, and 334 nm indicate that the surface of the synthesized NCQDS molecules has amide functions. In Figure 5 c2, the broad absorption band from 240 to 280 nm was observed which is contributed to the π-π * transition of C=C bonds for aromatic sp^2 hybridisation.

The fluorescence spectra of CQDs from different reactive materials are shown in Figure 6. It was found that CQDs from different reactive materials showed similar fluorescence properties and different fluorescence intensity, when the concentration of CQDs fixed the same. UCQDs and NCQDs had the same fluorescence properties and different fluorescence intensities. In contrast, NCQDs showed a strong luminous intensity being ascribed to N-atom doping in the CQDs, which corresponded to the optical properties of CQDs improved via the edge doping [30]. And the edge doping increased photoexited electron in the emission transition channel, thereby enhancing the radiation transition probability and the PL intensity [16]. In addition, UCQDs-peel exhibited a red-shifted PL emission in comparison to the UCQDs and NCQDs. According to the above FTIR analysis, three kinds of CQDs are hydrophilic due to the surface polar groups, which are highly dispersible in water, and the solution of CQDs exhibits strong light blue light under the irradiation of 365 nm xenon lamp (shown in the inset of Figure 6).

4. Conclusions

In summary, a green and facile synthesized method was presented to prepare NCQDs with enhanced luminescence intensity by grapefruit juice and urea under hydrothermal treatment. UCQDs, NCQDs, and UCQDs were successfully synthesized by using grapefruit juice, grapefruit juice, and urea and grapefruit peel as reactive materials, respectively. The analysis of structure, composition, and fluorescence properties indicates that nitrogen atom doping can enhance the fluorescence intensity due to the edge doping increasing photoexited electron in the emission transition channel, thereby enhancing the radiation transition probability and the PL intensity. In addition, UCQDs-peel exhibited a red-shifted PL emission in comparison to the UCQDs and NCQDs, which may be related to the size increase of CQDs.

Data Availability

The data used to support the findings of this study are available from the corresponding author upon request.

Conflicts of Interest

Acknowledgments

References

[1] M. J. Molaei, "The optical properties and solar energy conversion applications of carbon quantum dots: A review," *Solar Energy*, vol. 196, pp. 549–566, 2020.

[2] M. J. Molaei, "Principles, mechanisms, and application of carbon quantum dots in sensors: a review," *Analytical Methods*, vol. 12, no. 10, pp. 1266–1287, 2020.

[3] Q. Jia, Z. Zhao, K. Liang et al., "Recent advances and prospects of carbon dots in cancer nanotheranostics," *Materials Chemistry Frontiers*, vol. 4, no. 2, pp. 449–471, 2020.

[4] P. He, Y. Shi, T. Meng et al., "Recent advances in white light-emitting diodes of carbon quantum dots," *Nanoscale*, vol. 12, no. 8, pp. 4826–4832, 2020.

[5] J. Guo, H. Li, L. Ling et al., "Green synthesis of carbon dots toward anti-counterfeiting," *Acs Sustainable Chemistry & Engineering*, vol. 8, no. 3, pp. 1566–1572, 2019.

[6] S. P. Thota, S. M. Thota, S. S. Bhagavatham et al., "Facile one-pot hydrothermal synthesis of stable and biocompatible fluorescent carbon dots from lemon grass herb," *IET Nanobiotechnology*, vol. 12, no. 2, pp. 127–132, 2018.

[7] H. Wang, M. Zhang, Y. Ma et al., "Selective inactivation of Gram-negative bacteria by carbon dots derived from natural biomass: Artemisia argyi leaves," *Journal of Materials Chemistry B*, vol. 8, no. 13, pp. 2666–2672, 2020.

[8] M. Wang, Y. Wan, K. Zhang et al., "Green synthesis of carbon dots using the flowers of Osmanthus fragrans (Thunb.) Lour. as precursors: application in Fe^{3+} and ascorbic acid determination and cell imaging," *Analytical and Bioanalytical Chemistry*, vol. 411, no. 12, pp. 2715–2727, 2019.

[9] S. Wang, W. Sun, D.-s. Yang, and F. Yang, "Soybean-derived blue photoluminescent carbon dots," *Beilstein Journal of Nanotechnology*, vol. 11, pp. 606–619, 2020.

[10] R.-C. Wang, J.-T. Lu, and Y.-C. Lin, "High-performance nitrogen doped carbon quantum dots: facile green synthesis from waste paper and broadband photodetection by coupling with ZnO nanorods," *Journal of Alloys and Compounds*, vol. 813, article 152201, 2020.

[11] Z. Lai, X. Guo, Z. Cheng, G. Ruan, and F. Du, "Green synthesis of fluorescent carbon dots from cherry tomatoes for highly effective detection of trifluralin herbicide in soil samples," *Chemistryselect*, vol. 5, no. 6, pp. 1956–1960, 2020.

[12] M. Wen, Z. Qin, W. Wang et al., "A solvent-governed surface state strategy for rational synthesis of N and S co-doped carbon dots with multicolour fluorescence," *Molecular Physics*, pp. 1–11, 2020.

[13] D. López-Díaz, A. Solana, J. L. García-Fierro, M. D. Merchán, and M. M. Velázquez, "The role of the chemical composition on the photoluminescence properties of N-doped carbon nanoparticles," *Journal of Luminescence*, vol. 219, article 116954, 2020.

[14] X. Li, L. Yan, J. Si, Y. Xu, and X. Hou, "Control of the size and luminescence of carbon nanodots by adjusting ambient pressure in laser ablation process," *Journal of Applied Physics*, vol. 127, no. 8, article 083102, 2020.

[15] X. Zhang, M. Jiang, N. Niu et al., "Natural-Product-Derived Carbon Dots: From Natural Products to Functional Materials," *ChemSusChem*, vol. 11, no. 1, pp. 11–24, 2018.

[16] C. Hu, M. Li, J. Qiu, and Y.-P. Sun, "Design and fabrication of carbon dots for energy conversion and storage," *Chemical Society Reviews*, vol. 48, no. 8, pp. 2315–2337, 2019.

[17] S. J. Park, J. Y. Park, J. W. Chung, H. K. Yang, B. K. Moon, and S. S. Yi, "Color tunable carbon quantum dots from wasted paper by different solvents for anti-counterfeiting and fluorescent flexible film," *Chemical Engineering Journal*, vol. 383, article 123200, 2020.

[18] L. Jiang, H. Ding, S. Lu et al., "Photoactivated Fluorescence Enhancement in F,N-Doped Carbon Dots with Piezochromic Behavior," *Angewandte Chemie-International Edition*, vol. 59, no. 25, pp. 9986–9991, 2020.

[19] T. Geng, C. Liu, G. Xiao, S. Lu, and B. Zou, "Advances in the application of high pressure in carbon dots," *Materials Chemistry Frontiers*, vol. 3, no. 12, pp. 2617–2626, 2019.

[20] F. Huo, Z. Kang, M. Zhu et al., "Metal-triggered fluorescence enhancement of multicolor carbon dots in sensing and bioimaging," *Optical Materials*, vol. 94, pp. 363–370, 2019.

[21] Y. Wang, Y. Li, and Y. Xu, "Synthesis of mechanical responsive carbon dots with fluorescence *enhancement*," *Interface Science*, vol. 560, pp. 85–90, 2020.

[22] Q. Wang, S. Zhang, B. Wang et al., "Pressure-triggered aggregation-induced emission enhancement in red emissive amorphous carbon dots," *Nanoscale Horizons*, vol. 4, no. 5, pp. 1227–1231, 2019.

[23] Y. Xu, Y. Fan, L. Zhang, Q. Wang, H. Fu, and Y. She, "A novel enhanced fluorescence method based on multifunctional carbon dots for specific detection of Hg^{2+} in complex samples," *Spectrochimica Acta Part a-Molecular and Biomolecular Spectroscopy*, vol. 220, p. 117109, 2019.

[24] W.-K. Li, J.-T. Feng, and Z.-Q. Ma, "Nitrogen, sulfur, boron and flavonoid moiety co-incorporated carbon dots for sensitive fluorescence detection of pesticides," *Carbon*, vol. 161, pp. 685–693, 2020.

[25] D. Bouzas-Ramos, J. C. Canga, J. C. Mayo, R. M. Sainz, J. R. Encinar, and J. M. Costa-Fernandez, "Carbon quantum dots codoped with nitrogen and lanthanides for multimodal imaging," *Advanced Functional Materials*, vol. 29, no. 38, article 1903884, 2019.

[26] J. Singh, S. Kaur, J. Lee et al., "Highly fluorescent carbon dots derived from *Mangifera indica* leaves for selective detection of metal ions," *Science of the Total Environment*, vol. 720, article 137604, 2020.

[27] H. Qi, M. Teng, M. Liu et al., "Biomass-derived nitrogen-doped carbon quantum dots: highly selective fluorescent probe for detecting Fe3+ ions and tetracyclines," *Journal of Colloid and Interface Science*, vol. 539, pp. 332–341, 2019.

[28] V. Ramar, S. Moothattu, and K. Balasubramanian, "Metal free, sunlight and white light based photocatalysis using carbon

quantum dots from Citrus grandis: a green way to remove pollution," *Solar Energy*, vol. 169, pp. 120–127, 2018.

[29] T. Chatzimitakos, A. Kasouni, L. Sygellou, A. Avgeropoulos, A. Troganis, and C. Stalikas, "Two of a kind but different: Luminescent carbon quantum dots from *Citrus* peels for iron and tartrazine sensing and cell imaging," *Talanta*, vol. 175, pp. 305–312, 2017.

[30] N. Tejwan, S. K. Saha, and J. Das, "Multifaceted applications of green carbon dots synthesized from renewable sources," *Advances in Colloid and Interface Science*, vol. 275, article 102046, 2020.

Research Article

Jurkat T Cell Detectability and Toxicity Evaluation of Low-Temperature Synthesized Cadmium Quantum Dots

Ngoc Thuy Vo [iD],[1,2] **Thi Bich Vu,**[3,4] **Hong Tran Thi Diep,**[1,2] **Thien Le Khanh,**[1,2] **Hieu Tran Van,**[1,2] **Thanh Binh Nguyen,**[4] **and Quang Vinh Lam** [iD][1,2]

[1]*University of Science, Ho Chi Minh City 72711, Vietnam*
[2]*Vietnam National University, Ho Chi Minh City 71308, Vietnam*
[3]*Institute of Theoretical and Applied Research, Duy Tan University, Ha Noi 100000, Vietnam*
[4]*Institute of Physics, Vietnam Academy of Science and Technology, 10 Dao Tan, Ba Dinh, Ha Noi, Vietnam*

Correspondence should be addressed to Ngoc Thuy Vo; vtnthuy@hcmus.edu.vn

Early and highly accurate detection of diverse diseases is in urgent demand than ever, especially for cancers and infectious ones. Among possibilities, biosensing by utilizing conjugated nanoparticles is still a method of choice. However, the toxicity of quantum dots remains a big matter of concern in those biooriented applications. In this study, mercaptosuccinic acid-coated cadmium selenide quantum dots of approximately 2.3 nm were synthesized with a simple green method at low temperature and cost-saving chemicals. The influence of synthesis factors was investigated with different spectroscopic methods. The toxicity issue was evaluated on the NIH-3T3 cell line (ATCC® CRL-1658™) and an MTT assay, revealing a secure threshold of 20 μg/ml. Consequently, successful conjugation to the CD3 antibody including an A/G protein bridge was implemented and verified with fluorescent methods. Finally, Jurkat T cell detectability of conjugated CdSe was successfully validated with fluorescent microscopy. The CdSe-based products are accessible for future biosensing applications.

1. Introduction

For years, understanding of semiconducting quantum dots along with their unique properties of zero-dimensional structure has been extensively accumulated not only through diverse synthesis methods but also through novel applications [1–5]. Thanks to the primary advantages such as high stability, broad photoluminescence and absorption spectra, large Stoke shift, long lifetime, and an order of luminescent intensity higher than organic dyes and fluorescent protein counterparts [6, 7], quantum dots have been employed widely in biology especially in biomarking and biosensing [8–10].

A huge effort has been paid out on the fabrication and characterization of highly luminescent quantum dots derived from trioctylphosphine oxide- (TOPO-) or trioctylphosphine- (TOP-) mediated routes of high temperatures and costly chemicals. However, such quantum dots exhibited low dispersion in water and an inability to be directly applied in biology without surface functionalization [11–13]. Recent reports have focused on fabricating highly stable CdSe quantum dots in water with surfactants comprising thiol groups [14–17]. These nanoparticles could be applied straightly into bioapplications on the one hand, but low luminescence intensity due to dislocation or surface defects was a big drawback. Till now, novel synthesis methods have continuously been introduced to achieve nanoparticles of high quality and high luminescence as well as time and cost saving [18]. Following the trend, this work was aimed at synthesizing mercaptosuccinic acid- (MSA-) coated quantum dots of high quality, high luminescence, and high biocompatibility from inexpensive chemicals without metal-organic precursors. Effects of temperature, reaction time, and pH values on optical properties and structure were under investigation with UV-visible absorption, photoluminescence (PL), Fourier transform infrared spectroscopy, X-ray diffraction (XRD), and transmission electron microscopy (TEM). Experimentally, quantum

dots cause a greater effect of toxicity compared to bulky counterparts at the same mass dose [19–21]. Potential toxicity and hazardous adverse effects of bare CdSe quantum dots on biological samples have always posed a concern much greater than the core/shell CdSe/ZnS counterparts. In practice, toxicity evaluation of CdSe without a protective shell layer is a crucial step toward basic knowledge and further bioapplications. We evaluated the quantum dot toxicity by using the NIH-3T3 cell line (ATCC® CRL-1658™) and an MTT assay to determine a nontoxic threshold of high cell viability. A cadmium selenide quantum dot concentration of 20 μg/ml was found to be the safe level from which cells presented a great chance for survival (97.4% on average). Finally, for the detection of Jurkat T cells, conjugation of the CD3 antibody to MSA-capped CdSe quantum dots was implemented. In this process, the A/G protein played a role as a vital connector to enhance CD3 antibody-CdSe quantum dot association. Successful conjugation of the A/G protein and the CD3 antibody was verified with photoluminescence and time-resolved fluorescence characterizations. The final products are eminently promising and relevant to further development.

2. Experiment

2.1. Synthesis of MSA-Coated CdSe Quantum Dots. All chemicals in MSA-capped CdSe quantum dot synthesis were of analytical grade and brought into use without further purification: mercaptosuccinic acid (MSA), cadmium acetate dehydrate (Cd(CH$_3$CO$_2$)$_2$·2H$_2$O), sodium selenite pentahydrate (Na$_2$SeO$_3$·5H$_2$O), sodium borohydride (NaBH$_4$), sodium hydroxide (NaOH, 99%), methanol, toluene, and phosphate buffer saline solution (PBS, pH 7.0).

Initially, 1.53 mmol of Cd(CH$_3$CO$_2$)$_2$·2H$_2$O, 1.85 mmol of MSA, and 50 ml of distilled water were added into a three-neck flask to produce a Cd^{2+} precursor. The mixture was stirred in a nitrogen atmosphere until MSA was completely dissolved. Nitrogen gas was introduced to eliminate oxygen and the resulting acetic acid. To adjust pH, NaOH was gradually dropped to reach the expected value (6.0-11.5). For the Se^{2-} precursor, 2.64 mmol of NaBH$_4$, 1.34 mmol of Na$_2$SeO$_3$·5H$_2$O, and 5 ml of water were mixed up for 15 minutes. We rapidly injected the Se^{2-} precursor into the Cd^{2+} solution at room temperature. The mixture was then stirred for 30 minutes at 600 rpm. The solution was then heated up to three different reaction temperatures (90°, 95°, or 100°C) without stirring. After some time, toluene was injected to rapidly cool down the solution and to intentionally stop the development of particles. The as-synthesized products were finally dispersed in PBS 7.0 buffer solution for long-time preservation. A simple method of preparation, common chemicals, and reasonably low synthesis temperature are the three big advantages of this method.

2.2. Toxicity Evaluation of Quantum Dots. The toxicity of quantum dots was analyzed using the NIH-3T3 cell line (ATCC® CRL-1658™) and the MTT assay. NIH-3T3 cells were grown in DMEM-10 medium (HiMedia) supplemented with 10% fetal bovine serum (FBS) and antibiotics (Sigma).

Cells were seeded onto a 96-well plate (5×10^3 cells per well) in 100 μl DMEM-10 and incubated at 37°C in 5% CO$_2$ for 24 hours. After this time, cells were washed, supplemented with 100 μl of DMEM-10 containing quantum dots with different concentrations of 2×10^3, 2×10^2, 2×10^1, and 2×10^0 μg/ml, and incubated at 37°C in 5% CO$_2$ for 48 hours. Then, 5 μg/ml of MTT (Sigma) was added at a ratio 1/10 (v/v), cells were incubated for 3 hours, and optical density (OD) was measured at a wavelength of 550 nm (Multiskan Ascent). The results were normalized to respective control samples.

2.3. CD3 Antibody Conjugation to Quantum Dots. For conjugation of the CD3 antibody to MSA-capped CdSe quantum dots, the A/G protein was employed as an essential bridge to firmly enhance antibody-quantum dot connection efficiency. For this reason, a higher antibody-antigen interaction performance could be achieved later. Initially, acid-coated quantum dots were shaken in 5% BSA at 10°C for two hours to ensure that there was no direct interaction between quantum dots and cells through nonspecific bonds. Consequently, we supplied antibodies to Jurkat T cells [10, 22] at a weight ratio of 3 : 1 over the formerly delivered A/G protein. Reaction took place in an antibody incubation solution (Tris-base 50 mM, NaCl 150 mM, pH 8.2) which was shaken at 10°C for 2.5 hours. Finally, the solution went through centrifugation to collect the conjugated quantum dots.

2.4. Instrumental Characterization. Optical properties of nanoparticles were investigated with different spectroscopic measurements such as UV-visible absorption (PB-10 spectrophotometer, Taiwan), photoluminescence (PL, Jobin Yvon Spex Fluorolog 3, Horiba, Japan) of 325 nm excitation wavelength, and Fourier transform infrared spectrometer (FTIR, Tensor 27, Bruker, Germany). The crystal structure and morphology of quantum dots were studied with X-ray diffraction (D8 ADVANCE XRD, Bruker, Germany) taken with an accelerated voltage of 40 kV, a current intensity of 30 mA, a Cu-Kα wavelength of 1.5406 Angstroms, and transmission electron microscopy (TEM, JEM-1400, JEOL, Japan).

3. Results and Discussion

Synthesis temperature, reaction time, and pH values revealed a significant impact on the optical property of CdSe dots. A brief discussion about these influences will be given, and characterization of the best synthesis condition (temperature 100°C, reaction time 4 hours, and pH 11.5) will be provided.

As temperature increased from 90° to 95° and 100°C, UV-visible absorption peaks shifted accordingly (from 470.5 to 489 and 495.5 nm) due to a quantum confinement effect. According to Peng's equation [6], the average sizes of CdSe dots varied from 2.1 nm (90°C) to 2.2 nm (95°C) and 2.3 nm (100°C).

The reaction time effect on particle size distribution was systematically studied (from 1, 2, and 3 to 4 hours). While synthesis temperature was maintained at 100°C, four-hour synthesis exhibited the best absorption and photoluminescent spectra of high, sharp peaks and zero-approaching baselines.

In the CdSe synthesis procedure, Se^{2-} ions were easily oxidized during precursor preparation. To hinder that process, $NaBH_4$ was used to ensure that all SeO_3^{2-} would be transformed into Se^{2-} as described in Dong et al. ([14]):

$$SeO_3^{2-} + BH_4^- \longrightarrow Se^{2-} + B(OH)_3 + H_2O \qquad (1)$$
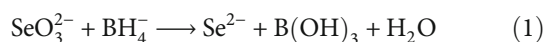
On the other hand, an excessive amount of $NaBH_4$ was easily hydrolyzed as well as oxidized; it then helped create an inert environment and prevent Se^{2-} ions from oxidation.

$$BH_4^- + H_2O \longrightarrow B(OH)_3 + OH^- + H_2 \qquad (2)$$

$$BH_4^- + O_2 \longrightarrow B(OH)_3 + H_2O \qquad (3)$$
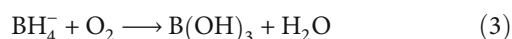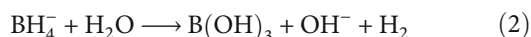
From (1), (2), and (3), it could be expected that a considerable amount of $B(OH)_3$ and OH^- was generated. This vigorously affected the pH value of the solution. To preserve sufficient growth conditions for CdSe quantum dots, pH values had to be adjusted subsequently from 7 to 11.5. Absorption peaks shifted to a longer wavelength when pH values increased. This could be explained by the increase in the dot growth rate when pH values increased in the same synthesis condition including time, temperature, and chemical ratio.

Luminescence intensity was likewise affected as pH values changed. CdSe quantum dot quality presented better improvement in higher pH environments. It could be justified as in higher pH values, thiol groups in MSA could efficiently form more complexes with Cd^{2-} ions. This in turn helped to enhance luminescence intensity by suppressing the surface traps of quantum dots [14, 15, 18].

3.1. Structure Investigation. The X-ray diffraction method was employed to study the structure of CdSe quantum dots (Figure 1). Three typical peaks at 2-theta 25.46°, 44.48°, and 49.91° demonstrated the zincblende structure of CdSe quantum dots, relating to lattice faces of (111), (220), and (311).

Existence of MSA as a capping layer of CdSe quantum dots was successfully validated by two noteworthy signals in FTIR spectra (Figure 2): an absorption band around $1639 \, cm^{-1}$ corresponding to vibration bonding C=O in both MSA and CdSe-MSA quantum dots and a peak at around $2571 \, cm^{-1}$ relating to S-H bonding, which disappeared in the CdSe-MSA case. These helped confirm MSA-CdSe bonding through the thiol (–SH) groups located on the one side of the acidic molecular structure. With two carboxyl groups facing out, the CdSe-MSA quantum dots were highly ready for further conjugation to functional biogroups. Ultimately, a broad absorption band at around $3303 \, cm^{-1}$ of O-H bonding ensured great hydrophilicity of coated CdSe dots.

A transmission electron image of MSA-coated CdSe quantum dots (synthesis temperature 100°C, reaction time 4 hours, and pH 11.5) was taken as shown in Figure 3. Fabricated particles presented a spherical shape with good size homogeneity of approximately 2.3 nm.

We plotted in Figure 4 both the absorption and photoluminescence spectra of a sample optimally synthesized at
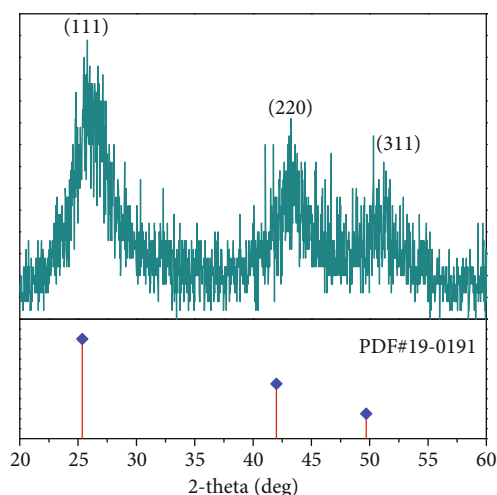

FIGURE 1: XRD pattern of CdSe quantum dots in a zincblende structure (synthesis temperature 100°C, reaction time 4 hours, and pH 11.5). Three peaks at 25.46°, 44.48°, and 49.9° related to the (111), (220), and (311) lattice direction.
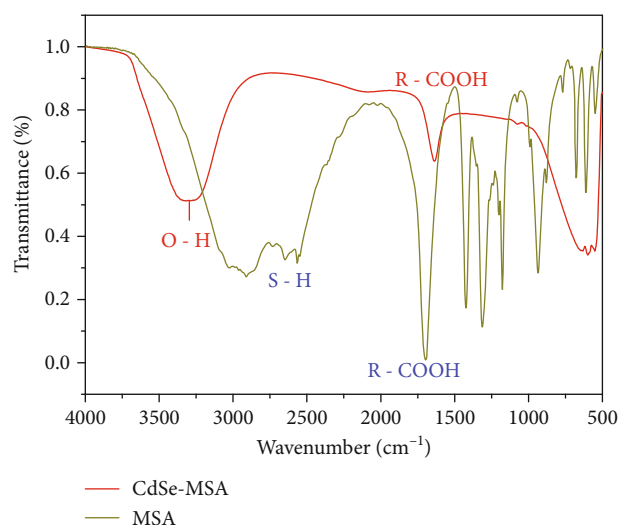

FIGURE 2: FTIR spectra of MSA (black) and MSA-capped CdSe quantum dots (red).

100°C, pH 11.5, and a reaction time of 4 hours and finally dispersed in PBS 7.0 buffer solution.

The photoluminescence spectrum (red line) presented a high, sharp peak of narrow full width at half maximum. Both sides of the peak approached near zero values. It certified that a 4-hour reaction was optimal for the growth of quantum dots and MSA not only enhanced the luminescence intensity but also helped to passivate surface traps.

A small difference of approximately 0.096 eV existed between absorption and luminescence peaks. Such a tiny deviation verified the high quality of the synthesized quantum dots in which surface traps were inhibited and energy transfer to lattice vibration was limited.

3.2. Toxicity Evaluation of Quantum Dots. According to ISO 10993-5 tests for *in vitro* cytotoxicity, reduction of cell
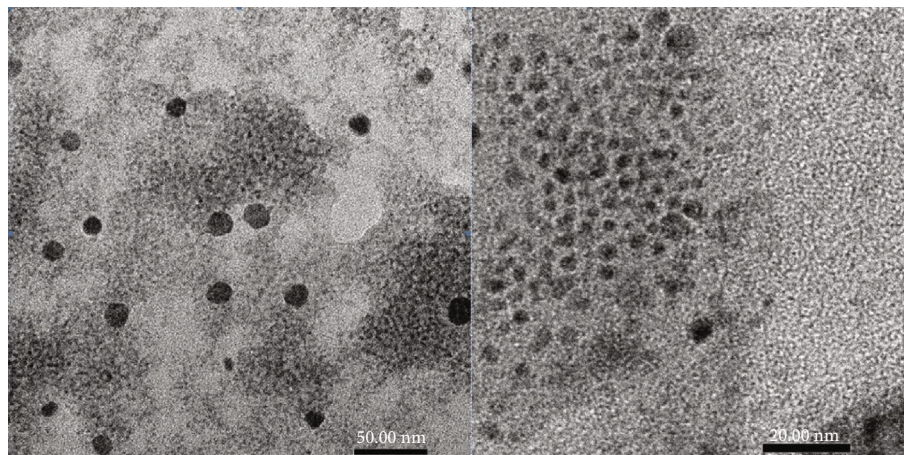
FIGURE 3: TEM image of MSA-capped CdSe quantum dots at 100°C for 4 h. Uniform sphere-shaped particles of 2.3 nm, in the majority.

FIGURE 4: UV-visible absorption (blue) and photoluminescence spectra (red) of CdSe quantum dots optimally synthesized at 100°C, pH 11.5, and a reaction time of 4 hours and dispersed in PBS 7.0 buffer solution.

FIGURE 5: Viability of NIH-3T3 cells exposed to various concentrations of quantum dots. Black-filled bar: naked quantum dots; grey-filled bars: MSA-capped quantum dots.

(a)

(b)

(c)

(d)

FIGURE 6: Morphology of NIH-3T3 cells exposed to various quantum dot concentrations: no exposure (a), 20 μg/ml (b), 200 μg/ml (c), and 2000 μg/ml (d).

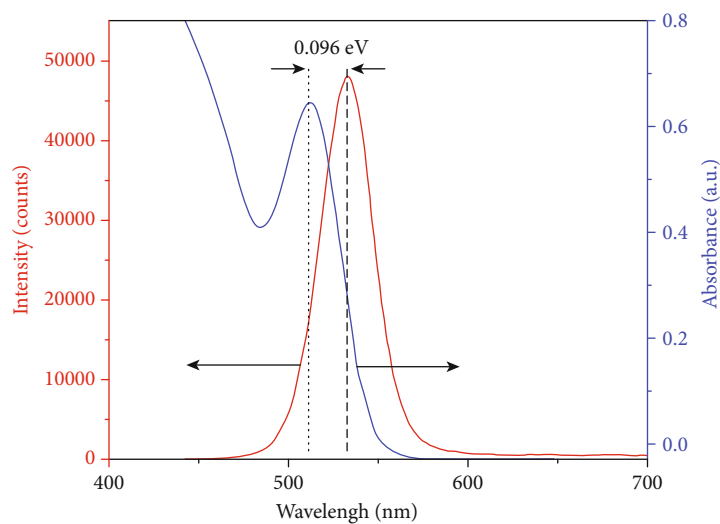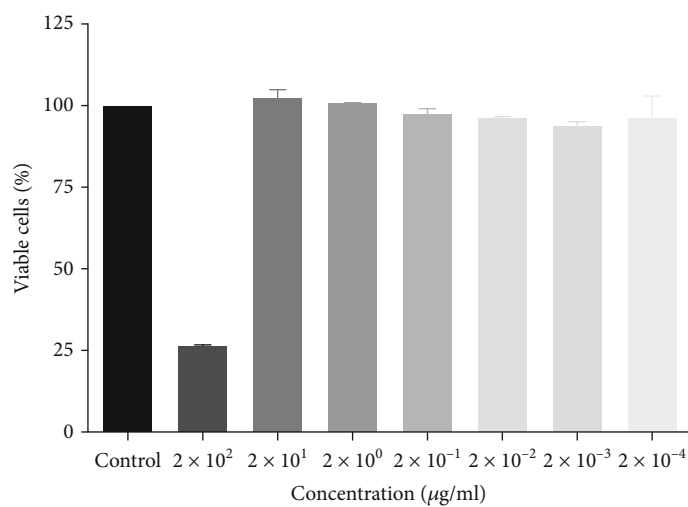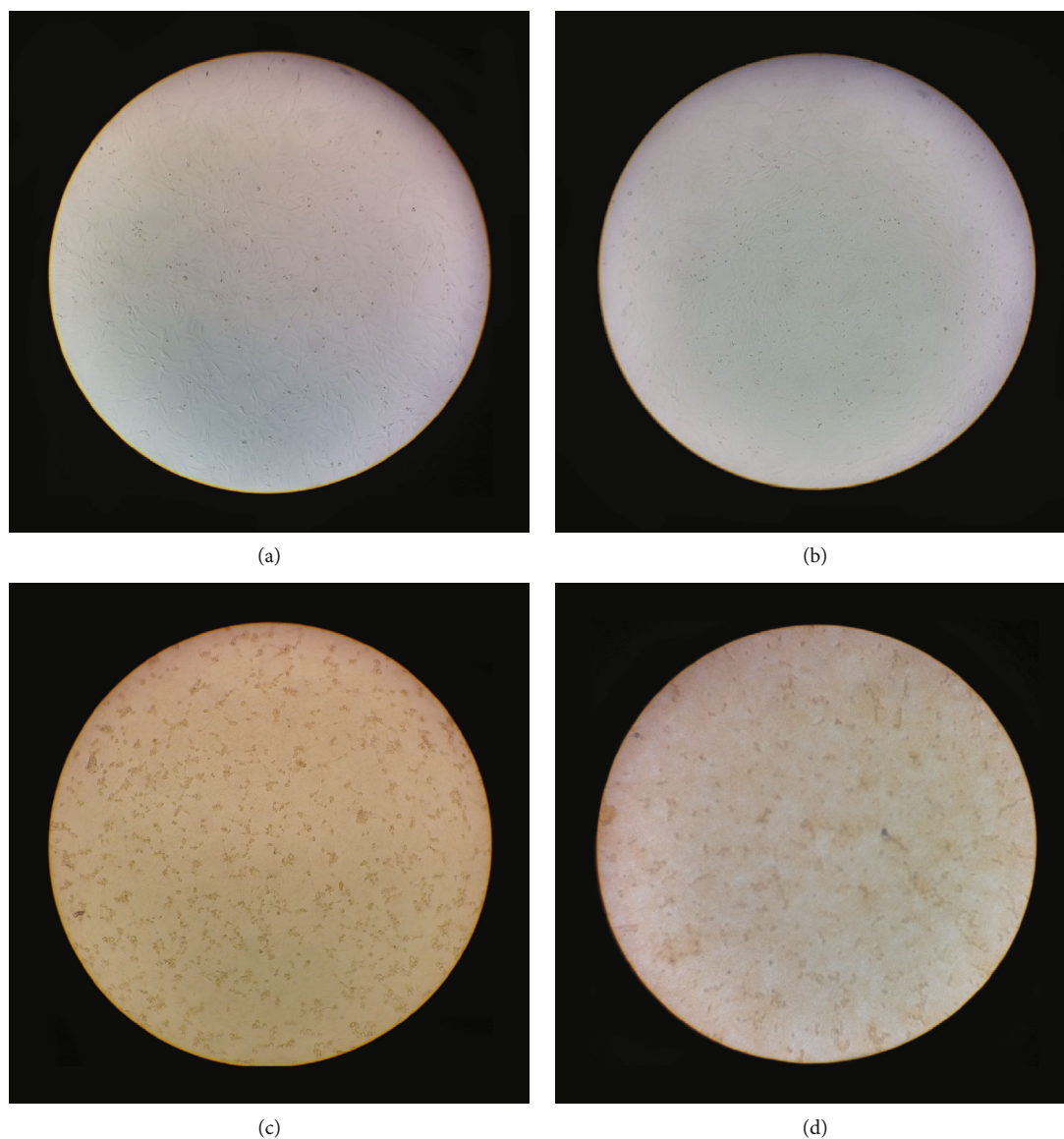viability by more than 30% is considered a cytotoxic effect [19]. Figure 5 shows the viability of NIH-3T3 cells exposed to various concentrations of quantum dots.

In accordance with a cytotoxic assay, morphological observation showed the same tendency, as shown in Figure 6. With cells exposed to and incubated in 2×10^2 μg/ml CdSe-MSA or higher, the vitality ratio dropped down to 25.9%, lower than the safety threshold. Cells became smaller and rounder and turned apoptotic. Previous studies show that Cd^{2+} ions are released from the surface of cadmium-based quantum dots. Cadmium is known as a toxic element that induces several adverse effects such as the induction of oxidative stress, mitochondrial dysfunction, apoptosis, and the disruption of intracellular calcium signaling, which leads to their cytotoxic effects [20, 21]. However, there was no obvious morphological change in the presence of quantum dots

covered by MSA at the concentrations from 2×10^1 μg/ml to 2×10^{-4} μg/ml; cell vitality ratios remained at a remarkably high level of 97.4% on average. Consequently, at a concentration of 20 μg/ml or less, cells had a great chance for survival. Taken together, we conclude that the highest concentrations of quantum dots that are nontoxic to the NIH-3T3 cell line was at 20 μg/ml.

3.3. Bioconjugation of the CD3 Antibody to MSA-Capped CdSe. Successfully conjugated samples were characterized by photoluminescent and time-resolved fluorescent spectroscopy.

The photoluminescent spectra of MSA-coated CdSe (sample A), A/G protein-MSA-coated CdSe (sample B), and CD3 antibody-A/G protein-MSA-coated CdSe (sample C) are depicted in Figure 7. Interestingly, after connecting with a bridging protein and an antibody, sample
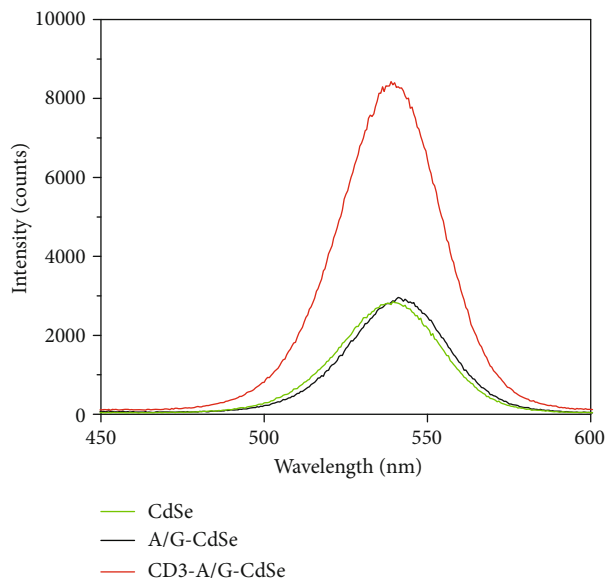
FIGURE 7: Photoluminescence spectra of MSA-coated CdSe (green), A/G protein-MSA-coated CdSe (black), and CD3 antibody-A/G protein-MSA-coated CdSe (red).

FIGURE 9: Jurkat T cell labeling evaluation of CD3 antibody-A/G protein-CdSe under fluorescent microscopy.

From time-resolved fluorescence decay curves (Figure 8), the fluorescence lifetime of these samples has been determined by fitting the decay curves with a triexponential function:

$$I(t) = A_1 \cdot \exp\left(-\frac{t}{\tau_1}\right) + A_2 \cdot \exp\left(-\frac{t}{\tau_2}\right) + A_3 \cdot \exp\left(-\frac{t}{\tau_3}\right),$$

$$(4)$$

where τ_1, τ_2, and τ_3 are the first, second, and third components of lifetimes and A_1, A_2, and A_3 are the corresponding relative weights of these components. The average fluorescence lifetimes for the decay curves were calculated from the decay times and the relative contribution of the components using the following equation:

$$\tau_{av} = \tau_1 . A_1 + \tau_2 . A_2 + \tau_3 . A_3 \qquad (5)$$

The fluorescence showed a triexponential decay with average lifetimes of 11.9, 11.9, and 9.1 nanoseconds for MSA-coated CdSe, A/G protein-MSA-coated CdSe, and CD3 antibody-A/G protein-MSA-coated CdSe, respectively.

A shorter radiative lifetime and low nonradiative recombination of carriers in sample C also helped to explain the strong luminescence compared with samples A and B (Figure 7). This is quite convenient and suitable for time-saving detection under fluorescent microscopy.

3.4. Jurkat T Cell Labeling Assessment. In addition to other spectroscopic or microscopic methods, confocal laser scanning microscopy has been considered an effective tool to verify the conjugation of bioagents on quantum dots [8, 10] and
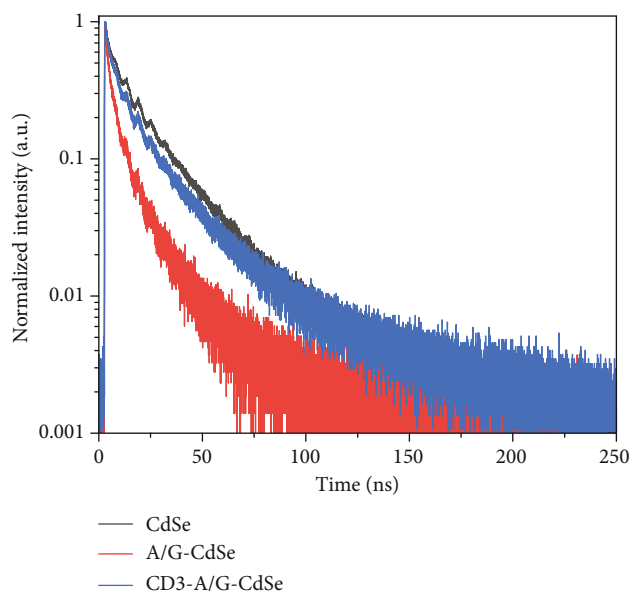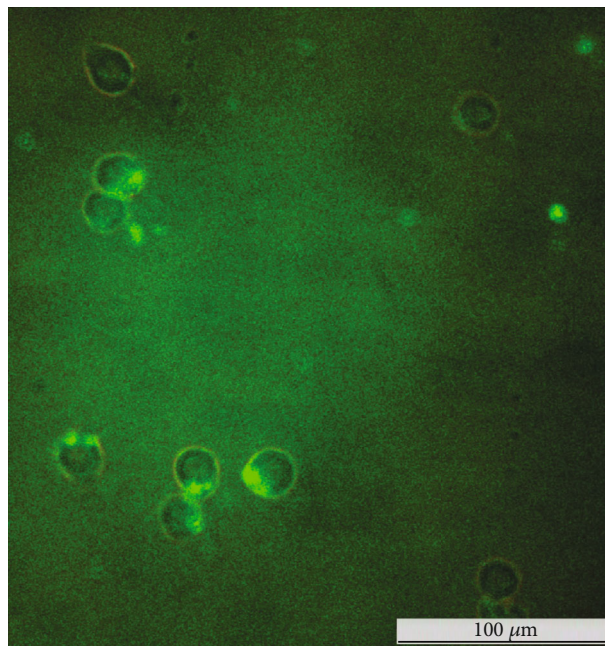

FIGURE 8: Photoluminescence decay curves of MSA-coated CdSe (black), A/G protein-MSA-coated CdSe (red), and CD3 antibody-A/G protein-MSA-coated CdSe (blue). Excited wavelength of 405 nm.

C exhibited a much higher peak than samples A and B. Such big improvement could probably be explained by lower dangling bonds or traps at the quantum dot surfaces, which might lead to the enhancement of radiative recombination rate and reduction of carrier lifetime. To verify such postulation, the radiative lifetime of the three samples was characterized through time-resolved fluorescence measurements.

the successful applications of nanoparticles in the biomedical field [9, 23–26].

To evaluate cell detection capability, CD3-A/G-CdSe was mixed at a volume ratio of 1 : 3 with Jurkat T cells preserved in RPMI 1640 solution. The mixture was delivered into several microcentrifuge tubes and moderately shaken for 30 minutes. Thereafter, those tubes went through centrifugation of 1500 rounds per minute for 5 minutes to eliminate unnecessary supernatants. The final product was characterized by fluorescent microscopy as shown in Figure 9. High fluorescent intensity could be observed on the membrane of Jurkat T cells where the quantum dots were located. This led to two solid conclusions: (1) good coupling between CD3 antibody-A/G protein-CdSe and cell antigen and (2) substantial bonding between quantum dots and cells.

4. Conclusion

In summary, we successfully synthesized MSA-coated CdSe by a simple green method at low temperature with cost-saving chemicals. The influence of reaction time, temperature, and pH values on optical property was spectroscopically characterized. Uniformly distributed 2.3 nm acid-coated quantum dots of high quality, high luminescence, and high biocompatibility were produced at 100°C, a pH value of 11.5, and a four-hour reaction. The toxicity of MSA-capped CdSe quantum dots was evaluated using the NIH-3T3 cell line (ATCC® CRL-1658™) and the MTT assay resulting in a secure threshold of 20 μg/ml. The CD3 antibody was successfully conjugated to the MSA-capped CdSe with the assistance of the A/G protein. Photoluminescence and time-resolved fluorescence were employed for verification. Lifetimes were found to decrease from 11.9 nanoseconds for MSA-coated CdSe and A/G protein-MSA-coated CdSe down to 9.1 ns for the CD3 antibody-A/G protein-MSA-coated CdSe, respectively. The final conjugated CdSe quantum dots were mixed with Jurkat T cells to evaluate detection ability. Fluorescent microscopic results evidently exhibited great coupling of the CD3 antibody and antigens and validated the high possibility of CdSe-based biosensors. The achieved products are ready for the coming steps of development.

Data Availability

The data used to support the findings of this study are included within the article and available from the corresponding authors upon request.

Conflicts of Interest

The authors declare that they have no conflict of interest.

Acknowledgments

References

[1] V. Biju, T. Itoh, and M. Ishikawa, "Delivering quantum dots to cells: bioconjugated quantum dots for targeted and nonspecific extracellular and intracellular imaging," *Chemical Society Reviews*, vol. 39, no. 8, pp. 3031–3056, 2010.

[2] J. F. Callan and R. C. Mulrooney, "Luminescent detection of Cu(II) ions in aqueous solution using CdSe and CdSe-ZnS quantum dots functionalised with mercaptosuccinic acid," *physica status solidi (c)*, vol. 6, no. 4, pp. 920–923, 2009.

[3] S. Chen, X. Zhang, Q. Zhang et al., "CdSe quantum dots decorated by mercaptosuccinic acid as fluorescence probe for Cu^{2+}," *Journal of Luminescence*, vol. 131, no. 5, pp. 947–951, 2011.

[4] W. E. Mahmoud, "Functionalized ME-capped CdSe quantum dots based luminescence probe for detection of Ba^{2+} ions," *Sensors and Actuators B: Chemical*, vol. 164, no. 1, pp. 76–81, 2012.

[5] Z. Zhelev, H. Ohba, R. Bakalova et al., "Fabrication of quantum dot–lectin conjugates as novel fluorescent probes for microscopic and flow cytometric identification of leukemia cells from normal lymphocytes," *Chemical Communications*, vol. 15, no. 15, pp. 1980–1982, 2005.

[6] C. Cai, H. Cheng, Y. Wang, and H. Bao, "Mercaptosuccinic acid modified CdTe quantum dots as a selective fluorescence sensor for A^{g+} determination in aqueous solutions," *RSC Advances*, vol. 4, no. 103, pp. 59157–59163, 2014.

[7] M. S. Hosseini and A. Pirouz, "Study of fluorescence quenching of mercaptosuccinic acid-capped CdS quantum dots in the presence of some heavy metal ions and its application to Hg(II) ion determination," *Luminescence*, vol. 29, no. 7, pp. 798–804, 2014.

[8] S. Dwarakanath, J. G. Bruno, A. Shastry et al., "Quantum dot-antibody and aptamer conjugates shift fluorescence upon binding bacteria," *Biochemical and Biophysical Research Communications*, vol. 325, no. 3, pp. 739–743, 2004.

[9] G. Giraud, H. Schulze, T. Bachmann et al., "Fluorescence lifetime Imaging of Quantum dot labeled DNA microarrays," *International Journal of Molecular Sciences*, vol. 10, no. 4, pp. 1930–1941, 2009.

[10] H. Udaka, T. Fukuda, N. Kamata, and M. Suzuki, "Evaluation of CdSe/ZnS quantum dot–half anti CD3 antibody–conjugate using confocal laser scanning microscopy," *Molecular Crystals and Liquid Crystals*, vol. 653, no. 1, pp. 177–181, 2017.

[11] S. A. Rahman, N. Ariffin, N. A. Yusof et al., "Synthesis and surface modification of biocompatible water soluble core-shell quantum dots," *Advanced Materials Research*, vol. 879, pp. 184–190, 2014.

[12] S. Rosenthal, J. Mcbride, S. Pennycook, and L. Feldman, "Synthesis, surface studies, composition and structural characterization of CdSe, core/shell and biologically active nanocrystals," *Surface Science Reports*, vol. 62, no. 4, pp. 111–157, 2007.

[13] R. A. Sperling and W. J. Parak, "Surface modification, functionalization and bioconjugation of colloidal inorganic nanoparticles," *Philosophical Transactions of the Royal Society A: Mathematical, Physical and Engineering Sciences*, vol. 368, no. 1915, pp. 1333–1383, 2010.

[14] M. Dong, J. Xu, S. Liu, Y. Zhou, and C. Huang, "Synthesis of highly luminescent mercaptosuccinic acid-coated CdSe nanocrystals under atmospheric conditions," *Luminescence*, vol. 29, no. 7, pp. 818–823, 2014.

[15] S. Li, H. Zhao, and D. Tian, "Aqueous synthesis of highly monodispersed thiol-capped CdSe quantum dots based on the electrochemical method," *Materials Science in Semiconductor Processing*, vol. 16, no. 1, pp. 149–153, 2013.

[16] J. T. Siy, E. M. Brauser, and M. H. Bartl, "Low-temperature synthesis of CdSe nanocrystal quantum dots," *Chemical Communications*, vol. 47, no. 1, pp. 364–366, 2011.

[17] Y. Wang, S. Liu, H. Pan, K. Yang, and L. Zhou, "Synthesis of high-quality CdSe quantum dots in aqueous solution," *Micro & Nano Letters*, vol. 7, no. 9, pp. 889–891, 2012.

[18] E. Ying, D. Li, S. Guo, S. Dong, and J. Wang, "Synthesis and bio-imaging application of highly luminescent mercaptosuccinic acid-coated CdTe nanocrystals," *PLoS One*, vol. 3, no. 5, p. e2222, 2008.

[19] ISO, "ISO 10993-5:2009 Biological evaluation of medical devices—part 5: tests for in vitro cytotoxicity," 2009, https://www.iso.org/standard/36406.html.

[20] C. Kirchner, T. Liedl, S. Kudera et al., "Cytotoxicity of colloidal CdSe and CdSe/ZnS nanoparticles," *Nano Letters*, vol. 5, no. 2, pp. 331–338, 2005.

[21] L. Peng, M. He, B. Chen et al., "Cellular uptake, elimination and toxicity of CdSe/ZnS quantum dots in HepG2 cells," *Biomaterials*, vol. 34, no. 37, pp. 9545–9558, 2013.

[22] P. Humeniuk, S. Geiselhart, C. Battin et al., "Generation of a Jurkat-based fluorescent reporter cell line to evaluate lipid antigen interaction with the human INKT cell receptor," *Scientific Reports*, vol. 9, no. 1, p. 7426, 2019.

[23] B. H. Lee, S. Suresh, and A. Ekpenyong, "Fluorescence intensity modulation of CdSe/ZnS quantum dots assesses reactive oxygen species during chemotherapy and radiotherapy for cancer cells," *Journal of Biophotonics*, vol. 12, no. 2, p. e201800172, 2018.

[24] M. Röding, S. J. Bradley, M. Nydén, and T. Nann, "Fluorescence lifetime analysis of graphene quantum dots," *The Journal of Physical Chemistry C*, vol. 118, no. 51, pp. 30282–30290, 2014.

[25] B. Zhang, C. Yang, Y. Gao et al., "Mechanisms of fluorescence decays of colloidal CdSe–CdS/ZnS quantum dots unraveled by time-resolved fluorescence measurement," *Physical Chemistry Chemical Physics*, vol. 17, no. 41, pp. 27588–27595, 2015.

[26] B. Zhang, C. Yang, Y. Gao et al., "Engineering quantum dots with different emission wavelengths and specific fluorescence lifetimes for spectrally and temporally multiplexed imaging of cells," *Nanotheranostics*, vol. 1, no. 1, pp. 131–140, 2017.

Research Article

Efficient All-Inorganic CsPbBr$_3$ Perovskite Solar Cells by Using CdS/CdSe/CdS Quantum Dots as Intermediate Layers

Shibing Zou and Feng Li [ID]

Engineering Laboratory for Optoelectronics Testing Technology, Nanchang Hangkong University, Nanchang 330063, China

Correspondence should be addressed to Feng Li; lifengnchu@163.com

Highly efficient all-inorganic perovskite solar cells require a fast charge transfer from CsPbBr$_3$ to TiO$_2$ to reduce the recombination from trap states. Herein, we insert a CdS/CdSe/CdS quantum dot (QD) layer between the TiO$_2$ and CsPbBr$_3$ layers to fabricate all-inorganic perovskite solar cells. By tuning the thicknesses of the CdSe layer of CdS/CdSe/CdS QDs, the conduction band (CB) levels can be adjusted to -3.72~-3.87 eV. After inserting the QD intermediate layer, the energy offset between the CB of TiO$_2$ and CsPbBr$_3$ is reduced, thus leading to a charge transfer rate boost from 0.040×10^9 to 0.059×10^9 s^{-1}. The power conversion efficiency (PCE) of the solar cell with QD intermediate layer achieves 8.64%, which is 20% higher than its counterpart without QDs.

1. Introduction

Hybrid organic-inorganic lead halide perovskite solar cells (PSCs) are promising candidates for commercialization, owing to their extremely high power conversion efficiency (PCE over 22%) and low fabrication cost. Despite recent rapid progress in developing the novel perovskite materials or optimizing the structure of the hybrid PSCs, the unsatisfactory long-term stability of the PSCs and the high cost of the hole-transporting materials hinder their commercialization [1–3]. All-inorganic PSCs are regarded as one of the most hopeful platforms to tackle this issue [4]. As light absorbers, inorganic perovskites such as CsPbX_3 (X=I, Br) have high charge-carrier mobility, which is similar to hybrid perovskites [5–7]. Moreover, inorganic lead halides are capable of against humidity and heat, which guarantee their long stability [4, 8–10]. Besides, the light-induced halide segregation that commonly happens in hybrid perovskites does not occur in such all-inorganic PSCs because ions need to overcome higher energy barrier to migrate compared with hybrid ones. Therefore, growing efforts are devoted to developing all-inorganic PSCs, aiming at resolving the challenging faced by hybrid ones.

Hodes et al. first used CsPbBr$_3$ as the light absorber with a typical device structure of FTO/c-TiO$_2$/m-TiO$_2$/CsPbBr$_3$/HTM/Au, achieving a PCE of 5.95% and an open-circuit voltage (V_{oc}) of 1.28 V [11]. These parameters are comparable to those MA-containing hybrid PSCs. Later, Liu and his coworkers fabricated an all-inorganic PSC with architecture of FTO/cTiO$_2$/m-TiO$_2$/CsPbBr$_3$/carbon in ambient environment without humidity control, reaching a PCE of 6.7% and good tolerance in humid air and extreme temperatures [5]. Tang's group further boosted the PCEs of CsPbBr$_3$ all-inorganic PSCs from 6.7% to 10.6% by using interfacial or compositional engineering [12–14]. Despite these achievements, the charge-carrier trap states within the CsPbBr$_3$ film and the interface still impede the further improvements of the device performances [13, 15]. Therefore, constructing an appropriate interface and enhancing the charge transfer may work in promoting the charge extraction efficiency and passivating the defects.

Quantum dots (QDs) are nanocrystals of several nanometers in diameter, and they are capable of tuning the optical and electronic properties by adjusting the size or composition [16–18]. Evidence has shown that modifying the energy level of QDs has significant impact on interface charge

transfer [15, 19, 20]. Instead of pursuing proper intermediate buffer layers, we intend to design QDs with proper energy band structures to make better energy level alignment between $CsPbBr_3$ and TiO_2 in PSCs because of the featured energy level tunability of the QDs. Many work shows that reducing the energy offset between the donor and the acceptor can accelerate the charge transfer at the interface [21–25]. Herein, we design core/multishell QDs with the conduction band (CB) ranging in -3.72~-3.87 eV. By inserting the QD layer between the TiO_2 and $CsPbBr_3$, we construct a cascade energy alignment, where photoexcited electrons can be extracted efficiently. Arising from the improved charge transfer rate, the optimized device exhibits a PCE of 8.64%, which is 20% higher than the device without QD intermediate layer.

2. Experimental

2.1. Materials.
Cadmium oxide (CdO, 99.99%), sulfur (99.9%, powder), tri-n-octylphosphine (TOP, 90%), oleic acid (OA, 99%), selenium (99%, powder), 1-dodecanethiol (DDT, 98%), 1-octadecene (1-ODE, 90%), titanium isopropoxide (AR, 95%), titanic chloride (AR, 99.0%), lead bromide ($PbBr_2$, AR, 99.0%), caesium bromide (CsBr, AR, 99.9%), N,N-dimethylformamide (DMF, AR, 99.5%), methanol (AR, 99.5%), and isopropanol were purchased from Aladdin. All the materials were used as received without further purification.

2.2. Preparation of Precursors.
Cationic precursors (0.1 M cadmium oleate $Cd(OA)_2$ and 0.5 M cadmium oleate ($Cd(OA)_2$)) were prepared by dissolving CdO (4 mmol or 20 mmol) in a mixed solvent of OA (20 mL) and 1-ODE (20 mL) under N_2 atmosphere at 250°C for 30 min, degassing at 150°C for 30 min, and filling with N_2. Anionic precursors (0.1 M TOP-Se) were prepared by dissolving the selenium power (1 mmol) in 10 mL of TOP under N_2 atmosphere at room temperature.

2.3. Synthesis of CdS Seeds.
First, 38.5 mg CdO (0.3 mmol) was loaded in a three-neck flask containing 1 mL of OA and 8 mL of 1-ODE at 150°C under N_2 atmosphere. Then the mixture solution was heated to 270°C, and 0.25 M S-ODE (0.5 mL) was rapidly injected into the reaction flask and stayed for 8 min. The resultant nanocrystals were purified twice by the precipitation (ethanol) and redispersion (toluene) method.

2.4. Synthesis of CdS/CdSe/CdS Nanocrystals.
For CdSe emissive layer growth, the desired amount of mixed Cd and Se precursors (0.1 M $Cd(OA)_2$ and 0.1 M TOP-Se) was injected into the three-neck flask containing CdS seeds (0.1 g) and 1-ODE (8 mL) at 300°C at a rate of 10 mL/hr. The obtained CdS/CdSe NCs do not require any purification. For CdS shell growth, the desired amount of 0.5 M $Cd(OA)_2$ and 1 M DDT-ODE were injected separately into the reaction solution at 300°C at a rate of 4 mL/hr. The reaction temperature was maintained at 300°C for the entire CdS shelling process and cooled down to room temperature to stop the reaction. The resultant CdS/CdSe/CdS NCs were purified twice.

2.5. Fabrication of All-Inorganic $CsPbBr_3$ Solar Cells.
All-inorganic $CsPbBr_3$ solar cells were prepared according to the previously reported method with some modifications [26]. Typically, 90 μL of CdS/CdSe/CdS solution in toluene was spin-coated onto the FTO/c-TiO_2/m-TiO_2 layer at 2000 rpm for 30 s and heated at 80°C for 10 min. Subsequently, an N,N-dimethylformamide (DMF) solution of 1.0 M $PbBr_2$ was spin-coated onto the CdS/CdSe/CdS layer at 2000 rpm for 30 s, followed by drying at 80°C for 60 min. Then the 0.07 M CsBr methanol solution was spin-coated onto the $PbBr_2$ film at 2000 rpm for 30 s and continuingly heated at 250°C for 5 min. This process was repeated for several times. Finally, the carbon electrode served as both hole transport layer (HTL), and the counter electrode was deposited on the $CsPbBr_3$ layer by doctor-blade coating of conductive carbon ink and then heated at 70°C for 60 min.

3. Results and Discussion

Figure 1(a) illustrates the architecture of the QDs, where a CdS is used as core and a monolayer or multilayer of CdSe grows on the CdS core, followed by growing a thick CdS shell. Both the CB and VB levels of the CdSe are contained between the CB and valence band (VB) of the CdS core and shell. Therefore, the CdS/CdSe/CdS QDs possess a spherical quantum well structure, where the electrons and holes are strongly confined in the CdSe layer. XRD results of the CdS, CdS/CdSe, and CdS/CdSe/CdS QDs are shown in Figure 1(b). The CdS exhibit characteristic peaks at 26.5°, 43.9°, and 51.9°, which are consistent with diffraction angles of the (111, 220, 311) of the standard zinc blende card (JCPDS 01-0647). After coated with CdSe shell, the resultant CdS/CdSe also shows three typical zinc blende diffraction peaks located at 25.61°, 42.89°, and 49.9° with a little shift to those of the CdS core. These XRD results confirm that CdSe shelling does not affect the zinc structure of the CdS just undergoing an epitaxial shell growth of CdSe. However, the growth of the second CdS shell on the zinc blende CdS/CdSe generates a wurtzite crystal structure featured with diffraction peaks at 24.6°, 26.3°, 28.4°, 43.6°, 47.0°, and 52.3°. The presence of the wurtzite structure in this QD is in accordance with some related core/shell systems containing both the wurtzite and zinc blende crystal structures [27]. Transmission electron microscopy (TEM) images from Figures 1(c)–1(f) show that the average diameter increases with the increases of CdSe shell. The TEM images of the prepared QDs display that all QDs have high crystallinity and monodisperse. The average diameters of the QDs are estimated by calculating over 10 TEM images as shown at the bottom of Figure 1. All the QDs are produced from the same CdS core, and the thicknesses of the outer CdS shell are also the same; we denote the QDs as CdS/CdSe(X monolayer, X ML)/CdS for simplicity. The average diameters of the QDs are determined to be 6.25 nm, 7.25 nm, 8.0 nm, and 11.0 nm for the CdS/CdSe(1 ML)/CdS, CdS/CdSe(3 ML)/CdS, CdS/CdSe(4 ML)/CdS, and CdS/CdSe(6 ML)/CdS, respectively.
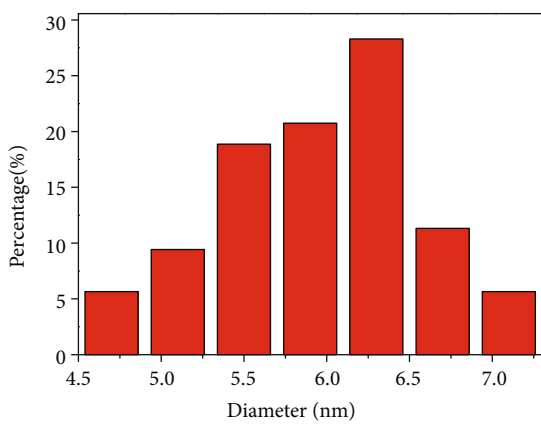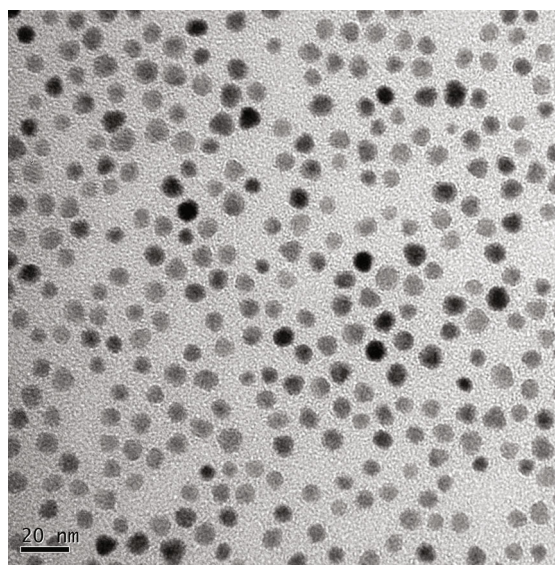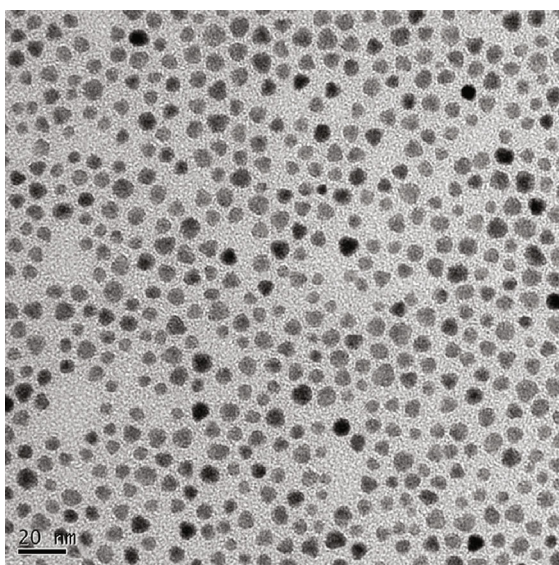
Although changing the size of the CdS core or the thickness of CdS can affect the energy structure of the QDs, controlling the thickness of the CdSe offers much wider
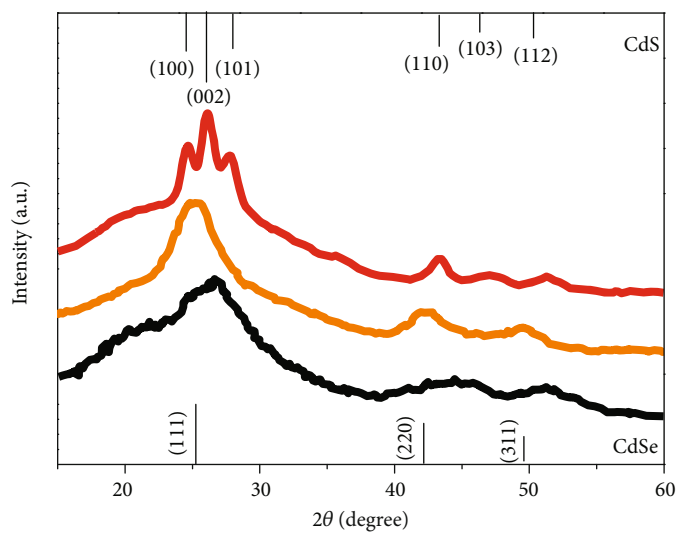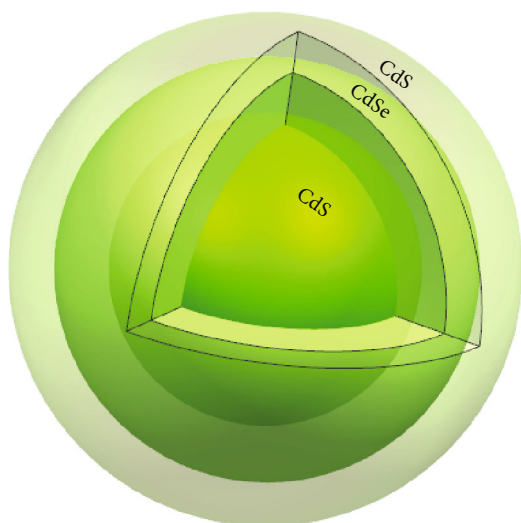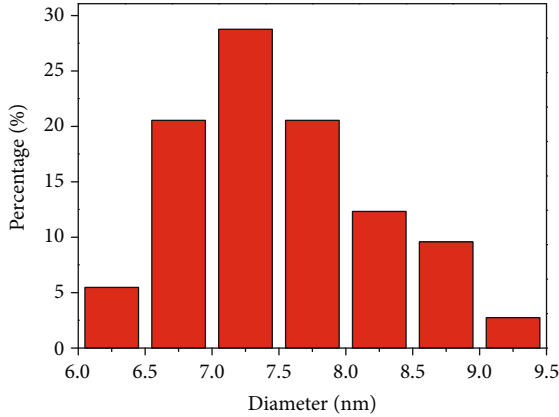
(a)

(b)
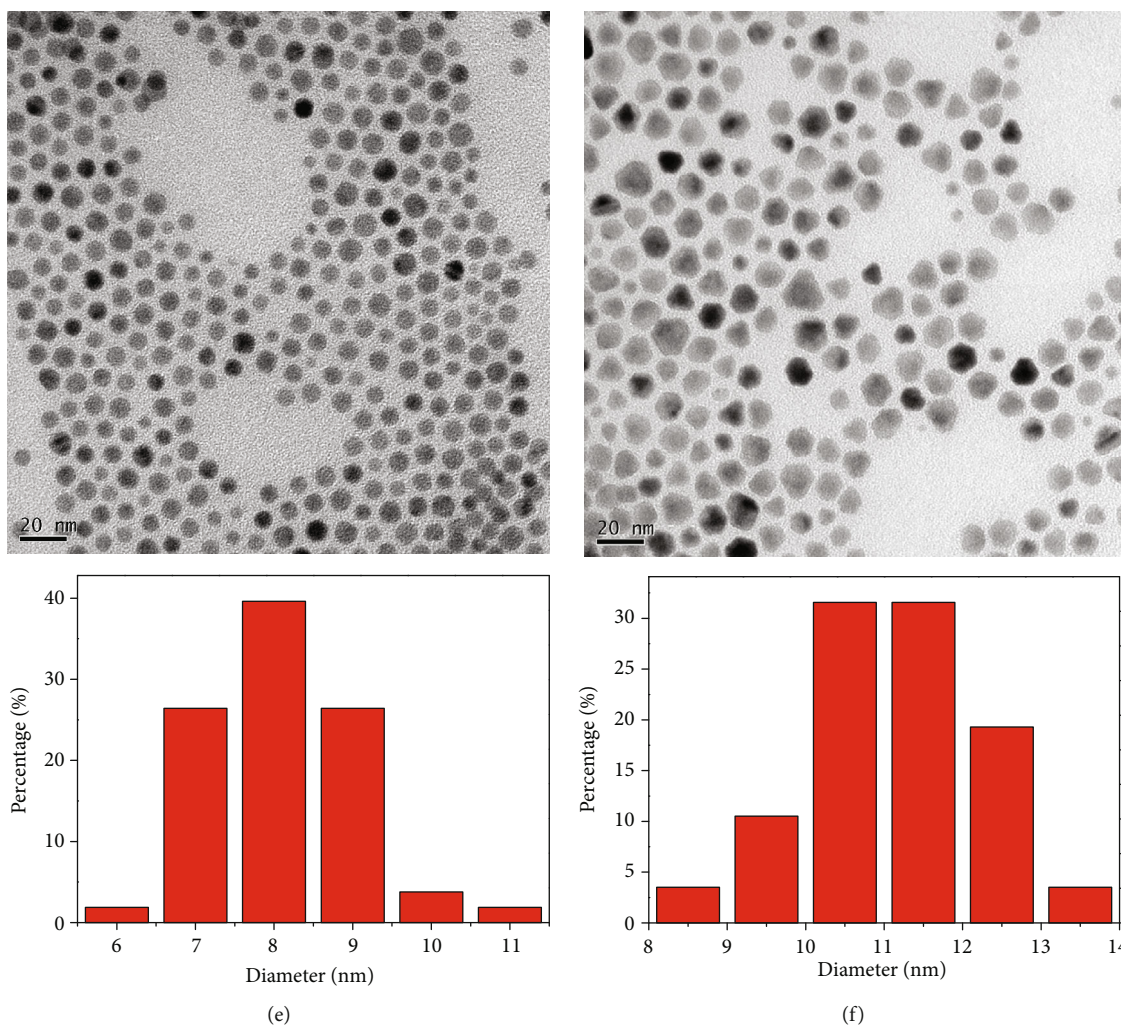

(c)

(d)

FIGURE 1: Continued.

(e)

(f)

FIGURE 1: (a) Schematic structures of CdS/CdSe/CdS QD. (b) XRD patterns of CdS seeds, CdS/CdSe, and CdS/CdSe/CdS QDs. (c–f) TEM images of CdS/CdSe/CdS QDs with varying CdSe shell thicknesses (1, 3, 5, and 6 ML) with the corresponding average diameter statistical charts for the QDs.

tenability on the energy levels. CdS has a higher CB and a lower VB than those of CdSe. Therefore, in the CdS/CdSe system, both the hole and electron charges are partially delocalized on the shell materials. Theoretical and experimental results have demonstrated that shell thickness has an influence on the band energy structure of this inverted type I system [28–30]. There is a competition between the kinetic energy and the potential energy in this system. With shell thickness increases, both the electron and the hole wave functions in the center of the particle are increased, while keeping the particle size constant [28]. Hence, the bandgap structure can be adjusted by changing the thickness of CdSe shell. Furthermore, type I and reverse type I QDs usually encounter the predicament of low PL QYs, and type II ones encounter low photooxidation stability. However, QDs with multilayer of shells exhibit both these two high properties [30, 31]. Therefore, a CdS layer was introduced upon the CdS/CdSe QDs to realize the passivation of surface defects. In short, by controlling the thickness of CdSe layer, the CB of CdS/CdSe/CdS QDs can be tuned.

For core/shell QDs, shell usually have a nonnegligible impact on the energy structure, so as to the optical properties of the dots. Many II-IV and I-III-VI core/shell QDs have been synthesized to enhance the stability and the photoluminescence (PL) quantum yields (QYs) of pure cores or to restrain the dot-dot FRET that is beneficial to the improvement of device performance [32–34]. However, there exists a pronounced trade-off between the shell thickness and the PL QYs in the CdSe/CdS system, owing to the traps originated from the exceeded epitaxy of shells. Hence, appropriate shell layers are generally required.

Figures 2(a) and 2(b) show the photoluminescence (PL) spectra of the QDs with different CdSe shell thicknesses. Under the irradiation of an ultraviolet (UV) lamp, the QDs show different color from green to red, indicating the promising tenability of the emission wavelengths. Figure 2(c) shows tunable absorption band edges of the QDs ranging from 580 to 652 nm, corresponding to the bandgaps between 2.14 and 1.90 eV according to the relationship $E_g = 1240/\lambda$ eV. For a conventional inorganic PSC, the energy offset
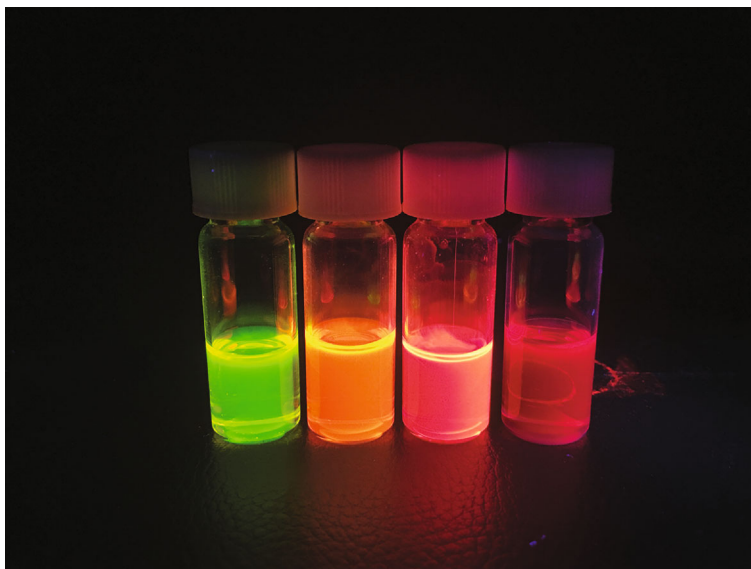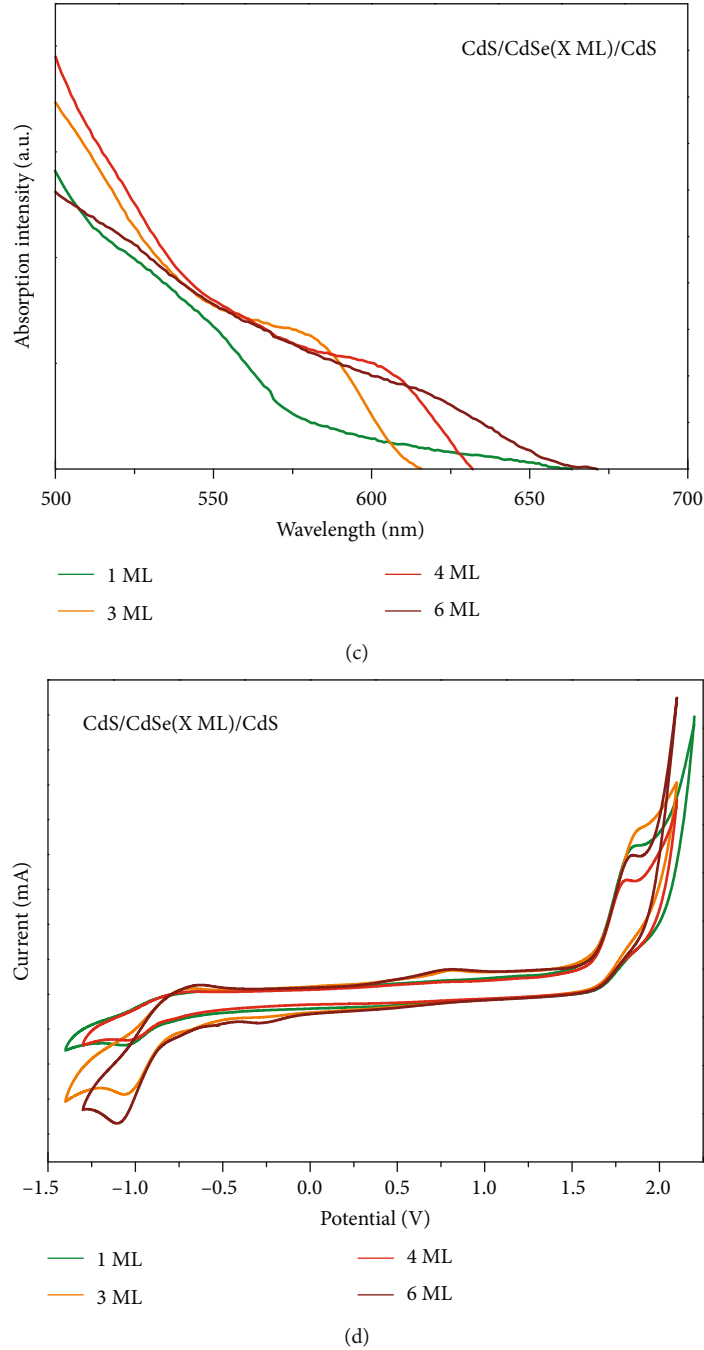
(a)
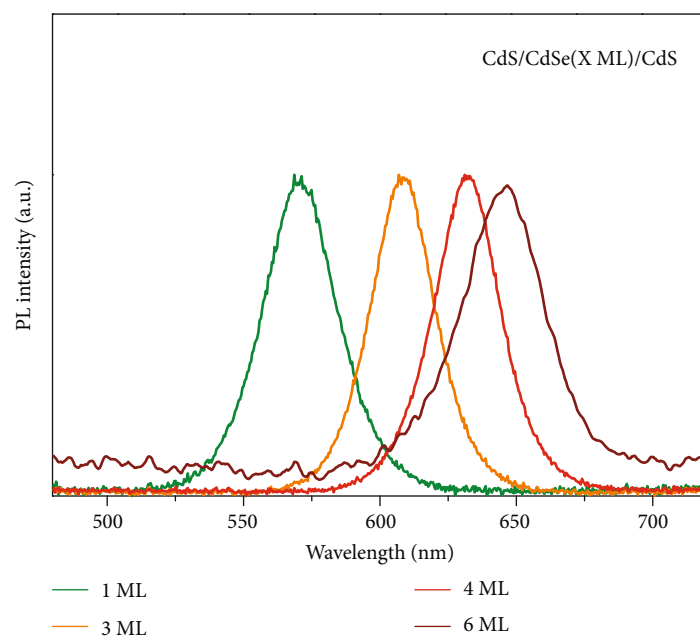
(b)

Figure 2: Continued.

(c)

(d)

Figure 2: (a) Photograph of CdS/CdSe/CdS solutions under the irradiation of a 365 nm lamp. (b) PL spectra of CdS/CdSe/CdS QDs. (c) Absorption spectra of CdS/CdSe/CdS QDs. (d) CV behaviors of the CdS/CdSe/CdS QDs.

between the CB of CsPbBr$_3$ (-3.30 eV) and TiO$_2$ (-4.20 eV) is about 0.90 eV, which is large enough to overcome the Coulomb attraction (typically 0.1-0.5 eV) [35]. Gong et al. have demonstrated that electrons can transfer efficiently even with an energy offset as small as 0.12 eV [36]. This prompts us to employ QD as intermediate layer to reduce the "excess" energy offset between TiO$_2$ and CsPbBr$_3$. Therefore, we performed CV tests to determine the energy level of the prepared QDs with respect to the vacuum level. Figure 2(d) shows obvious oxidation and reduction waves for all QD films,

Table 1: Electrochemical parameters of the CdS/CdSe/CdS QDs.

CdS/CdSe (X ML)/CdS	E_{Re}(V)/CB (eV)	E_{Ox} (V)/VB (eV)	E_g (eV)
1 ML	-0.75/-3.72	1.55/-6.02	2.30
3 ML	-0.70/-3.77	1.55/-6.02	2.25
4 ML	-0.72/-3.75	1.55/-6.02	2.27
6 ML	-0.60/-3.87	1.55/-6.02	2.15
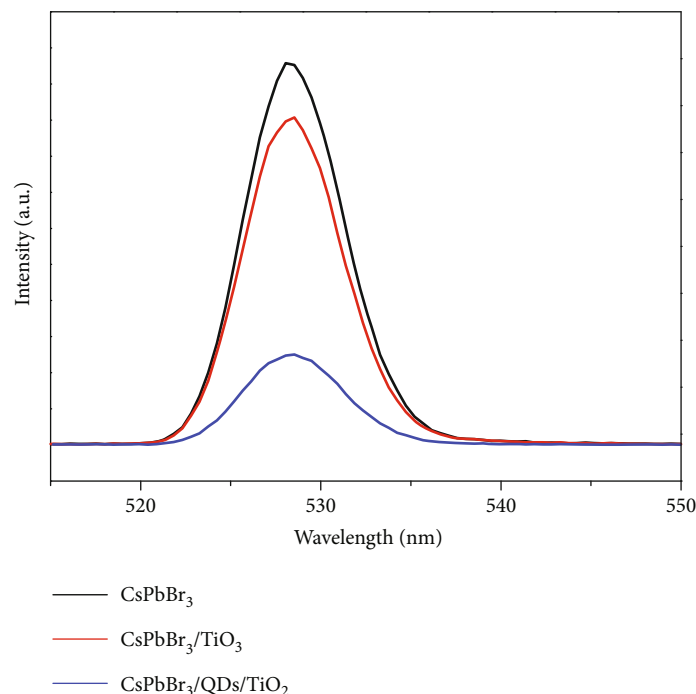
(a)
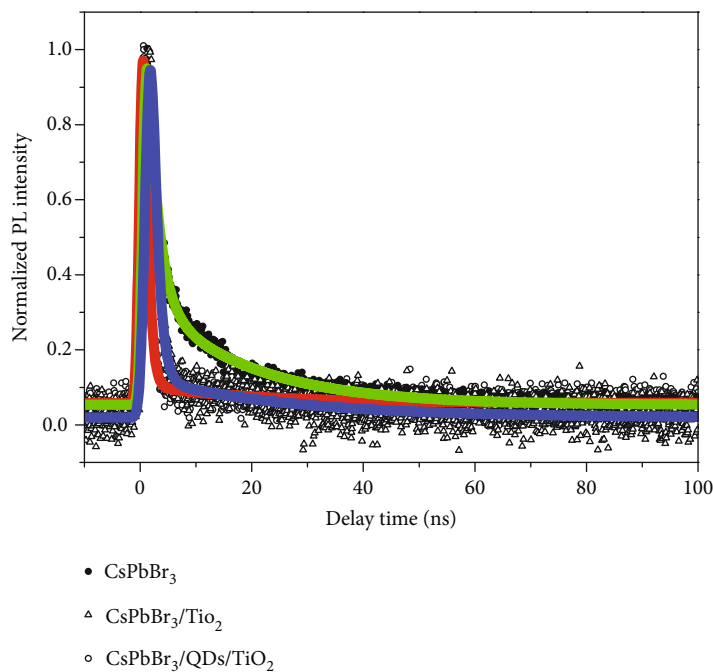
(b)

FIGURE 3: (a) Steady PL spectra of CsPbBr$_3$, CsPbBr$_3$/TiO$_2$, and CsPbBr$_3$/QDs/TiO$_2$ films. (b) The PL decays of CsPbBr$_3$, CsPbBr$_3$/TiO$_2$, and CsPbBr$_3$/QD/TiO$_2$ films.

implying that the QD as an intermediate layer has good capability conducting electrons and holes. The CB and VB levels of the QDs are calculated by using the formula: CB or VB = $-4.8 - (E - E_{1/2})$ (eV), where E is the peak point of the redox potential and $E_{1/2}$ is the formal ferrocene potential against the Ag/Ag$^+$ system and determined to be $E_{1/2} = 0.33$ eV.

The electrochemical parameters of the QDs are summarized in Table 1. With the increase of the thicknesses of the CdSe shell, the CB level changes from -3.72 to -3.87 eV, whereas the VB level varies little as compared with the CB level. Similar results are observed for other QD systems. All the CB levels of the QDs locate between the CB of CsPbBr$_3$

TABLE 2: Lifetimes and charge transfer rate estimated from PL decays.

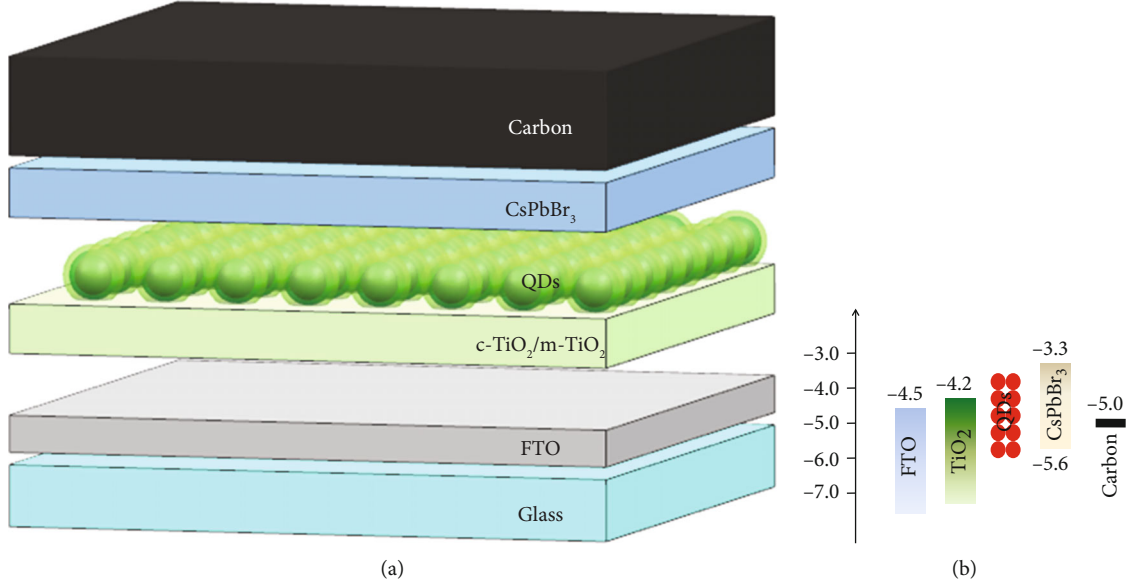| Kinetic parameters	a_1	τ_1 (ns)	a_2	τ_2 (ns)	τ (ns)	k_{ct} ($\times 10^9$ s^{-1})
Pristine CsPbBr$_3$	0.81	1.90 ± 0.05	0.20	17.7 ± 0.5	12.4 ± 0.5	
CsPbBr$_3$/TiO$_2$	0.91	0.9 ± 0.1	0.1	13 ± 1	8.3 ± 1	0.040
CsPbBr$_3$/QDs/TiO$_2$	0.95	0.6 ± 0.1	0.04	14 ± 1	7.2 ± 1	0.059

FIGURE 4: The architecture of all-inorganic CsPbBr$_3$ perovskite solar cell using CdS/CdSe/CdS QDs as an electron modification layer. (b) The schematic diagram of the energy level structure of the PSC.

(-3.3 eV) and the CB of TiO$_2$ (-4.2 eV). We expect that inserting the QD layer between CsPbBr$_3$ and TiO$_2$ will reduce the excess energy offset and benefit the electron extraction.

To explore the influences of the QD layer on the charge transfer properties of the solar cell, steady state PL and time-resolved PL measurements were performed. Comparative analysis on CsPbBr$_3$/QDs/TiO$_2$ against CsPbBr$_3$/TiO$_2$ enables us identify the role of QDs that plays on the interface charge transfer. Figure 3(a) shows that the PL intensity of the CsPbBr$_3$ decreases notably when interfaced with TiO$_2$, but inserting the QDs between CsPbBr$_3$ and TiO$_2$ can further quench the PL intensity. The degree of the PL intensity quenching is quite sensitive to the charge transfer from CsPbBr$_3$ to TiO$_2$. Such a high degree of PL quenching indicates the strong charge transfer of the CsPbBr$_3$/QDs/TiO$_2$. To evaluate the exact charge transfer rate at the interface, time-resolved PL measurements were performed, and the results are shown in Figure 3(b). Interfaced with the TiO$_2$ layer, the emission decays dramatically. An additional intermediate QD layer results in a fastest decay as compared with the neat CsPbBr$_3$ and CsPbBr$_3$/TiO$_2$ blend. Analyzing the slope of the decay curves, we found that the biexponential function is satisfactory to fit the decays [37]:

$$I(t) = [a_1 \exp{(-t/\tau_1)} + a_2 \exp{(-t/\tau_2)}] \otimes F(t), \quad (1)$$

where signal $I(t)$ is the convolution of the biexponential function and the impulse response function (IRF) $F(t)$, a_1 and a_2 are the amplitudes, and τ_1 and τ_2 are lifetimes. Then the average lifetimes are calculated by

$$\tau = \frac{a_1\tau_1^2 + a_2\tau_2^2}{a_1\tau_1 + a_2\tau_2}. \quad (2)$$

Comparing the average lifetime of the CsPbBr$_3$, CsPbBr$_3$/TiO$_2$, and CsPbBr$_3$/QD/TiO$_2$ blend films, we can evaluate the interface charge transfer rate k_{ct} by using

$$k_{ct} = \frac{1}{\tau_{blend}} - \frac{1}{\tau_{CsPbBr_3}}. \quad (3)$$

All the kinetic parameters are listed in Table 2. The average decay time t of the neat CsPbBr$_3$, CsPbBr$_3$/TiO$_2$, and CsPbBr$_3$/QDs/TiO$_2$ is 12.4, 8.3, and 7.2 ns, respectively. Strikingly, the charge transfer rate of CsPbBr$_3$/QDs/TiO$_2$ is 0.059×10^9 s^{-1}, which is over 40% faster than that of CsPbBr$_3$/TiO$_2$.

Figure 4(a) illustrates the device architecture of the all-inorganic PSC with FTO/c-TiO$_2$/m-TiO$_2$/QDs/CsPbBr$_3$/carbon configuration. Unlike other PSCs that need hole-transporting layers (HTLs), our all-inorganic PSCs are
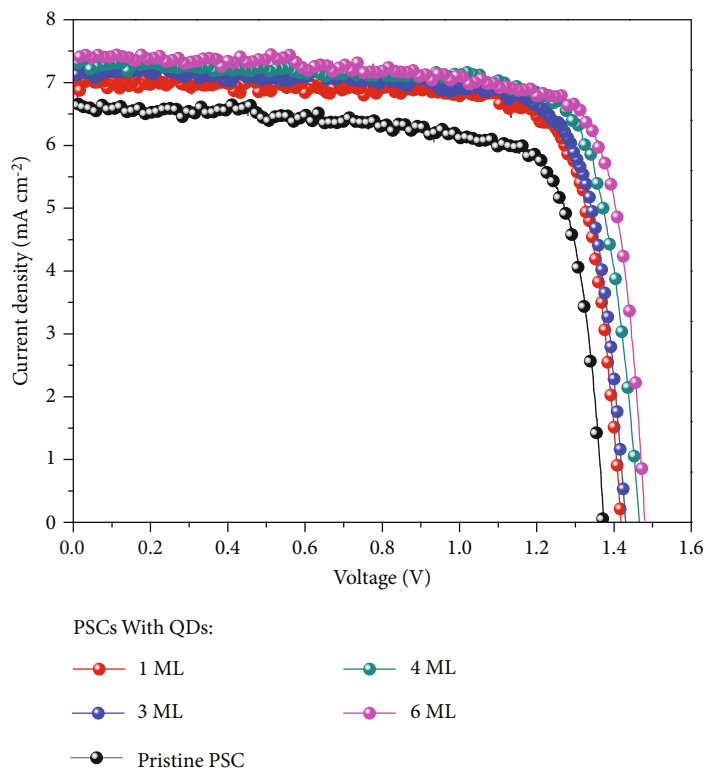
FIGURE 5: $J - V$ curves of all-inorganic PSCs with and without CdS/CdSe/CdS QDs intermediate layer.

HTL-free. The QDs are used as an intermediate layer between TiO_2 and $CsPbBr_3$. As displayed in Figure 4(b), the CB levels of the QDs range in -3.72~-3.87 eV, which locate above the CB of TiO_2 (-4.2 eV), implying that the QDs are electronically active for electron transfer. Inserting the QD layer also creates a cascade energy level architecture where the energy offset is lowered, which may accelerate the charge transfer process and direct the charge-carriers to circuit. Figure 5 shows the current density-voltage ($J - V$) curves of the all-inorganic PSCs under the illumination of the simulated sunlight (AM1.5G). The photovoltaic parameters of the PSC with different QDs are summarized in Table 3, including open-circuit voltage (V_{oc}), short-circuit current density (J_{sc}), and filling factor (FF). The pristine $CsPbBr_3$ PSC delivers a moderate PCE of 7.15% ($V_{oc} = 1.368$ V, $J_{sc} = 6.69$ mA cm^{-2}, and $FF = 0.78$), which is comparable to other HTL-free inorganic PSCs [8, 15]. After inserting the QDs as intermediate layers, all the devices yield higher J_{sc}, V_{oc}, and PCE than that of the reference device. The underlying mechanism of this enhancement is that the cascade energy level is formed by inserting QDs with appropriate CB level between the CB of TiO_2 and $CsPbBr_3$, thus offering fast charge transfer channel to gain efficient charge extraction. As a consequence, the champion PSC with QDs shows a PCE of 8.64%, which is 20% higher than that of pristine $CsPbBr_3$ PSC.

4. Conclusion

In summary, we have synthesized CdS/CdSe/CdS QDs with tunable energy levels and used them as intermediate layers

TABLE 3: The photovoltaic data of all-inorganic PSCs.

PSCs	J_{sc} (mA cm^{-2})	V_{oc} (V)	FF	PCE (%)
Pristine	6.69	1.368	0.78	7.15
With QDs (1 ML)	7.14	1.419	0.78	7.92
With QDs (3 ML)	7.34	1.431	0.77	8.09
With QDs (4 ML)	7.38	1.466	0.78	8.47
With QDs (6 ML)	7.50	1.482	0.78	8.64

to enhance the performances of the inorganic PSCs. Evidence show that the CB level lies between the CB of TiO_2 and the CB of $CsPbBr_3$, which is suitable for transporting electrons. After inserting the QD intermediate layer, the CB energy offset between TiO_2 and $CsPbBr_3$ is reduced, thus leading to charge transfer rates boosting from 0.040×10^9 to 0.059×10^9 s^{-1}. The optimized PSC shows a PCE as high as 8.64%, which is over 20% higher than 7.15% for the pristine device. This work offers potential route to design HTL-free inorganic PSCs with efficient charge transfer.

Data Availability

Findings of this research work will be provided from corresponding author on reasonable demand.

Conflicts of Interest

The authors declare no conflicts of interest.

Acknowledgments

References

[1] W. S. Yang, B.-W. Park, E. H. Jung et al., "Iodide management in formamidinium-lead-halide-based perovskite layers for efficient solar cells," *Science*, vol. 356, no. 6345, pp. 1376–1379, 2017.

[2] N. J. Jeon, J. H. Noh, W. S. Yang et al., "Compositional engineering of perovskite materials for high-performance solar cells," *Nature*, vol. 517, no. 7535, pp. 476–480, 2015.

[3] Y. Liu, S. Akin, L. Pan et al., "Ultrahydrophobic 3D/2D fluoroarene bilayer-based water-resistant perovskite solar cells with efficiencies exceeding 22%," *Science Advances*, vol. 5, no. 6, p. eaaw2543, 2019.

[4] Y. Wang, M. I. Dar, L. K. Ono et al., "Thermodynamically stabilized β-CsPbI$_3$–based perovskite solar cells with efficiencies >18%," *Science*, vol. 365, no. 6453, pp. 591–595, 2019.

[5] J. Liang, C. Wang, Y. Wang et al., "All-inorganic perovskite solar cells," *Journal of the American Chemical Society*, vol. 138, no. 49, pp. 15829–15832, 2016.

[6] J. Liang, P. Zhao, C. Wang et al., "CsPb0.9Sn0.1IBr2Based all-inorganic perovskite solar cells with exceptional efficiency and stability," *Journal of the American Chemical Society*, vol. 139, no. 40, pp. 14009–14012, 2017.

[7] X. Chang, W. Li, L. Zhu et al., "Carbon-based CsPbBr3Perovskite solar cells: all-ambient processes and high thermal stability," *ACS Applied Materials & Interfaces*, vol. 8, no. 49, pp. 33649–33655, 2016.

[8] X. Zhang, Z. Jin, J. Zhang et al., "All-ambient processed binary CsPbBr3–CsPb2Br5Perovskites with synergistic enhancement for High-Efficiency Cs–Pb–Br-Based solar cells," *ACS Applied Materials & Interfaces*, vol. 10, no. 8, pp. 7145–7154, 2018.

[9] C. Liu, W. Li, C. Zhang, Y. Ma, J. Fan, and Y. Mai, "All-inorganic CsPbI2Br perovskite solar cells with high efficiency exceeding 13%," *Journal of the American Chemical Society*, vol. 140, no. 11, pp. 3825–3828, 2018.

[10] J. Duan, H. Xu, W. E. I. Sha et al., "Inorganic perovskite solar cells: an emerging member of the photovoltaic community," *Journal of Materials Chemistry A*, vol. 7, no. 37, pp. 21036–21068, 2019.

[11] M. Kulbak, S. Gupta, N. Kedem et al., "Cesium enhances long-term stability of lead bromide perovskite-based solar cells," *Journal of Physical Chemistry Letters*, vol. 7, no. 1, pp. 167–172, 2016.

[12] J. Duan, Y. Zhao, B. He, and Q. Tang, "High-purity inorganic perovskite films for solar cells with 9.72 % efficiency," *Angewandte Chemie International Edition*, vol. 57, no. 14, pp. 3787–3791, 2018.

[13] J. Ding, J. Duan, C. Guo, and Q. Tang, "Toward charge extraction in all-inorganic perovskite solar cells by interfacial engineering," *Journal of Materials Chemistry A*, vol. 6, no. 44, pp. 21999–22004, 2018.

[14] J. Duan, Y. Zhao, X. Yang, Y. Wang, B. He, and Q. Tang, "Lanthanide ions doped CsPbBr3Halides for HTM-free 10.14%-efficiency inorganic perovskite solar cell with an ultrahigh open-circuit voltage of 1.594 V," *Advanced Energy Materials*, vol. 8, no. 31, article 1802346, 2018.

[15] G. Liao, J. Duan, Y. Zhao, and Q. Tang, "Toward fast charge extraction in all-inorganic CsPbBr$_3$ perovskite solar cells by setting intermediate energy levels," *Solar Energy*, vol. 171, pp. 279–285, 2018.

[16] X. Jin, H. Li, S. Huang et al., "Bright alloy type-II quantum dots and their application to light-emitting diodes," *Journal of Colloid and Interface Science*, vol. 510, pp. 376–383, 2018.

[17] O. Chen, J. Zhao, V. P. Chauhan et al., "Compact high-quality CdSe-CdS core-shell nanocrystals with narrow emission linewidths and suppressed blinking," *Nature Materials*, vol. 12, no. 5, pp. 445–451, 2013.

[18] C. Pu and X. Peng, "To battle surface traps on CdSe/CdS core/-shell nanocrystals: shell isolation versus surface treatment," *Journal of the American Chemical Society*, vol. 138, no. 26, pp. 8134–8142, 2016.

[19] W. Cao, C. Xiang, Y. Yang et al., "Highly stable QLEDs with improved hole injection via quantum dot structure tailoring," *Nature Communications*, vol. 9, no. 1, p. 2608, 2018.

[20] G. S. Selopal, H. Zhao, X. Tong et al., "Highly stable colloidal "giant" quantum dots sensitized solar cells," *Advanced Functional Materials*, vol. 27, no. 30, article 1701468, 2017.

[21] X. Jin, W. Sun, S. Luo et al., "Energy gradient architectured praseodymium chalcogenide quantum dot solar cells: towards unidirectionally funneling energy transfer," *Journal of Materials Chemistry A*, vol. 3, no. 47, pp. 23876–23887, 2015.

[22] Q. Li, X. Jin, X. Yang et al., "Reducing the excess energy offset in organic/inorganic hybrid solar cells: toward faster electron transfer," *Applied Catalysis B: Environmental*, vol. 162, pp. 524–531, 2015.

[23] X. Jin, W. Sun, Z. Chen et al., "Exciton generation/dissociation/charge-transfer enhancement in inorganic/organic hybrid solar cells by robust single nanocrystalline LnP$_x$O$_y$ (Ln = Eu, Y) doping," *ACS Applied Materials & Interfaces*, vol. 6, no. 11, pp. 8771–8781, 2014.

[24] F. Li, J. Wei, G. Liao et al., "Quaternary quantum dots with gradient valence band for all-inorganic perovskite solar cells," *Journal of Colloid and Interface Science*, vol. 549, pp. 33–41, 2019.

[25] M. Cha, P. da, J. Wang et al., "Enhancing perovskite solar cell performance by interface engineering using CH3NH3PbBr0.9I2.1Quantum dots," *Journal of the American Chemical Society*, vol. 138, no. 27, pp. 8581–8587, 2016.

[26] B. G. Jeong, Y.-S. Park, J. H. Chang et al., "Colloidal spherical quantum wells with near-unity photoluminescence quantum yield and suppressed blinking," *ACS Nano*, vol. 10, no. 10, pp. 9297–9305, 2016.

[27] B. Mahler, N. Lequeux, and B. Dubertret, "Ligand-controlled polytypism of thick-shell CdSe/CdS nanocrystals," *Journal of the American Chemical Society*, vol. 132, no. 3, pp. 953–959, 2010.

[28] J. W. Haus, H. S. Zhou, I. Honma, and H. Komiyama, "Quantum confinement in semiconductor heterostructure nanometer-size particles," *Physical Review B*, vol. 47, no. 3, pp. 1359–1365, 1993.

[29] Z. Pan, H. Zhang, K. Cheng, Y. Hou, J. Hua, and X. Zhong, "Highly efficient inverted type-I CdS/CdSe core/shell structure QD-sensitized solar cells," *ACS Nano*, vol. 6, no. 5, pp. 3982–3991, 2012.

[30] D. Battaglia, J. J. Li, Y. Wang, and X. Peng, "Colloidal two-dimensional systems: CdSe quantum shells and wells," *Angewandte Chemie*, vol. 42, no. 41, pp. 5035–5039, 2003.

[31] R. G. Chaudhuri and S. Paria, "Core/shell nanoparticles: classes, properties, synthesis mechanisms, characterization, and applications," *Chemical Reviews*, vol. 112, no. 4, pp. 2373–2433, 2012.

[32] I. Coropceanu and M. G. Bawendi, "Core/shell quantum dot based luminescent solar concentrators with reduced reabsorption and enhanced efficiency," *Nano Letters*, vol. 14, no. 7, pp. 4097–4101, 2014.

[33] Y. Niu, C. Pu, R. Lai et al., "One-pot/three-step synthesis of zinc-blende CdSe/CdS core/shell nanocrystals with thick shells," *Nano Research*, vol. 10, no. 4, pp. 1149–1162, 2017.

[34] J.-H. Kim and H. Yang, "High-efficiency Cu-In-S quantum-dot-light-emitting device exceeding 7%," *Chemistry of Materials*, vol. 28, no. 17, pp. 6329–6335, 2016.

[35] T. M. Clarke and J. R. Durrant, "Charge photogeneration in organic solar cells," *Chemical Reviews*, vol. 110, no. 11, pp. 6736–6767, 2010.

[36] X. Gong, M. Tong, F. G. Brunetti et al., "Bulk heterojunction solar cells with large open-circuit voltage: electron transfer with small donor-acceptor energy offset," *Advanced Materials*, vol. 23, no. 20, pp. 2272–2277, 2011.

[37] D. McMorrow, W. T. Lotshaw, and G. A. Kenney-Wallace, "Femtosecond optical Kerr studies on the origin of the nonlinear responses in simple liquids," *IEEE Journal of Quantum Electronics*, vol. 24, no. 2, pp. 443–454, 1988.